HYDROGEN ADSORPTION ON Co^{2+}-, Ni^{2+}- EXCHANGED ZEOLITES ZSM-5 AND US-Y

A THESIS SUBMITTED TO
THE GRADUATE SCHOOL OF NATURAL AND APPLIED SCIENCES
OF
MIDDLE EAST TECHNICAL UNIVERSITY

BY

NURKAN SAROHAN

IN PARTIAL FULFILLMENT OF THE REQUIREMENTS
FOR
THE DEGREE OF MASTER OF SCIENCE
IN
CHEMICAL ENGINEERING

AUGUST 2022

Approval of the thesis:

HYDROGEN ADSORPTION ON Co^{2+}-, Ni^{2+}- EXCHANGED ZEOLITES ZSM-5 AND US-Y

submitted by **NURKAN SAROHAN** in partial fulfillment of the requirements for the degree of **Master of Science** i**n Chemical Engineering, Middle East Technical University** by,

Prof. Dr. Halil Kalıpçılar
Dean, Graduate School of **Natural and Applied Sciences** _____

Prof. Dr. Pınar Çalık
Head of the Department, **Chemical Engineering** _____

Assoc. Prof. Dr. Bahar İpek Torun
Supervisor, **Chemical Engineering, METU** _____

Examining Committee Members:

Prof. Dr. Halil Kalıpçılar
Chemical Engineering, METU _____

Assoc. Prof. Dr. Bahar İpek Torun
Chemical Engineering, METU _____

Assoc. Prof. Dr. Zeynep Çulfaz Emecen
Chemical Engineering, METU _____

Prof. Dr. Burcu Akata Kurç
Micro and Nanotechnology, METU _____

Asst. Prof. Dr. Murat Oluş Özbek
Chemical Engineering, GTU _____

Date: 09.08.2022

I hereby declare that all information in this document has been obtained and presented in accordance with academic rules and ethical conduct. I also declare that, as required by these rules and conduct, I have fully cited and referenced all material and results that are not original to this work.

Name Last name : Nurkan Sarohan

Signature :

ABSTRACT

HYDROGEN ADSORPTION ON Co^{2+}-, Ni^{2+}- EXCHANGED ZEOLITES ZSM-5 AND US-Y

Sarohan, Nurkan
Master of Science, Chemical Engineering
Supervisor: Assoc. Prof. Dr. Bahar İpek Torun

August 2022, 130 pages

The increase in greenhouse gases motivates the search for renewable energy sources and carriers. Hydrogen is an attractive option used as an energy carrier due to its high gravimetric energy density (140 kJ/kg). Although hydrogen energy has been used in fuel cell electric vehicles (FCEVs) at an increasing rate over the years, its storage is still the main concern. Zeolites, carbon-based materials, and metal organic frameworks (MOFs) are porous materials that store hydrogen through physical adsorption. In this thesis, Ni^{2+} or Co^{2+}- exchanged micro-and mesoporous zeolites ZSM-5 and US-Y are prepared for the hydrogen adsorption tests. According to the experiments performed at 298 K and up to 10 bar, Ni^{2+}-,Co^{2+}- zeolites show gravimetric storage capacity in the range of 0.14–0.05 wt.%. The experimentally calculated initial isosteric heat of H_2 adsorption values are between -23 and -40 kJ/mol for Ni^{2+}-zeolites and -15 and -19 kJ/mol for Co^{2+}-zeolites. Ni^{2+}-, Co^{2+}-zeolites show reversible storage at 298 K and up to 50 bar due to the optimum heat of adsorption values. Among the results obtained at 298 K and up to 50 bar experiments, the highest volumetric storage capacity is reached with Meso-Na^{+},Ni^{2+}-ZSM-5 by 20 g H_2/L, showing a great potential to be used as H_2 storage material at 298 K. On the other hand, calculated high maximum storage capacity values on US-

Y at 77 K (~2.3 wt.%) via the Sips model show that US-Y can be an appropriate adsorbent for higher pressure or low temperature adsorption studies. The site information of Co^{2+} and Ni^{2+} cations on the samples are investigated using diffuse reflectance (DR) UV–Vis spectra and synchrotron powder X-ray Diffraction (XRD). The results show that hydrogen adsorption mostly occurs on β and γ sites in Co^{2+}-ZSM-5. According to synchrotron powder XRD analysis, the highest cation occupation is detected near Site III (in the supercage) of US-Y that are accessible to H_2 molecule. The theoretical site dependent heat of adsorption values ($-E_{ads}$) are calculated using both periodic and cluster density functional theory (DFT) for Ni^{2+}-,Co^{2+}-ZSM-5. β-site and γ-site occupation on Co^{2+}-ZSM-5 as well as an additional α-site occupation on Ni^{2+}-ZSM-5 are also predicted using DFT. Overall, it is found that the heat of adsorption values calculated from experiments and density functional theory (DFT) are within the same range.

Keywords: hydrogen adsorption, nickel, cobalt, synchrotron powder XRD, density functional theory

ÖZ

Co^{2+}- VE Ni^{2+}- İÇEREN ZEOLİTLER ZSM-5 VE US-Y ÜZERİNDE H_2 ADSORPSİYONU

Sarohan, Nurkan
Yüksek Lisans, Kimya Mühendisliği
Tez Yöneticisi: Assoc. Prof. Dr. Bahar İpek Torun

Ağustos 2022, 130 sayfa

Sera gazlarındaki artış, yenilenebilir enerji kaynakları ve enerji taşıyıcı arayışlarını motive etmektedir. Hidrojen, yüksek gravimetrik enerji yoğunluğu (140 kJ/kg) nedeniyle enerji taşıyıcısı olarak kullanılan ilgi çekici bir seçenektir. Hidrojen enerjisi, yakıt hücreli elektrikli araçlarda (FCEV'ler) yıllar içinde artan bir oranda kullanılmasına rağmen, hidrojenin depolanma problemi en büyük dezavantajı olmaktadır. Zeolitler, karbon bazlı malzemeler ve metal organik kafes yapıları, fiziksel adsorpsiyon yoluyla hidrojeni depolayan gözenekli malzemelerdir. Bu tezde, hidrojen adsorpsiyon testleri için Ni^{2+} veya Co^{2+}-değişimli mikro ve mezogözenekli zeolitler olan ZSM-5 ve US-Y hazırlanmıştır. 298 K ve 10 bar'a kadar yapılan deneylere göre, Ni^{2+}-,Co^{2+}- zeolitler ağırlıkça %0.14–0.05 aralığında depolama kapasitesi göstermektedir. H_2 adsorpsiyon değerlerinin deneysel olarak hesaplanan başlangıç izosterik ısısı, Ni^{2+}-zeolitler için -23 ile -40 kJ/mol ve Co^{2+}-zeolitler için -15 ile -19 kJ/mol arasındadır. Ni^{2+}-, Co^{2+}-zeolitler, optimum adsorpsiyon ısısı değerleri nedeniyle 298 K'de ve 50 bar'a kadar yapılan deneylerde tersinir depolama göstermişlerdir. 298 K ve 50 bar'a kadar olan deneylerde elde edilen sonuçlar arasında, en yüksek hacimsel depolama kapasitesine Meso-Na^{+},Ni^{2+}-ZSM-5 örneği (20 g H_2/L) ulaşılmıştır ve bahsedilen örnek 298 K'de H_2 depolama çalışmaları için

potansiyel olarak görülmektedir. Öte yandan, Sips modeli aracılığıyla 77 K'de hesaplanan US-Y örneklerinin maksimum depolama kapasiteleri (2.3 wt.%) onların yüksek gözenek hacmi ve yüzey alanı özelliklerinden dolayı yüksek basınç veya düşük sıcaklık adsorpsiyon çalışmaları için uygun bir adsorban olabileceğini göstermektedir. Örnekler içindeki Co^{2+} ve Ni^{2+} katyonlarının yerleşim yeri bilgisi ve çerçeve yapısı ile olan koordinasyonları dağınık yansıma ultraviyole ve görünür ışık (UV-Vis) absorpsiyon spektroskopi ve senkrotron toz XRD analizi ile belirlenmiştir. Sonuçlara göre, Co^{2+}'ın MFI çerçeve yapısındaki β ve γ-yerlerini tercih ettiği gözlemlenmiştir. Senkrotron tozu XRD analizine göre, en yüksek katyon oranı US-Y'nin Site III yakınında (süper kafeste) tespit edilmiştir ve bu yerleşim yeri hidrojen tarafından ulaşılabilirdir. Ni^{2+}-,Co^{2+}-ZSM-5 için teorik adsorpsiyon ısıları ($-E_{ads}$) periyodik ve küme yoğunluğu fonksiyonel teorisi (DFT) ile hesaplanmıştır. Co^{2+}-ZSM-5 üzerinde β-alanı ve γ-alanı ve ayrıca Ni^{2+}-ZSM-5 üzerinde ek bir α-alanı gözlemlenmiştir. Genel olarak, deneylerden ve yoğunluk fonksiyonel teorisinden (DFT) hesaplanan adsorpsiyon ısısı değerlerinin aynı aralıkta olduğu bulunmuştur.

Anahtar Kelimeler: hidrojen adsorpsiyonu, nikel, kobalt, Synchrotron x-ışını kırınımı, yoğunluk fonksiyonel teorisi

To my family

ACKNOWLEDGMENTS

As a new graduate engineer, I was not sure about many paths that I could take as my professional passion. Now, after two and a half years of working as a researcher, looking back, I feel blessed that this is the career path that flourishes my personality and my interests. During this period, I have developed as an engineer, academic, and most importantly as a person. For all of this, I would like to thank my supervisor Assoc. Prof. Dr. Bahar IPEK TORUN for her mentorship, patience, and belief that she has for me.

The project is funded by Middle East Technical University Research Grant No: BAP-GAP-304-2020-10275.

I wish to thank Asst. Prof. Dr. M. Oluş OZBEK for periodic density functional theory study (DFT) and Dr. Yasemin KAYA for cluster model density functional theory study contributions and their support throughout the process. In addition, TUBITAK ULAKBIM High Performance and Grid Computing Center is acknowledged for providing an opportunity for performing the DFT computations reported in this research.

I would like to thank beamline scientist Mahmoud Abdellatief from SESAME (Synchrotron-light for Experimental Science and Applications in the Middle East) for performing synchrotron powder X-ray Diffraction experiments.

I would like to thank also Prof. Dr. Alper UZUN for high pressure (298 K, < 50 bar) experiments performed at KUTEM (Tüpraş Energy Center).

Over this period, I have developed many valuable friendships in the department. Firstly, I would like to thank İklim GÖKÇE and Sezer OSMANAĞA for their support in the laboratory and their uplifting souls that always cheered me up on any given day. I also thank Sılay ÖNDER for relentlessly being there whenever I need

her both as a colleague and as a friend. Lastly, I thank the teaching assistants and professors whom I had the privilege to work with.

I am also grateful to my dearest friends Mervecan GÖKÇE and Şehnaz GENÇ for their emotional support even though sometimes life makes it hard for me to give back the friendship that they offered to me.

To my parents Neriman and Selami SAROHAN and my brother Burkay SAROHAN, I could not have done this without your support. They always helped me lift the heaviest weights off of my shoulders. From the darkest moments to the most joyful ones, there has not been a second that I felt alone.

Last but foremost, I would like to thank my love, Mert KELEŞ, whose position in my life cannot be described in words. Every experiment I have done, every sentence I have written carries his physical and emotional presence that will not be compensated in our lives. Not only in academics but also in every aspect of life he helps me find happiness and joy within the smallest details. For always making me believe in myself he deserves one of the biggest thanks there is.

TABLE OF CONTENTS

LIST OF TABLES

TABLES

LIST OF FIGURES

FIGURES

LIST OF ABBREVIATIONS

ABBREVIATIONS

XRD	X-Ray Diffraction
SEM	Scanning Electron Microscope
EDX	Energy Dispersive X-Ray Spectroscopy
ICP-OES	Inductively coupled plasma-optical emission spectrometer
BJH	Barrett–Joyner–Halenda Adsorption model
SDA	Structure direction agent
CTABr	Cetyltrimethylammonium bromide
HDA	1,6-diaminohexane
FCEVs	Fuel Cell Electric Vehicles
DOE	The U.S. Department of Energy
MOF	Metal Organic Framework
FT-IR	Fourier transform infrared spectroscopy
IUPAC	International Union of Pure and Applied Chemistry
DFT	Density Functional Theory
DR UV-Vis	Diffuse Reflectance (DR) UV–Vis

LIST OF SYMBOLS

SYMBOLS

b	Affinity constant, bar^{-n}
P	Pressure, bar
Q_e	Equilibrium solid phase concentration, $mmol/g$
Q_{max}	Maximum adsorption capacity, $mmol/g$
Qst	Isosteric heat of adsorption, kJ/mol
R	Ideal gas constant (8.314), $J/K*mol$
T	Temperature, K
ΔH_{ads}	Heat of adsorption, kJ/mol
λ	Wavelength, Å
1/n	Exponent
ΔH^0_{opt}	Optimum heat of adsorption (kJ/mol)

CHAPTER 1

INTRODUCTION

The global population is expected to reach 10 billion people by 2050, which will cause an exponential effect on energy requirements [1]. Although fossil fuels are the main source of energy generation, they cause economic and environmental issues because of the greenhouse gas emissions such as carbon dioxide, methane and nitrous oxide [2]. The highest emitted greenhouse gas is CO_2 by 79% and the total CO_2 emission amount has reached 36 billion metric tons in 2020. 20.27% of emitted total CO_2 is caused by the transportation sector, 36.51 % by the power industry, 21.74% by the industrial combustion [3]. The ultimate solution for high CO_2 emission is to find new renewable resources (e.g., solar, wind, hydro, and biomass) and energy carriers that come with a lower negative effect on the environment.

Hydrogen has been one of the most preferable energy carriers over the last 50 years. Apart from being the most abundant and lightest element with the highest gravimetric energy content in the universe, hydrogen is non-toxic, sustainable, and considered a clean energy carrier for transportation as its only combustion product is water[4]. The 7% rise in worldwide hydrogen demand from 2013 to 2020 demonstrates the growing appeal of hydrogen energy over time [5]. Currently, 96% of the hydrogen is obtained from conventional fossil fuels (natural gas 48 %, oil 30%, coal 18%) mainly through methane steam reforming process, and the remaining 4% from electrolysis methods (e.g., alkaline electrolysis, polymer exchange membranes (PEM), and solid oxide electrolysis cells (SOEC))[6].

The hydrogen has been used mostly in the ammonia production (51%), oil refining (31%), and the methanol production (10%) until recently. To this date, only 0.01% of hydrogen energy is consumed for transportation all around the world. The hydrogen consumption in a variety of sectors has been predicted to increase

according to the International Energy Agency Net Zero 2050 report [7]. Among the sectors, transportation including road transportation, aviation and shipping are expected to show high hydrogen demand to diminish large CO_2 emissions. It is planned to use almost half of the produced hydrogen (530 Mt) by 2050 in industry and transportation sectors as seen on Figure 1.1.

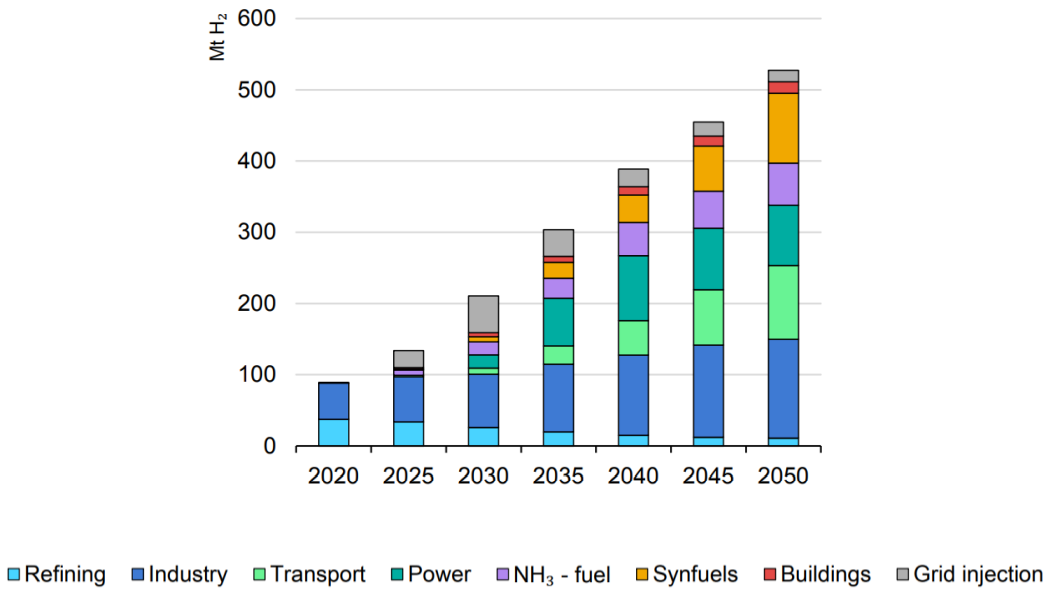

Figure 1.1 Potential hydrogen demand for different sectors [7]

Hydrogen energy in transportation shows itself in a wide spectrum of Fuel Cell Electrical Vehicles (FCEV) ranging from light duty vehicles to heavy duty trucks and aircrafts [8]. Globally, light passenger vehicles (PLDVs) are the most concentrated type of FCEV constituting in 2020, accounting for 74% of registered FCEVs, whereas buses cover only 16% of total FCEV stock. The transportation sector is paying increasing attention to FCEVs. Toyota, Honda, and Hyundai are just few examples of global FCEVs car manufacturers. At the end 2021, there were more than 40 000 FCEVs on the road around the World [9].

Fuel Cell Electrical Vehicles (FCEVs) use hydrogen as an energy carrier to convert hydrogen chemical energy to electricity through fuel cells [10]. Proton exchange membrane fuel cell (PEMFC) or solid oxide fuel cells (SOFC) are used to convert

the chemical energy in hydrogen and oxygen directly into electrical energy [11]. A single fuel cell is composed of three main parts: anode, cathode, and electrolyte. As demonstrated in Figure 1.2, hydrogen molecule passes through an anode where the catalyst causes the splitting of hydrogen molecule into proton and electrons in a fuel cell (Equation1.1). The membrane allows only the protons to pass while the electrons follow the external circuit to the cathode (Equation1.2). These electrons create electricity that can be used as a power. On the other side of the cell, oxygen coming from the air reacts with the proton hydrogen, and water is formed as the only product of this process [12].

$$Anode: H_2 \rightarrow 2H^+ + 2\,e^- \qquad \text{(Eqn.1.1)}$$

$$Cathode: \frac{1}{2}O_2 + 2H^+ + 2\,e^- \rightarrow H_2O \qquad \text{(Eqn.1.2)}$$

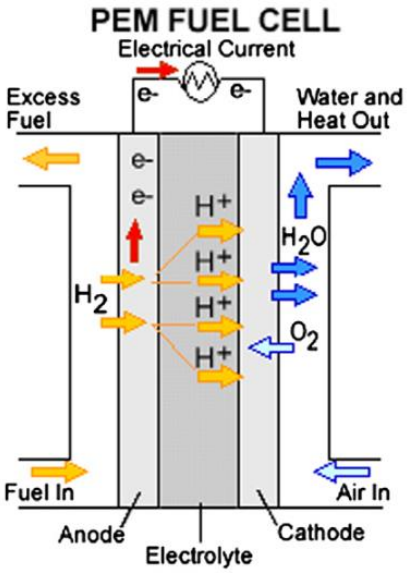

Figure 1.2 Schematic of PEM (Polymer Electrolyte Membrane) Fuel cell [13]

Although battery electric vehicles (BEV) have been used over the years for clean transport, there are key advantages that hydrogen powered fuel cells offer over electrical batteries. One main advantage of FCEVs is the high gravimetric hydrogen energy density of hydrogen has the capability to produce electricity up to 140 MJ/kg,

which surpasses the energy density of most batteries as can be seen in Figure 1.3 [14]. As stated above, fuel cells can be used in a variety of load selections while BEVs are mostly limited to light load conditions due to their inconvenient weight increase as the duty becomes heavier. That's why FCEVs are becoming more convenient for hard-to-electrify transport segment vehicles (e.g. long-haul, heavy-duty trucking, shipping and aviation). Furthermore, when the recharging times are compared between the two options, hydrogen fuel cells take the lead with a refill time of <5 mins for 300 miles range. Even for a driving range of 100 miles, BEV takes up to 60 mins to refill [15]. When these arguments are taken into consideration, using the hydrogen fuel cell option instead of an electrical battery in heavy duty vehicles (trucks, aircrafts, etc.) can be seen as a necessity.

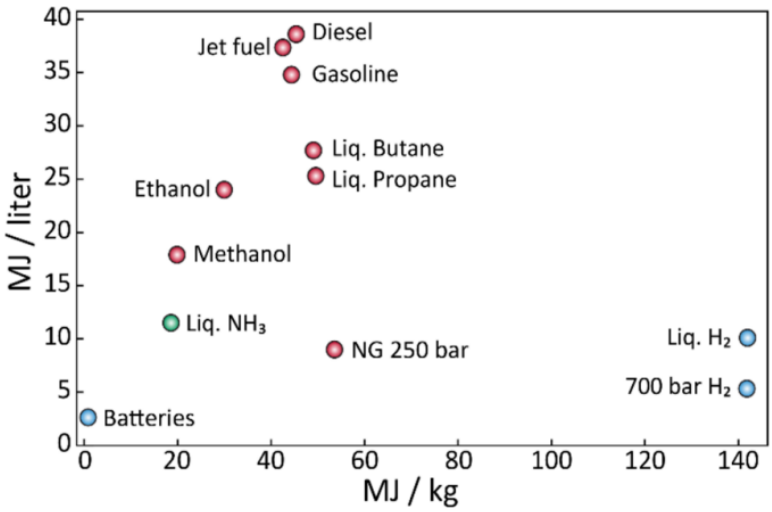

Figure 1.3 Volumetric and gravimetric energy densities of different energy storage applications [16]

As presented in Figure 1.3, H_2 has the highest gravimetric energy content. However, since the density of H_2 is quite low, the energy per metric volume is one of the lowest (10 MJ/L) at the moment. This dilemma brings out one of the main challenges to replace the conventional energy sources with hydrogen: which is efficient storage of H_2. Therefore, the challenge of implementing the hydrogen energy into transportation clearly lies on the question that is how much hydrogen can be stored in a specified volume.

CHAPTER 2

LITERATURE REVIEW

2.1 Hydrogen Storage

Hydrogen has a significant advantage with its high energy content (140 MJ/kg) but the volumetric energy content of H_2 is four times less than gasoline [17] due to the very low density of H_2 (1 kg of hydrogen/11 m^3 at ambient temperature and atmospheric pressure [18]). Therefore, efficient storage techniques (e.g., large storage tanks or faster-flowing pipelines) are required to be able to use hydrogen as an energy carrier, especially in portable applications under ambient conditions. The U.S. Department of Energy (DOE) in cooperation with U.S. Drive (Driving Research and Innovation for Vehicle Efficiency and Energy) has targeted comprehensive hydrogen storage limits (Table 2.1) for 300–500 miles driving range at one filling (3–5 min) in light-duty vehicles for ambient temperature and low pressure storage (<100 bar) [19]. Storage systems should be economically feasible, reversible at ambient condition, and provide safe operation. Expression of the hydrogen uptake capacity of materials is presented in terms of gravimetric and volumetric capacity. Gravimetric capacity expresses the weight percentage of hydrogen over the total amount storage materials and the term is generally used in material-based storage methods. Volumetric capacity is the amount of hydrogen stored inside the storage system. High gravimetric capacity is a necessity to obtain light on-board storage tank, while volumetric storage is crucial because of direct relation with the volume of the storage tank [20,21]. As demonstrated in Figure 2.1, there have been several hydrogen storage methods used and tried to be improved.

Table 2.1 DOE Technical Targets for Onboard Hydrogen Storage for Light-Duty Vehicles [19]

Target or Status	Gravimetric Capacity (wt% H_2)	Volumetric Capacity (g H_2 per L)
2020 Targets	4.5	30
2025 Targets	5.5	40
Ultimate Targets	6.5	50
700 bar compressed	4.2	24

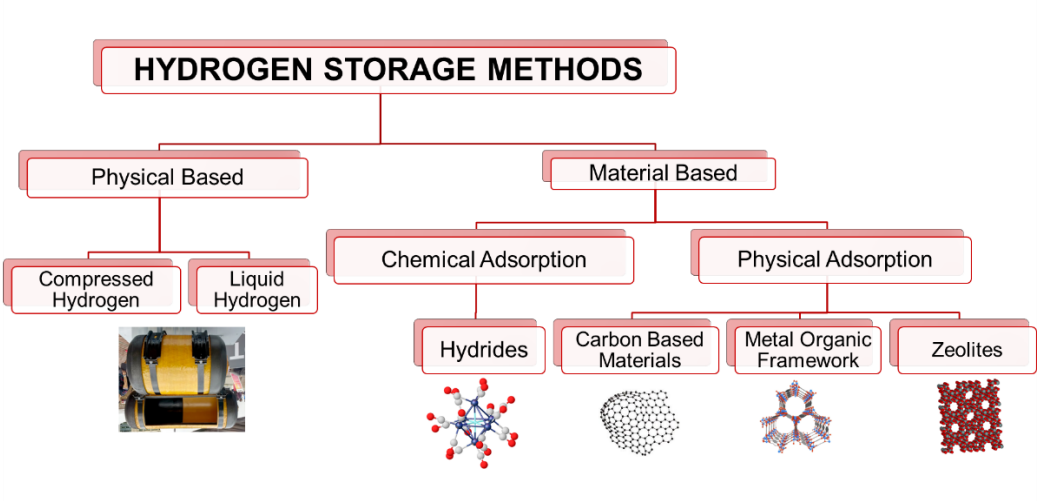

Figure 2.1 Classification of hydrogen storage methods [22]

2.2 Physical Based Methods

Physical based hydrogen storage methods consist of pressurizing of hydrogen at high pressures (700 bar) and liquefaction of hydrogen at low temperatures. Compressed hydrogen systems generally work between 350 to 700 bars in onboard storage systems. Pressurizing method is widely used in commercial FCEVs such as the recently launched Toyota Mirai 2021 in which the storage process is performed at 700 bars [7]. For ambient temperature storage, high pressure compression become insufficient for reaching DOE targets as can be seen in Table 2.1. Moreover, they

impose significant safety hazards to the vehicle which makes the redesign of the storage systems a necessity in such a way that lower pressured storage systems (< 100 bar) are required.

Liquefaction is based on increasing the density of hydrogen to almost 70 kg/m^3 at atmospheric pressure (approximately 848 times that of gaseous hydrogen) [24]. Hydrogen is stored in vacuum-insulated tanks below its boiling temperature (20 K at 1 atm) following the cooling at 33 K (hydrogen critical temperature). Even though this process appears to be volumetrically and gravimetrically efficient, more research is needed to address the issues of high hydrogen liquefaction rates, which could result in significant energy waste [25].

2.3 Material Based Methods

Among other possible techniques, material based H_2 storage is favored due to the possibility of compressing H_2 at lower pressure and higher temperature values via chemical or physical bonds. This section will be explained in detail in the following subsections.

2.3.1 Chemical Adsorption

Chemical adsorption (chemisorption) of hydrogen is based on the formation of the chemical bond between material and a hydrogen molecule. Hydrogen molecule is firstly adsorbed on the surface and dissociated to hydrogen atoms. Afterwards hydrogen atoms are chemically adsorbed on the surface. One class of the promising chemical adsorbent materials is conventional metal hydrides, which have been studied widely for stationary hydrogen storage [26]. Magnesium hydride (MgH_2) shows a reasonably high gravimetric capacity (7.6 wt.%) but suffers from the high binding energy ($-\Delta H$ = 66–75 kJ/mol H_2) that requires 663 K to desorb H_2 at 1 bar which causes reversibility problems at ambient conditions [27,28]. Although complex hydrides can meet the DOE gravimetric capacity target (e.g. 170 $Mg(BH_4)_2$

(14.9 wt%), $LiBH_4$ (18.5 wt%)), none can presently achieve the DOE's minimum delivery pressure, charging/discharging rates at the same time [29–31]. Intermetallic compounds and alloying methods have gain attention because of decreasing the thermodynamic limitation at ambient condition storage [32]. To illustrate, VH_2 and $LaNi_5H_x$, have moderately low heat of adsorption values compared to other hydrides ($-\Delta H = 30–43$ J/mol H_2), but heavy transition and rare earth metals in their structures result in limited gravimetric H_2 storage densities (1–2 wt.%) [33]. Another improvement is nanostructuring of the metal hydrides. When particle size decreases to the nanometer level, MgH_2 becomes thermodynamically destabilized and diffusion path becomes shorter for hydrogen molecules, resulting in fast kinetics. Ultrafine MgH_2 nanoparticles (4–5 nm) showed a reversible hydrogen storage capacity of 6.7 wt% at 303 K which has never been achieved before with hydrides. However, it still requires a high desorption temperature of 423 K [34].

2.3.2 Physical Adsorption

Physical adsorption is based on weak Van der Waals forces that enable fast adsorption/desorption kinetics as well as reversibility at ambient temperature and pressures below 100 bar. The ultimate pressure is stated as 100 bar while the lowest pressure is demonstrated as 5 bar for the swing physical adsorption process of hydrogen. The reason for determining the low-pressure level is the non-availability of H_2 in the tank for the materials having high binding energy with hydrogen [35]. Metal organic frameworks (MOF), carbon based materials and zeolites are the most often studied porous materials that can physically adsorb hydrogen [35]. Under ambient temperature conditions, which does not favor densification of H_2, strong interaction between the walls and the H_2 molecules are required to maximize the van der Waals interactions. This is due to the fact that hydrogen has no charge or dipole moment, low quadrupole moment ($2.21*10^{-40}$ C m^{-2}) and low polarizability ($8.79 * 10^{-41}$ C^2 m^2 J^{-1})[36].

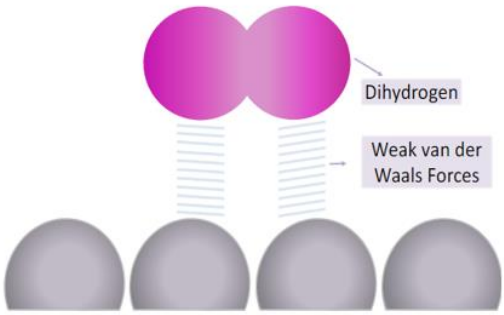

Figure 2.2 Schematic representation of weak van der Waals Forces between material and hydrogen molecule [37]

2.3.2.1 Optimum Heat of Adsorption

The interaction of H_2 with the adsorbent surface is generally quantified by the heat of adsorption that should be in the optimum range to obtain high storage capacity as well as reversibility on porous materials. Optimum thermodynamic requirement is studied by Bhatia and Myers via Langmuir adsorption model (Equation1.3), which maximizes the working capacity between adsorption pressure and desorption pressure [38].

$$\Delta H^0_{opt} = T\Delta S^0 + \frac{RT}{2}\ln\left(\frac{P_{ads}P_{des}}{P_0^2}\right) \qquad \text{(Eqn.1.3)}$$

Although, the heat of adsorption of adsorption vary as loading amount increases on the surface or due to surface heterogeneity, the stated Langmuir Isotherm based model represents the average or integral heat of adsorption (ΔH^0_{opt}). In Bhatia and Myers study, optimum heat of adsorption is calculated as -15.1 kJ/mol ($\Delta S° = -8R$ for a variety of adsorbents) for 298 K and 1.5–30 bar cycling adsorption process. According to extrapolation on adsorption heat of adsorption versus entropy for hydrogen adsorption on several cation exchanged zeolites, it was suggested that optimum heat of adsorption on zeolites should be in the range $-\Delta H^0_{opt} = 22 - 25\ \mathrm{kJ/mol}$ [39]. On the other hand, Grand Canonical Monte Carlo simulation on different MOFs shows the optimal heat of adsorption should be in the narrow range

such $-\Delta H^0_{opt} = 18.5 - 25\ kJ/mol$ [40]. In the scope of these studies, it can be concluded that the optimum heat of adsorption on porous materials should not exceed 25 kJ/mol to obtain reversibility for 30−1.5 bar operating pressure range at 298 K.

In addition to the strong polarizing centers on the adsorbent materials, pore sizes and distribution are essential in order to obtain optimum heat of adsorption and high volumetric hydrogen uptake [35]. Absolute values for heat of adsorption steadily increase with the decreasing pore size due to increased interaction with the hydrogen molecules [41]. In order to design a suitable hydrogen storage on-board system based on DOE constraints, both gravimetric and volumetric capacity should be balanced by using materials that have high isosteric heat values and low pore openings (<1 nm) [42–45]. Although gravimetric capacity of porous materials can be increased by increasing total surface area, it is not the case for volumetric storage as can be seen in the Figure 2.3.

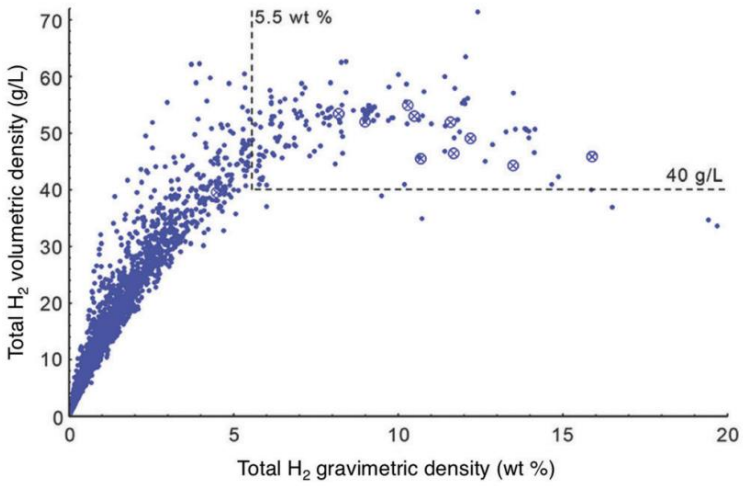

Figure 2.3 Theoretical total volumetric vs. gravimetric capacities for various MOFs at 77 K and 35 bar [46]

There are few optimization study for balancing gravimetric and volumetric storage capacities on MOFs. In the study of Allendorf et al., different MOFs are analyzed in terms of volumetric and gravimetric capacities at 77 K and 100 bars [35]. The results show that even though the gravimetric capacity proportionally increases with the surface area or pore size, the proportionality relation with the volumetric capacity is

limited. According to the findings, optimization limits and obtained ranges are given in Table 2.2.

Table 2.2 Ranges of various crystallographic properties that optimize volumetric and gravimetric capacity for MOFs [21]

Properties	**Range**
Pore volume (cm^3/g)	0.4–0.5
Pore diamater (nm)	1–2
Gravimetric surface area (m^2/g)	4500–5500

2.3.2.2 Metal Organic Frameworks

Metal organic frameworks (MOFs) are crystalline porous materials that can have internal surface area values higher than 6000 m^2/g. They include a variety of organic linkers and inorganic components (metal ions) in their structures, as shown in Figure 2.4, showing a range of adsorption energy values as well as varying surface areas. One of the main advantages of metal organic frameworks is their permanent highly ordered porosity. Hence, MOFs are one of the preferred materials in the application of clean energy and in the storage of hydrogen, methane, carbon dioxide and others [47,48].

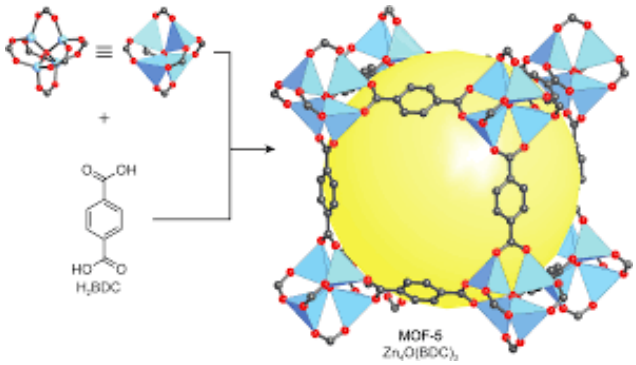

Figure 2.4 The structure of MOF-5 shown as Zn_4O tetrahedra (blue polyhedra) joined by benzene dicarboxylate linkers (O: red and C: black) to give an extended 3D cubic framework [49]

Hydrogen storage capacities of several MOFs are listed in Table 2.3 for ambient temperatures and 77 K experiments. At elevated pressures (>20bar) and 77 K, porous materials show increasing uptake performance with the increasing surface area as the general trend namely Chahine's rule (1 wt% of uptake is obtained for every 500 m^2/g of surface area)[50]. The mentioned trend can also be seen on the table. Although MOFs show significant gravimetric hydrogen uptake capacity at cryogenic temperature and high pressure, their capacities become insufficient for the DOE standards at ambient temperatures (<2 wt%) [51]. Large pore diameter of the MOF structures are the main bottleneck to sustaining high affinity with hydrogen at ambient conditions [52].

In general, two main strategies have been followed to increase the hydrogen uptake capacity of MOFs at low pressure and ambient temperature environment. The first one is to narrow the pores and the second one is to create coordinatively unsaturated metal centers to increase the affinity for H_2 through strong metal-hydrogen interactions [53]. Various metal sources have been utilized in the synthesis of MOFs, such as Zn, Cu, Mn, Co, Cr, Ni, lanthanide metals, alkali metals, Mg, and Al [54–57]. Among the MOFs, the highest gravimetric uptake capacity is reached with $Be_{12}(OH)_{12}(BTB)_4$ as 2.3 wt.% at 95 bars under the ambient condition but it is still below the stated DOE targets.

Table 2.3 Surface area, H_2 uptake capacity and heat of adsorption of H_2 adsorption data of metal organic frameworks

MOF	Surface Area (m^2/g)	77 K (wt.%)	Ambient Condition (wt.%)	$-\Delta H_{ads}$(kJ/ mol)	Ref
PCN-10	1779	5.2(45bar)	-	7–4	[58]
IRMOF-11	2180	3.5(34bar)	-	-	[59]
MOF-5	4170	5.2(48bar)	-	4.8	[60]
MOF-5	4170	11.5(180bar)	-	4.8	[60]
MOF-205	4460	6.5(80bar)	-	-	[61]
MOF-177	4500	7.5(70bar)	-	4.4	[62]
NU-100	6143	16.4(70bar)	-	-	[63]
MOF-5	2296	5.1(65bar)	0.28(65bar)	3.8	[64]
MIL-100	2700	3.3(26.5bar)	0.15(73bar)	6.3	[52]
MIL-101	5500	6.1(80bar)	0.43(80bar)	10	[52]
$Be_{12}(OH)_{12}(BTB)_4$	4030	9.2(100bar)	2.3(95bar)	-	[65]
Ni_2(dhtp)	1131	2.5(100bar)	-	13	[66]
Co_2(dhtp)	1173	2(100bar)	-	11.5	[66]
Co-PCN-9	1355	1.5(1bar)	-	10	[67]
Ni_2(m-dobdc)	-	5(100bar)	1(100bar)	13.7	[68,69]
Co_2(m-dobdc)	-	-	0.95(100bar)	12.1	[68,69]

Among different metal loaded MOFs, nickel and cobalt cations gain attention due to their high initial heat of adsorption values. High partial positive charges and polarizability of the nickel and cobalt cations enable them to have high initial heat of adsorption values ranging 5.2–13 kJ/mol [57,67,70–74].

Although MOFs show high volumetric capacity (<60 g H_2/L crystal) at high pressures (<100bar) and at 77 K environment [75,76], reported highest volumetric storage capacity under ambient conditions among the MOFs belongs to Ni_2(m-dobdc) by 11 g/L at 100 bar [69] which is still below the DOE targets. This is mainly caused by the large pore diameters of the MOFs and their loss of efficiency in terms of volumetric capacity.

2.3.2.3 Carbon Based Materials

Porous carbons, carbon aerogels, activated carbons, carbon nanotubes, and nanofibers are some carbon structures that have been investigated for hydrogen storage applications [77]. Among the carbon based materials, one example of porous activated carbon AC-K5 shows a high gravimetric capacity of 7.08% at 77 K and 20 bar with a high surface area (3190 m^2/g) [78]. Higher hydrogen capacities are achieved with zeolite-templated carbon materials (synthesized by carbonization within a zeolite template). In the study of Masika et al, zeolite 13X is used as a template to generate ultrahigh surface area carbons (3332 m^2/g) showing 7.3 wt% at 20 bar and 77 K [79]. Moreover, carbon single- and multiwall nanotubes (SWCNTs and MWCNTs) are promising adsorbents for hydrogen storage systems. Li-doped and K-doped multi-walled nanotubes (MWNTs) show a hydrogen uptake capacity of 20 wt.% and 14 wt.%, respectively under ambient temperature and pressure, but very high temperatures (473 to 673 K) are needed for desorption of hydrogen[80]. Although some of the porous materials can show high storage capacity at 77 K, their capacities become lower than 2 wt.% in a general trend [81,82].

2.3.2.4 Zeolites

Zeolites are highly ordered, microporous crystalline aluminosilicates, that share a general chemical formula as $M^{+}_{x/n}(AlO_{4/2})^{-}_{x}(SiO_{4/2})_{y}\cdot zH_2O$. They are composed of tetrahedrally coordinated Si and Al atoms, ($AlO_{4/2}^{-}$ and $SiO_{4/2,}$ and other tetrahedral atoms such as P, Fe, Ga, etc. in zeotypes), coordinating oxygens, extra-framework cations ($M^{+}_{x/n}$) and water molecules [83]. Combination of silica and aluminum tetrahedral building blocks form secondary building units (SBUs) that can be a single ring or a double ring (4 member rings, (4MR), 6MR, 8MR, 10MR up to 30MR). More complex units called Composite building units (CBUs) are constructed by the arrangement of SBUs. They can be seen in the form of a double 6 member ring (d6MR), sodalite cage (sod) or super cage [83]. Cages are generally seen at the intersection of two channel systems. Eventually, combination of different SBUs create different frameworks that are named with the three letter codes such as MFI, FAU and MOR, etc. which can be seen in Figure 2.5.

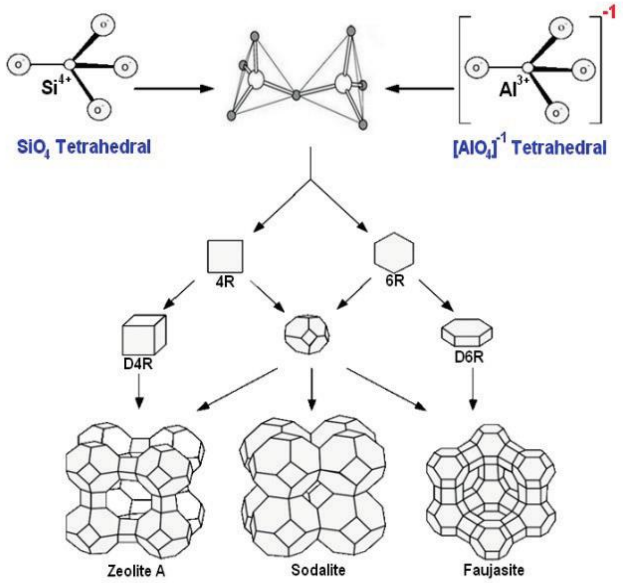

Figure 2.5 Zeolite formation from the tetrahedrals [84]

The zeolites are generally classified with their pore sizes and Si/Al ratio. Zeolites classifications are given in Table 2.4 with a few examples of frameworks. The silicon

to aluminum ratio in zeolites is essential in determining their chemical properties such as the maximum cation content and acidity. Since Al–O–Al linkages cannot be formed in the structure (Loewenstein's Rule), Si/Al should be greater than 1 or equal.

Table 2.4 Classification of zeolites [83]

Class of zeolite	**Si/Al**	**Type of zeolite**
Low silica	1-1.5	A, X, LSX, sodalite
Intermediate silica	2-5	Y, L, mordenite, Erionite
High silica	10-∞	ZSM-5

The negative charge on the framework is caused by aluminum tetrahedra $(AlO_4)^-$ that is generally balanced with alkali or alkaline-earth metal cations ($M^+_{x/n}$) such as Na^+, Li^+, K^+ and Ca^{2+} [85]. Cation loading capacity and pore size tunability (3.4 to 20 Å) of zeolites make them a preferable porous material for adsorption and ion-exchange processes [86–89]. Alkali-alkaline metal cations provide them the ability to have strong interaction with hydrogen, resulting in promising gravimetric and volumetric storage capacities [85]. In Table 2.5, some of the reported H_2 storage capacities of zeolites are listed.

Table 2.5 H_2 uptake capacity data of alkali metal and alkaline earth metal exchanged zeolite

Zeolite	Gravimetric Capacity(wt.%)	Temperature	Pressure (bar)	Reference
Na-A	0.1	293 K	10	[90]
Na-Y	0.28	298 K	15	[91]
H-ZSM-5	<0.1	303 K	31	[92]
H-ZSM-5	0.72	77 K	0.66	[93]
H-SSZ-13	1.28	77 K	0.92	[94]
Li-MOR	1.12	77 K	1	[95]
Na-ZSM-5	0.87	77 K	1	[95]
Na-FAU	1.21	77 K	1	[95]
SAPO-34	1.4	77 K	1	[96]
Ca-X	2.19	77 K	15	[85]
Na-Y	1.81	77 K	15	[85]
Na-X	2.55	77 K	40	[97]

In the zeolites, hydrogen storage firstly takes place on the sites that show high affinity with hydrogen at low loadings. Afterward, other cation sites showing lower binding energy to hydrogen are started to be filled. Then, the pore walls of the material are started to be interacting with hydrogen. At this step, hydrogen can be in interaction with framework oxygen atom or another hydrogen molecule. As pressure is increased, firstly interior of micropores (< 2 nm pore opening) is filled with hydrogen (~ 50 bar) and this step is followed by the filling of larger pores (2–50 nm, mesopores) which can be seen at high pressures (≤ 100 bar) [38].

The small pore size advantage of zeolites as well as the extra-framework cation adsorption centers provide them high interaction with hydrogen, resulting in high heat of adsorption compared to other porous materials (e.g., MOFs and carbon based materials) [35].

Adsorption microcalorimetry, isosteric heat method and Fourier transform infrared spectroscopy (FT-IR) are three classical methods that have been widely used to determine the heat of adsorption on zeolites. Hydrogen binding energy to the extra-framework cation on zeolites is also inferred from the bathochromic shift of the free H_2 stretching vibration (Raman active, 4163 cm^{-1}) on FT-IR. Larger bathochromic shift values indicate stronger perturbation of H_2 molecule, therefore, stronger binding energy values. The summary of the IR vibration of hydrogen and calculated heat of adsorption values (-ΔH) of different extra-framework exchanged zeolites are given in Table 2.6 [98].

Isosteric heat of adsorption (Q_{st}) measures the change of enthalpy when adsorbate molecules are adsorbed from the bulk gas phase to the adsorbed phase. It provides a measure of heterogeneity for the gas–solid interfaces [99,100] Following the Clausius-Clapeyron equation, the isosteric heat equation is finalized as shown in Equation.2.1.

$$\left(\frac{\partial \ln P}{\partial (1/T)}\right)_n = \frac{Q_{st}}{R} \qquad \text{(Eqn.2.1)}$$

Table 2.6 H–H stretching wavenumber and heat of adsorption values of alkali and earth alkali metal containing zeolites

Zeolites	Si/Al	H–H Stretching Wavenumber (cm^{-1})	-ΔH (kJ/mol)	Calculation Method	Reference
Li-FER	8.5	4090	4.1	FT-IR	[101]
Na-FER	8.5	4100	6	FT-IR	[101]
K-FER		4111	3.5	FT-IR	[101]
Na-ZSM-5	25	4101	10.3	FT-IR	[102]
K-ZSM-5	25	4112	9.1	FT-IR	[102]
(Mg,Na)-Y	2.4	4056	17.5	FT-IR	[103]
Ca-Y	2.4	4078	15	FT-IR	[104]
Na-ZSM-5	25		6	Qst	[105]
Na-FAU	2.8		6.1	Qst	[105]
Na-MOR	6.5		11.7	Qst	[105]
Li-MOR	8.9		12.1	Qst	[95]
Li-MFI	12		10.9	Qst	[95]

Cu, a transition metal, demonstrates high isosteric heat of adsorption values on ZSM-5 (73–39 kJ/mol) and SSZ-13 (48–16 kJ/mol) due to its unusual strong interaction with H_2 molecule [106,107]. This phenomenon is caused by increased Cu(I) ($3d\pi$)→ H_2 (σ^*) back donation in the presence of Kubas type structure (Cu(I)(η^2-H_2)) [107–109].

Although Cu(I)-exchanged zeolites are investigated in terms of heat of adsorption and hydrogen storage capabilities, other transition metals such as Co and Ni are not

as often studied and a thorough investigation of hydrogen interaction with Co^{2+}- and Ni^{2+}-exchanged zeolites is need. So far, the following studies have been conducted about the hydrogen attraction behaviors of Co and Ni.

The interaction of H_2 and Ni^{2+}- or Co^{2+}- ZSM-5 are studied using Diffuse Reflectance Infrared Fourier Transform (DRIFT) method at 77 K. H–H stretching vibrations are presented for Ni^{2+}-ZSM-5 (ν = 3866, 3928, 3967 cm^{-1}, Si/Al = 25) and Co^{2+}-ZSM-5 (ν = 3904, 3980, 4010 cm^{-1}, Si/Al = 25) [110,111]. On the other hand, adsorbed hydrogen molecules show 4110 cm^{-1} frequency when they bind to Na-ZSM-5 at 77 K [112]. Since the vibration frequency shift are higher when H_2 molecule interacts with Ni^{2+} and Co^{2+} cations when compared to the shift of H_2 frequency when interacted with Na^+ cation, higher heat of adsorption values are expected on from Ni^{2+} and Co^{2+} cations when compared to that of Na-ZSM-5 ($-\Delta H_{ads}$ = 10.3 kJ/mol experimentally) [98].

Parallel to this assumption, Co^{2+}- and Ni^{2+}- exchanged zeolite-Y gives -17 kJ/mol heat of H_2 adsorption, which was calculated based on paramagnetic shifts observed in the NMR spectra of adsorbed H_2 molecules [113]. In another study, the adsorption energy of reduced Ni^+-ZSM-5 is reported as -67.4 kJ/mol using the density functional theory [114]. Moreover, storage capacity of Ni-Na-Y (Si/Al = 3, Ni/Al = 0.42) is reported as 0.92 wt.% at 77 K and 1 bar [115].

When the aforementioned heat of adsorption values and hydrogen storage capacities of Ni and Co loaded MOFs are also taken into account, investigation of hydrogen storage on Co^{2+}- and Ni^{2+}-exchanged zeolites seems promising to reach the optimum heat of adsorption values and high storage capacities on zeolites. Therefore, US-Y and ZSM-5 are chosen as a storage material for this study because of the properties mentioned in the sections 2.3.3 and 2.3.4.

2.3.3 Zeolite-Y

The framework structure of Zeolite Y (FAU) is characterized by the double-6-membered rings (D6R). In FAU framework, sodalite cages are bound to form supercages having pore openings of 0.74 nm and a cage size of 1.41 nm x 1.56 nm. There are six main cation sites (I, I′, II, II′, III, and III′) on FAU framework that are observed in the unit cell as demonstrated in Figure 2.6. According to Ni-Zeolite Y studies, cations are located mostly at the Site I (at the center of the double-6-membered ring), Site I′ (at the window of 6-membered ring towards the sodalite cage), Site II (at the 6-membered ring window towards the supercage) and Site II′ (inside the supercage)[116–118]. However, Monte Carlo simulations showed that sites I and I' are not accessible for hydrogen due to small pore sizes of 2.5 Å [115].

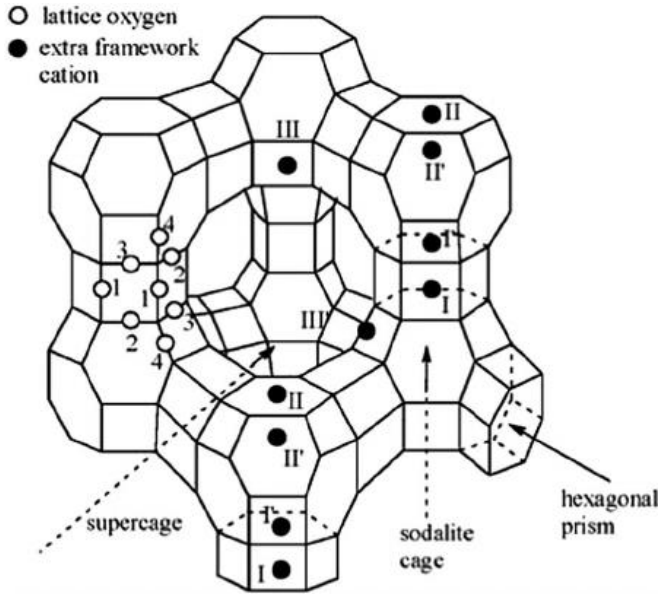

Figure 2.6 Faujasite (FAU) zeolite structure and positions of their potential charge compensating cations [119]

Ultra-stable Y (USY) zeolite is obtained from Zeolite-Y (~ 0.3 cm^3/g) by the dealumination method and this zeolite can have a total pore volume up to 0.5 cm^3/g with a higher stable structure compared to Zeolite-Y [120,121]. According to Vitillo et al., the maximum total storage capacity of the FAU framework, having 0.34 cm^3/g total pore volume, is 2.86 wt.% [122]. Therefore, US-Y is studied in this research

due to high pore volume and surface area values that can provide high storage capacity at ambient temperature and high pressures (< 100 bar).

2.3.4 ZSM-5

ZSM-5 (MFI topology, Si/Al 12–∞) is a member of high-silica crystalline aluminosilicates with a wide range of applications as zeolite-based catalyst and sorbent. The TO_4 tetrahedra (T atom=Si,Al) are interconnected in a framework, forming intersected pores (5.4×5.6 and 5.1×5.5 Å) with ten-member ring-openings (10 MR) [123]. MFI framework type consists of eight 5MR that emerge as a pentasil chain. The framework also contains straight and sinusoidal 10 MR channels that intersect to form larger cavities.

There are three main cation sites on the MFI framework [124] as shown in Figure 2.7. Alpha(α) sites are coordinated to four framework oxygen atoms that are located on the main straight channel's walls. Beta(β) sites are coordinated to oxygen atoms in distorted 6MR that are located at the intersection of straight and sinusoidal channels. Lastly, gamma sites(γ) are located on the wall of the sinusoidal channel [125,126]. All of the mentioned sites are accessible by hydrogen [127].

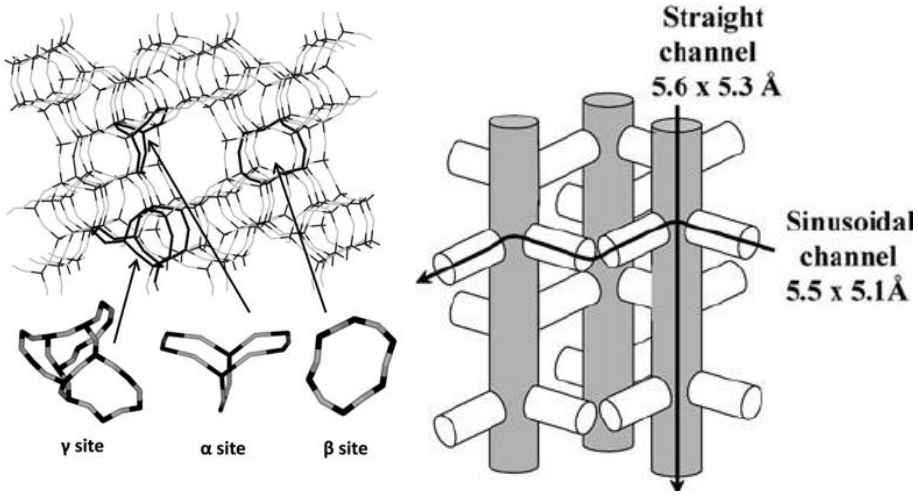

Figure 2.7 MFI framework and structure of α, β, γ sites [128,129]

Despite the advantages of ZSM-5 in terms of accessibility of cation sites and narrow pore openings (<1 nm), its total pore volume is limited. According to the theoretical hydrogen adsorption capacity calculations of Vitillo et al., the MFI framework can store a maximumly of 1.69 wt.% for 0.197 cm^3/g total pore volume [122]. Therefore, secondary porosity added to the structure would increase the total pore volume and the surface area, which can result in higher hydrogen storage capacity on the ZSM-5. The novel strategies for obtaining secondary porosity are given in the next section.

2.4 Mesoporous Zeolites

There are mainly three types of pores present in zeolites; pores with < 2 nm are named ‘micropore’, pores that have 2–50 nm diameter are named ‘mesopore’ and macropores have pore opening higher than 50 nm according to the International Union of Pure and Applied Chemistry (IUPAC) [130]. Zeolites that have at least two levels of pore types are considered hierarchically structured zeolites. The methods for constructing hierarchical zeolites are classified into two main methods named bottom-up and top-down as it is shown in Figure 2.8 [131,132].

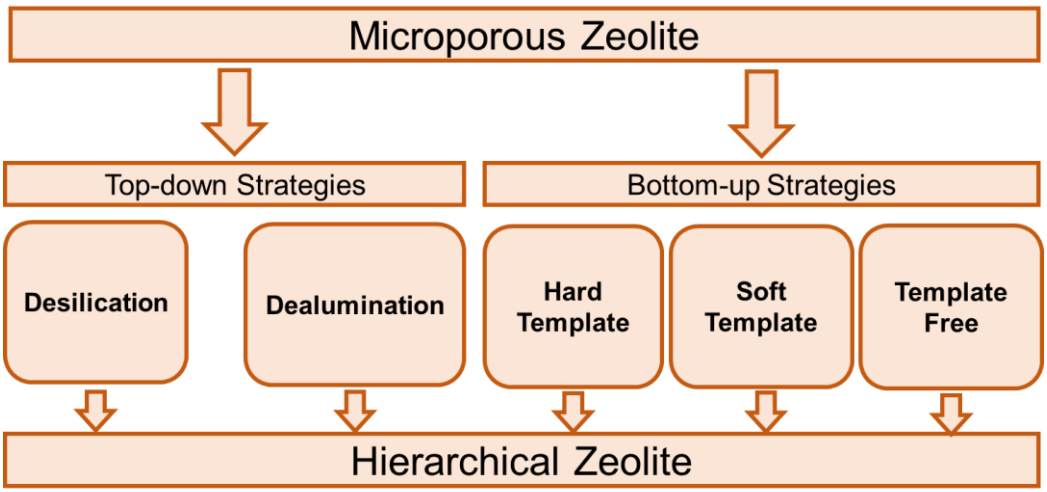

Figure 2.8 The schematic representation of main hierarchical zeolite formation strategies [131]

Hard template and soft template methods are based on introducing mesopore template (e.g. carbon nanoparticles, aerogel for hard template and e.g. surfactant or polymers for soft template) in the mother solution of zeolite during crystallization. In both methods, the template is removed from the zeolite by calcination at high temperatures (>773 K) after zeolite synthesis [132]. Templating using surfactants also reveals a different method known as the 'dual-templating method'. Structural directing agent (SDA) and mesoporogen are used in the zeolite synthesis gel together in this proposed method [133]. The surfactant directs the secondary porosity while SDAs construct the zeolite's micropores and main channels [134].

The top-down methods are also named the 'post-synthetic methods' since it is applied after crystallization as different from the bottom-up strategies. Desilication and dealumination are the main methods that are used. Dealumination is based on removing aluminum tetrahedral atoms from the structure in an acidic medium (e.g. nitric acid and hydrochloric acid) [135], while desilication is applied in a basic medium (NaOH) to remove silica atoms from the zeolite [136]. Intracrystalline mesoporosity is obtained as a result of the two methods. On the other hand, these methods can be also used to change the Si/Al of synthesized zeolites [137]. Specific to the desilication method, it is essential to adjust Si/Al ratio since removing silica from the framework can be prevented with the high amount of aluminum content in Si/Al<25 zeolites. Intermediate Si/Al ratios (25–50) are stated as the optimum range to obtain high mesoporosity. High silica content (>50) can result in larger pores (macropores) after desilication rather than mesopores. Although the optimum temperature is stated as 338 K for the desilication, as Si/Al decreases (<25), increasing temperature (358 K) is required to obtain extra mesoporosity [136].

The mentioned methods soft template and desilication are studied for obtaining ZSM-5 having a high pore volume (~ 0.5 cm^3/g). The soft template method provides better control of the mesoporous structure and obtaining narrow pore size distribution; however the cost of this method is higher compared to the desilication method. On the other hand, the desilication method enables a high probability to

scale up, but the mesopore formation on the framework is less controllable compared to the soft template method.

After adding extra porosity to ZSM-5, cation loading to zeolites is performed in this research. Although there are only a few related studies about hydrogen storage on nickel or cobalt loaded zeolites in literature [113–115], some introductory information relating to Ni, and Co cations on zeolites are given in section 2.5.

2.5 Ni, Co Cations on ZSM-5 and Zeolite Y

Nickel or cobalt loaded zeolites have been used in the different applications: catalytic reduction of NOx with methane [138], biomass pyrolysis [139], hydrogen production via CO_2 reforming of methane [140], methanol to hydrocarbons reaction [141] and dry reforming of methane [142]. The cation loading process in zeolitic materials is strongly influenced by the pH of the solution because it has a strong impact on the zeolitic structure and concentration at the active site. Depending on the Si/Al ratio, cobalt content, preparation method and pH; different species are formed such as M^{2+}, $M(OH)_2$, $M(OH)^{-}_3$ and $M(OH)^{2-}_4$. When pH >7, precipitation of $M(OH)_2$ plays the main role in the loading of M^{2+}. In the large cavities of the zeolite framework, transition metal cations can form complexes with simple molecules as a ligand. On the other hand, metal ions in acidic medium are mainly present in positively charged forms with two or three charges (M^{2+} and M^{3+}) [143,144].

Cation distribution and location are directly related to the AlO_4^- tetrahedra intensity and location in zeolites. In the zeolite framework, the maximum M^{2+} cation amount with respect to aluminum can be 0.5 because 2 aluminum tetrahedra neutralize one divalent cation. There are two main aluminum coordination types that are seen on the silica rich zeolites as stated in the Dedecek et al., 2012 [145] i.e., Al-O-(Si-O)$_2$-Al or Al-O-(Si-O)-Al sequences in one ring (denoted as Al pairs, Al_{2Al}) that balances the divalent cations . This arrangement is detected by Diffuse Reflectance UV-Vis by using Co^{2+} ions showing detectable d-d electron transition when they coordinated

with pair Al sequence on the framework. On the other hand, single Al atoms (Al_{1Al}) in those Si–Al sequences are able to charge balance only monovalent ions or monovalent metal-oxo complexes.

In order to observe the interactions between the cation loaded zeolites and hydrogen, the oxidation states and the distribution of the cations are needed to be understood. However, it is hard to detect the metal sites via XRD because of the low concentrations and random distributions of the cations. The information about Ni and Co loaded ZSM-5 and Zeolite-Y have been obtained in an indirect way from UV–Vis spectra [144,146–149], diffuse-reflectance Fourier-transform infrared spectroscopy (DRIFT) [110,111,126,150–155], X-ray photoelectron spectroscopy (XPS) [156] and Synchrotron powder X-Ray Diffraction (SXRD) [116].

2.6 Objective of the study

The objective of this study is to reach DOE (Department of Energy) hydrogen storage targets (5.5 wt.%, 40 g H_2/L) for light-duty FCEVs by using mesopore added ZSM-5 and US-Y under ambient temperature and pressures lower than 100 bar. ZSM-5 and US-Y are chosen as a sorbent material due to advantages they provide. ZSM-5 is a promising material in terms of narrow pore channels (< 1nm) and accessible main cation sites while US-Y is seen as a promising material due to high pore volume and surface area. One of the aims is to observe Ni^{2+} and Co^{2+} heat of adsorption performances on ZSM-5 and US-Y at ambient temperature, therefore hydrogen storage experiments are performed for three different temperatures up to 10 bar to calculate the isosteric heats of the samples. Another objective is adding secondary porosity to ZSM-5 to overcome pore volume restriction by the desilication and soft template methods. It is also aimed to obtain the same total pore volume (~0.5 cm^3/g) on ZSM-5 and US-Y samples to compare the performances of zeolites based on their frameworks at high-pressure experiments (< 100 bar). It is also aimed to analyze cation site distribution on zeolites to investigate the site-dependent adsorption energies. Hence UV–Vis spectra of dehydrated samples, as well as

synchrotron XRD data and Rietveld Refinement studies are performed. Site-specific H_2 adsorption energy values are also theoretically investigated using density functional theory.

CHAPTER 3

EXPERIMENTAL PROCEDURE

An experimental procedure consisting of the preparation of Co^{2+}-ZSM-5-Soft Template, Meso-Na,Co^{2+}-ZSM-5, Meso-Na,Ni^{2+}-ZSM-5, Micro-Ni^{2+}-ZSM-5, Micro-Co^{2+}-ZSM-5, Meso-Ni^{2+}-ZSM-5, Meso-Co^{2+}-ZSM-5, Ni^{2+}-US-Y and Co^{2+}-US-Y. Ion exchange details, characterization techniques, and hydrogen storage test procedures are given after the preparation of zeolites.

3.1 Preparation of Zeolites

During the preparation of zeolites two main objectives are targeted: obtaining 0.5 cm^3/g total pore volume for ZSM-5 and reaching high metal content on the zeolite. The soft template and desilication methods are used for ZSM-5 in order to reach 0.5 cm^3/g total pore volume. The procedure for the soft template method is given in section 3.1.1 and it was expected to reach 0.5 cm^3/g total pore volume according to the results of the mentioned article. The desilication method is performed according to Groen et al. study shows the results of ZSM-5 samples having different initial Si/Al ratios [136]. For the zeolites having Si/Al<25, an increase in the total pore volume is achieved only by 0.3 cm^3/g. On the other hand, for the zeolites having Si/Al>40, the macropores are formed rather than mesopores which are not preferred for hydrogen storage on porous materials. The Si/Al range of 25–50 appears to be optimal for mesopore formation upon desilication. Therefore, the appropriate starting Si/Al ratio (~30) and desilication method conditions (0.2 M NaOH for 30 min at 358 K) are chosen for reaching 0.5 cm^3/g total pore volume according to Groen et al. [136].

3.1.1 Co^{2+}-ZSM-5-Soft Template

Mesoporous ZSM-5 is synthesized hydrothermally following the gel formula reported by Xue et al [134] with the gel formula $1SiO_2$:0.0167 Al_2O_3:0.13K_2O:0.14HDA:0.1CTABr:60H_2O. KOH is used in the synthesis to dissolve silica source more efficiently rather than NaOH [157]. Firstly, 0.48 g KOH (Merck, %99) and 0.307 g $NaAlO_2$ (Sigma Aldrich, %37-45 Na_2O, %50-56 Al_2O3) are dissolved in 53.56 g de-ionized water. After that, 1.85 g cetyltrimethylammonium bromide (CTABr, Sigma Aldrich, %98) and 0.2 g 1,6-diaminohexane (HDA, Sigma Aldrich, %98) are added and the stirred until a homogenous solution is obtained. 2.98 g fumed silica (Sigma Aldrich, %99.9) is added slowly and stirred for 6 h using a magnetic stirrer at room temperatur. HDA is used as the structure directing agent (SDA) and CTABr as the mesoporogen for the synthesis of hierarchical porous ZSM-5 in this synthesis. The homogenous mixture is then transferred to 35 mL Teflon-lined autoclaves for hydrothermal synthesis at 423 K for 28 days. After synthesis, Teflons are quenched in cold water and then the zeolite is separated using vacuum filtration and a membrane having a pore diameter of 200 nm (ISOLab) until a pH of 7 is obtained. Following drying at 333 K for one day, the resulting sample is calcined at 853 K for 10 hours (using a 1 K/min heating rate) in a muffle furnace to remove organic residues coming from CTAB and HDA. The resulting zeolite is labeled as Na-ZSM-5-Soft Template.

Calcined 1 g of ZSM-5 is NH_4^+-exchanged using 500 ml 0.2 M NH_4NO_3 (Sigma Aldrich, 99 wt.%) solution at 353 K for 3 h. Afterwards, the zeolite is vacuum filtered and dried at 333 K for 1 day. The exchange procedure is repeated three times and the sample is identified as NH_4^+-ZSM-5-Soft Template.

Co^{2+} ion exchange is performed to 1 g of NH_4^+-ZSM-5-Soft Template using 150 ml 0.2 M Cobalt-(II) nitrate hexahydrate (Merck, 98%) solution at 353 K for 9 hours under stirring. Then the sample is dried in the oven for one day at 333 K. The ion-exchange procedure is repeated two more times. The zeolite is labeled as Co^{2+}-ZSM-5-Soft Template.

3.1.2 Meso-Na^+,Co^{2+}-ZSM-5 and Meso-Na^+,Ni^{2+}-ZSM-5

ZSM-5 is synthesized using a gel formula of $1SiO_2$:$0.02Al_2O_3$:0.4TPA:$0.08Na_2O$:$1.5H_2O$ reported elsewhere [158]. Firstly, 0.9 g $NaAlO_2$ (Sigma Aldrich, %37–45 Na_2O, %50–56 Al_2O_3) and 0.9 g NaOH are dissolved in 29.4 g de-ionized water under rigorous stirring, followed by the addition of 58.2 g tetrapropylammonium hydroxide (TPAOH, Merck, 40%). Afterwards, 59.1 g tetraethyl orthosilicate (TEOS, Merck, 99.99%) is added dropwise to the mixture under rigorous stirring. All the prepared gels are transferred into Teflon-lined 35 ml autoclaves and heated under static conditions at 443 K for 3 days. Synthesized zeolites are separated using vacuum filtration and washed with 500 ml de-ionized water. Then, zeolite is dried at 333 K, and calcined at 823 K (using a heating rate of 1 K/min) for 20 h in a muffle furnace. NH_4^+ -exchange is applied three times to the dried sample with the procedure indicated for NH_4^+-ZSM-5-Soft Template. The NH_4^+-exchanged sample is labeled as NH_4^+-ZSM-5(I). Desilication is applied based on a reported method in Groen et al. [159]. NH_4^+-ZSM-5(I) is desilicated using 0.2 M NaOH solution in 33 ml de-ionized water at 353 K for 30 min. Then the zeolite is separated using vacuum filtration, washed with deionized water and dried in the oven at 333 K for one day. The prepared zeolite is NH_4^+-exchanged following the same procedure stated before and labeled as NH_4^+-ZSM-5(I)-DES.

Cobalt cation exchange is performed as follows; ion-exchanging three times using 150 ml 0.1 M cobalt (II) nitrate hexahydrate (Merck, 98%) solution at 353 K for 9 h and two times in 75 ml 0.5 M cobalt (II) nitrate hexahydrate (Merck, 98%) solution at room temperature for 24 h. Final product is labeled as Meso-Na^+,Co^{2+}-ZSM-5.

Nickel cation is performed as follows; ion-exchanging three times using 150 ml 0.2 M nickel-(II)-nitrate hexahydrate (Merck, 99%) solution at 353 K for 9 h and one time at 298 K for 24 h. Final sample is labeled as Meso-Na^+,Ni^{2+}-ZSM-5.

3.1.3 Meso-Ni^{2+}-ZSM-5 and Meso-Co^{2+}-ZSM-5

ZSM-5 is synthesized hydrothermally using the gel formula having a molar composition of $1SiO_2$:$0.01Al_2O_3$:$0.112Na_2O$:0.051TPABr:$36H_2O$ reported by Schmith et al. [160]. 18.5 g fumed silica (Sigma Aldrich, %99), 4.2 g tetrapropylammonium bromide (TPABr, Merck, %98), 2.435 g NaOH (Merck, >%99) and 168 g H_2O is stirred at 298 K for 24 h. Afterwards, a mixture of 0.505 g of sodium aluminate ($NaAlO_2$, Sigma Aldrich, %37-45 Na_2O, %50-56 Al_2O_3) and 32 g H_2O de-ionized water is added slowly to the silica containing mixture and stirred at 298 K until a homogeneous solution is obtained. The gel mixtures are then transferred to a Teflon-lined stainless-steel autoclaves and treated hydrothermally at 423 K for 72 h. The solid crystals are separated using vacuum filtration and washed using deionized water until a pH of 7 is obtained. The powder is then dried at 333 K for 24 h and calcined at 823 K for 5 h (using a heating rate of 1 K/min). After calcination, desilication is applied according to the procedure stated in Groen et al [159] that is given in the Meso-Na^+,Co^{2+}-ZSM-5 preparation section in detail. Thereafter NH_4^+ exchange is applied to desilicated 1 g of Na-ZSM-5 samples. The zeolites are exchanged three times using 15 ml 0.5 M NH_4NO_3 (Sigma Aldrich, 99 wt.%) solution at 353 K for 3h. The zeolite is labeled as NH_4^+-ZSM-5(II)-DES. 1 g NH_4^+-ZSM-5(II)-DES is exchanged three times using 100 ml 0.2 M cobalt-(II)-nitrate hexahydrate (Merck, 98%) solution or 100 ml 0.2 M nickel-(II)-nitrate hexahydrate (Merck, 98%)solution at 333 K for 24 h. The exchanged zeolites are labeled as Meso-Co^{2+}-ZSM-5 and Meso-Ni^{2+}-ZSM-5.

3.1.4 Micro-Ni^{2+}-ZSM-5 and Micro-Co^{2+}-ZSM-5

The same procedure in the preparation for Meso-Co^{2+}-ZSM-5 and Meso-Ni^{2+}-ZSM-5 is performed. Chemical amounts and gel formula is similar with a slight difference coming from the doubled aluminum source amount of 1.01 g of $NaAlO_2$. Therefore, the gel formula becomes $1SiO_2$:$0.02Al_2O_3$:$0.125Na_2O$:0.051TPABr:$36H_2O$. After

calcination at 823 K for 5 h (using a heating rate of 1 K/min), 1 g of ZSM-5 isexchanged three times using 150 ml 0.5 M NH_4NO_3 (Sigma Aldrich, 99 wt.%) solution at 353 K for 3h and labeled as NH_4^+-ZSM-5(III). Then the zeolites are exchanged using 100 mL of 0.2 M cobalt-(II)-nitrate hexahydrate (Merck, 98%) or nickel-(II)-nitrate hexahydrate (Merck, 98%) solutions at 333 K for 12 h. The exchange procedure is repeated two more times at 333 K for 24 h. Final zeolites are named as Micro-Co^{2+}-ZSM-5 and Micro-Ni^{2+}-ZSM-5.

3.1.5 Ni^{2+}-US-Y and Co^{2+}-US-Y

NH_4^+-US-Y (Alfa Aesar, Si/Al=6, CAS:1318-02-0.1) zeolites are obtained commercially. 1 g NH_4^+-US-Y (Si/Al=6) is ion-exchanged twice using 75 mL of 0.5 M cobalt(II)-nitrate hexahydrate (Merck, 98%) or nickel-(II)-nitrate hexahydrate (Merck, 98%) aqueous solution at 298 K for 24 h. Cation-exchangedzeolites are labeled as Co^{2+}-US-Y and Ni^{2+}-US-Y.

3.2 Characterization Tests

3.2.1 X-Ray Diffraction (XRD) analysis

X-Ray Diffraction (XRD) analysis of Co^{2+}-ZSM-5-Soft Template, Meso-Na^+,Co^{2+}-ZSM-5, Meso-Na^+,Ni^{2+}-ZSM-5, Ni^{2+}-US-Y and Co^{2+}-US-Y samples are performed with Rigaku Ultima-IV, equipped with Cu Kα radiation (λ=1.5418 Å, 40 kV, 30 mA, Central Laboratory, METU) with a scanning speed of 1º/min.

XRD analysis of Micro-Ni^{2+}-ZSM-5, Micro-Co^{2+}-ZSM-5, Meso-Ni^{2+}-ZSM-5 and, Meso-Co^{2+}-ZSM-5 are performed with Rigaku Miniflex, equipped with Cu Kα radiation (λ = 1.5418 Å, 40 kV,15 mA) with 0.02° step-size and 5°/min scanning rate between 2θ angles of 2° and 50°.

3.2.2 Textural Analysis- N_2 Adsorption Tests

Pore and surface characterization of samples are performed using N_2 adsorption/ desorption isothermsobtained at 77 K using a surface analyzer; i.e., Micromeritics Tristar II 3020 (Chemical Engineering Department, METU). Prior to the adsorption experiment, samples are degassed under vacuum conditions (<150 μmHg) at 573 K for 6 h using Micromeritics VacPrep. Following the filling of the sample container with N_2, the sample is transferred into the surface analyzer. Following room temperature evacuation, the available volume is measured using He gas (Oksan, %99.999). The sample holder temperature is kept at 77 K using liquid N_2 in a dewar. The micropore volume of the samples is calculated based on statistical thickness t-plot analysis, employing the Harkins and Jura equation for the adsorbed layer thickness of 3.5 to 5 Å [161]. The total pore volume of the zeolites are obtained from N_2 adsorption isotherm between 10^{-4} and 0.986 P/P_0 values. The mesopore volume is calculated by subtracting the t-plot micropore volume from the total pore volume. Pore size distributions of samples are obtained using the BJH model from the adsorption branch.

3.2.3 Scanning Electron Microscope (SEM)

The Scanning Electron Microscope (SEM) analysis of samples is conducted with QUANTA 400F Field Emission SEM (Central Laboratory, METU) with an accelerating voltage of 20 kV. The Energy-Dispersive X-ray Spectroscopy (EDX) analysis is also performed using the same accelerating voltage.

3.2.4 Elemental Analysis

The elemental analysis of the samples is performed by inductively coupled plasma optical emission spectrometer (ICP-OES) with Perkin Elmer Optima 4300DV

analyzer (Central Laboratory, METU). The samples are dissolved in HF solution before analysis.

3.3 Diffuse Reflectance (DR) UV–Vis

The diffuse reflectance (DR) UV–Vis experiments are conducted using the spectrometer Shimadzu 2600i equipped with a diffuse reflectance cell (Shimadzu ISR-2600Plus, METU Chemical Engineering Department). A quartz U-tube is filled with a mixture of 0.5 g sample and 2 g Ba_2SO_4. Dehydration is performed by flowing 100 ccm He over the sample at 673 K for 30 min. After the quartz U-tube is sealed, the spectra of samples are taken between 45 000 cm^{-1} and 7 100 cm^{-1}. The absorption intensities are calculated using Schuster–Kubelka–Munk equation $F(R_\infty) = (1 - R_\infty)^2/2R_\infty$ where R_∞ is the diffuse reflectance from a semi-infinite layer and $F(R_\infty)$ is proportional to the absorption coefficient.

3.4 Synchrotron powder X-ray Diffraction

Synchrotron XRD data of powder samples are obtained from MS beamline (ID09) at SESAME light source. The wavelength is 1.03365 (12 keV) with a scanning 2Θ between 2° and 80°[162]. Prior to the analysis, the samples are partially dehydrated under vacuum at 623 K for 4 h using Micromeritics VacPrep. Then, the samples are transferred into a borosilicate capillary (having an OD 1 mm) inside a He filled glovebag. The borosilicate capillary tubes are sealed using epoxy. GSASII software [163] is used to perform the Rietveld Refinement analysis with the Debye-Scherrer diffractometer type. The background, including the peak at 2θ of 5.78°, is fitted by a log interpolate function with 10 parameters. The initial phases are obtained from the International Zeolite Association, Structure Database [123]. Le Bail method is used to fit peak profiles and unit cell parameters. Atomic positions, occupancies, and thermal displacement parameters (U) are refined using Rietveld Refinement. All siliceous Zeolite Y crystallographic information files (cubic unit cell, *Fd-3m* space

group, a= 24.2576 Å) are used for refinement of US-Y. The occupancy of Si and Al atoms were determined based on elemental analysis tests of the samples. Tetrapropylammonium ZSM-5 crystallographic information file (orthorhombic unit cell, *Pnma* space group (orthorhombic space group), a = 20.022 Å, b = 19.899 Å, c = 13.383 Å) is used for refinement of ZSM-5. The framework Si and O atom distances were restrained to 1.61±0.01 Å on ZSM-5 samples using a weight factor of 60. The tetrahedral atom positions in the MFI framework were refined using only Si atoms due to low Al content.

3.5 Hydrogen Storage Experiments (<10 bar)

Hydrogen storage tests up to 10 bar are performed using a homemade volumetric high pressure adsorption system (see Figure 3.1). In the system, high-pressure resistant steel pipes (Swagelok, ¼" O.D., 0.89 mm) and connections are used. The pressures are recorded via an explosion-proof digital pressure manometer (Keller, ECO2-Ei/-1 30bar / 81201.1). Prepared 0.3–0.5 grams zeolites are degassed under vacuum at 653 K for 1 h using a scroll vacuum pump (Agilent Technologies, Model IDP3). Filter (Swagelok Filter, 0002454293) is used above the storage cap to protect the system from the sample and prevent the sample loss during vacuum condition. During H_2 (Hatgaz, 99.999%) storage and available volume (free space) calculation with He (Hatgaz, %99.999), firstly V_1 part of the system is filled with gas and the pressure of this part is denoted as P_1. Then, Valve1 is opened and the equilibrium pressure of the whole system is denoted as P_2. P_3 represents the pressure of the cap that includes sample zeolite. Available volume (free space) of samples is detected with volumetric calculation of He (Hatgaz, %99.999) with respect to Equation 3.1.

$$V_{avaliable\ volume} = \frac{V_1(P_2 - P_1)}{P_3 - P_2} - V_{\text{filter}} \qquad \text{(Eqn.3.1)}$$

$P = \text{Pressure(bar)}$
$n = \text{Adsorbed amount(mol)}$
$R = \text{Gas constant}\left(\frac{\text{bar.ml}}{\text{mol.K}}\right) = 83.14$
$T = \text{Temperature(K)}$

The sample is degassed at 653 K for one hour to desorb He from the sample. After degassing the sample, H_2 (Hatgaz, 99.999%) is dosed to the system with 0.5 bar increments up to 10 bar at 298 K. Almost 15 min is waited to establish equilibrium for each dosing. Adsorbed amount at 298 K is calculated according to Equation 3.2.

$$\frac{P_1V_1}{RT} - \frac{P_2(V_1+V_3)}{RT} + \frac{P_3(V_3+V_{filter})}{RT} = n_{adsorbed} \quad \text{(Eqn.3.2)}$$

Experiments for each sample is carried out at three different temperatures (293–338 K) to calculate the heat of adsorption (Equation.3.3). In the equation, Qst is isosteric heat, P is system pressure and R is the ideal gas constant. For the experiments that are performed at higher temperatures than 298 K, 20 min is needed for equilibrium. The temperature of the V_3 part of the system is brought to the target high temperature value by using the furnace (ORDEL, SC771). The mole balance is established by considering the temperature differences and the amount of hydrogen adsorbed for each pressure is calculated using Equation.3.4.

$$\left(\frac{\partial lnP}{\partial(1/T)}\right)_n = \frac{Q_{st}}{R} \quad \text{(Eqn.3.3)}$$

$$\frac{P_1V_1}{RT_{ambient}} + \frac{P_3V_3}{RT_{high}} + \frac{P_3V_{filter}}{RT_{filter}} - \frac{P_2V_3}{RT_{high}} - \frac{P_2V_1}{RT_{ambient}} - \frac{P_2V_{filter}}{RT_{filter}} = n_{adsorbed} \quad \text{(Eqn.3.4)}$$

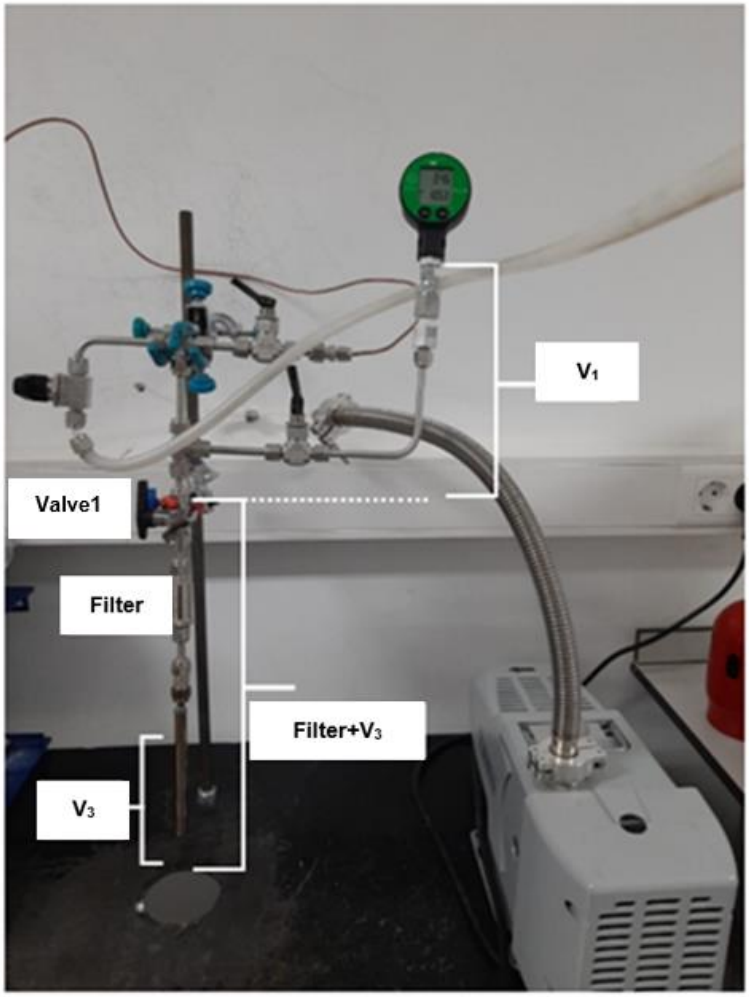

Figure 3.1 Photograph of the H_2 adsorption experiment set-up used for H_2 adsorption up to 10 bar

3.6 High Pressure Hydrogen Storage Experiments (<50 bar)

High pressure experiments are performed using a Micrometric High Pressure Volumetric Analyzer at KUTEM (TÜPRAŞ Energy Center). 0.1–0.2 g zeolite samples are degassed at 623 K for 4 hours. Afterwards hydrogen storage experiments are performed at 298 K up to 50 bar. For each loading 15 min is waited to establish the equilibrium of adsorption and desorption.

3.7 77 K Hydrogen Storage Experiments

Hydrogen storage experiments for 77 K are conducted by Micromeritics Tristar II 3020 (METU, Chemical Engineering Department). 0.2-0.3 g samples are degassed under vacuum condition at 623 K for 4 hours using a degassing instrument (Micromeritics, VacPrep 061). Then, samples are cooled to ambient temperature and filled with nitrogen gas (Oksan, 99.999%). Afterwards zeolites are transferred to Micromeritics Tristar II 3020 for H_2 adsorption analysis, following evacuation for 30 min. The available volume of evacuated samples are measured using He gas (Oksan, 99.999%). Then, hydrogen (Hatgaz, 99.999%) is started to be introduced to the zeolites starting from 0.013 bar up to 1.055 bar incrementally.

3.8 Density Functional Theory Calculations

Density Functional Theory studies are performed by periodic and cluster model. The periodic DFT study is performed by Asst. Prof. Dr Murat Oluş Özbek and cluster model is performed by Dr. Yasemin Kaya on TUBITAK ULAKBIM, High Performance and Grid Computing Center (TRUBA resources).

3.8.1 Cluster Model

Cluster model optimizations are performed using Gaussian09 package with B3LYP functional and 6-31G(d,p) basis set. The cluster structures having α- and γ-sites are cleaved from the optimized ZSM-5 unit cell. After cleaving the cluster, the dangling O atoms are terminated by hydrogen atoms to obtain the neutral charge for the cluster. These H atoms are directed towards the next Si atoms in the unit cell structure. O-H bond lengths are kept fixed at 0.96 Å during all the calculations. Two Si atoms are replaced by two Al atoms. Replacement of each Si atom by an Al atom results in having an extra negative charge on the cluster. Negative charge of the

cluster is saturated by additional Ni^{2+}/Co^{2+} ions. Additionally, 3 possible configurations for Al atoms are tested.

The energy of H_2 adsorption is calculated by Equation 3.5, where $E_{H_2/M^+-zeolite}$ represents the total energy of the adsorbed H_2 on the metal exchanged zeolite, $E_{M^+-zelolite}$ is the energy of the metal exchanged zeolite and $E_{H_2(g)}$ is the energy of a hydrogen molecule in the gas phase.

$$\Delta E_{ads} = E_{H_2/M^+-zelolite} - (E_{H_2(g)} + E_{M^+-zelolite}) \quad \text{(Eqn.3.5)}$$

3.8.2 Periodic Model

Periodic DFT simulations are performed using the Quantum Espresso package [164]. Perdew–Burke–Ernzerhof (PBE) functional is used for the exchange-correlation energy, where the ionic core pseudopotential is expressed using projector augmented wave (PAW) sets. The cut-off energies used for the wavefunctions, and the charge densities are 75 Ry and 476 Ry, respectively. All the results of the Co and Ni containing structures are the outputs of the spin polarized computations and are obtained by relaxing the structures until the net force acting on the ions were Fnet < 0.001 Ry/Bohr and a scf convergence of $1x10^{-6}$ Ry. The Brillouin zone sampling of the ZSM-5 structures and gas phase H_2 molecule are done using a single gamma point, where the periodic molecules of the latter are separated with a minimum of 10 Å vacuum distances in all Cartesian Coordinates. The adsorption energies of the H_2 molecules are calculated as the difference between the DFT energies of the products (H_2 adsorbed structure) and the sum of the reactants (clean structure + H_2(g)) as given in Equation 3.5.

CHAPTER 4

RESULTS AND DISCUSSION

4.1 Characterization Results

4.1.1 XRD Results

XRD patterns of ZSM-5 samples are given in Figures 4.1 and 4.2. All of the ZSM-5 samples show MFI framework characteristic peaks with high crystallinity. Extra peaks and extra phases are not observed for any of the zeolite samples. Na-ZSM-5-Soft Template and Co^{2+}-ZSM-5-Soft Template have lower diffraction intensities and broader peaks compared to other samples due to smaller crystal sizes. As seen in Figures 4.1 and 4.2, there is a slight decrease in peak intensities after desilication due to decreasing crystal sizes (Figure 4.2).

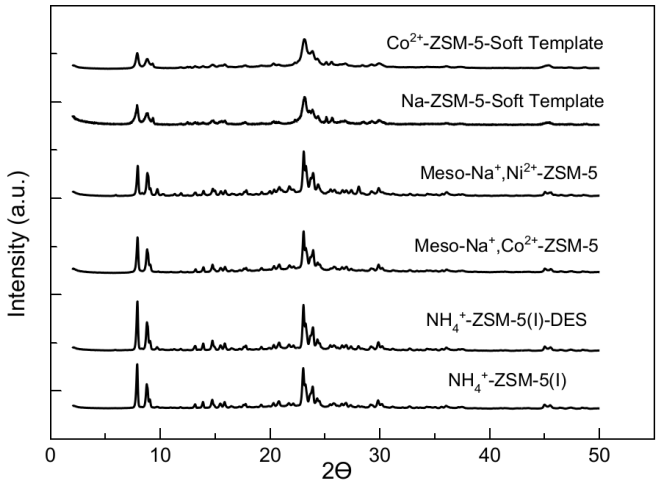

Figure 4.1 XRD patterns of Na-ZSM-5-Soft Template and Co-ZSM-5-Soft Template, Meso-Na^{+},Ni^{2+}-ZSM-5, Meso-Na^{+},Co^{2+}-ZSM-5, NH_4^{+}-ZSM-5(I)-DES, NH_4^{+}-ZSM-5(I)

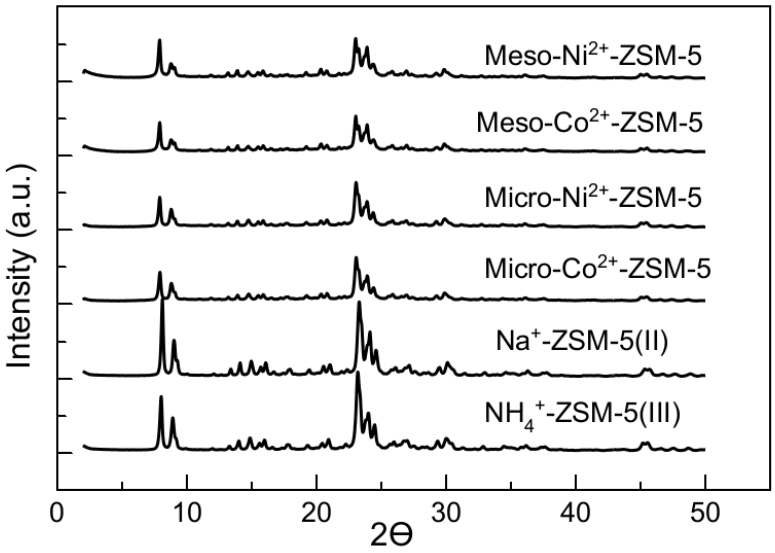

Figure 4.2 XRD patterns of Meso-Ni^{2+}-ZSM-5, Meso-Co^{2+}-ZSM-5, Micro-Ni^{2+}-ZSM-5, Micro-Co^{2+}-ZSM-5, Na-ZSM-5(II) and NH_4^+-ZSM-5(III)

Figure 4.3 shows XRD patterns of US-Y samples. All of the zeolites show well-resolved peaks characteristic for the FAU framework, without the presence of peaks of other crystalline phases or amorphous phase.

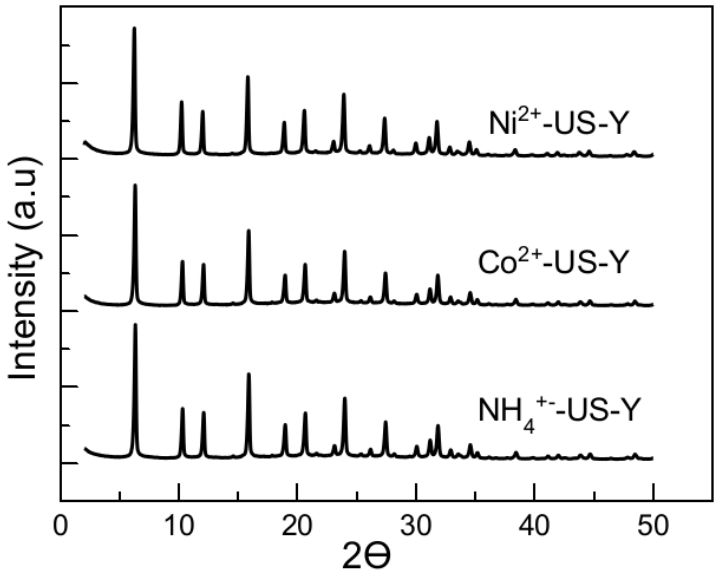

Figure 4.3 XRD patterns of Ni^{2+}-US-Y, Co^{2+}-US-Y, NH_4^+-US-Y

4.1.2 SEM Micrographs

SEM images of Na-ZSM-5-Soft Template and Co^{2+}-ZSM-5-Soft Template are given in Figure 4.4. In the synthesis, ZSM-5 microsphere aggregates are formed from primary nano-particles as can be seen in Figure 4.4(a) and interparticle mesoporosity is obtained with mesoporogen; cetyltrimethylammonium bromide (CTABr).

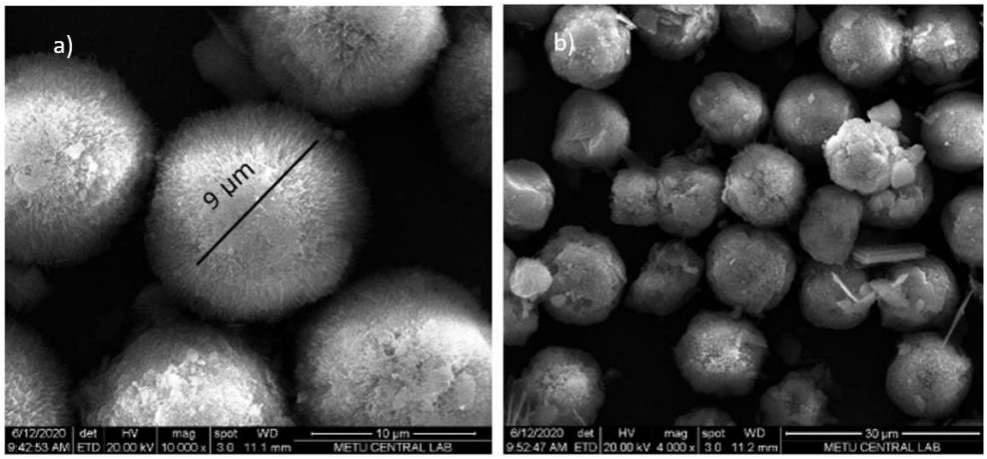

Figure 4.4 SEM micrographs a) Na^{+}-ZSM-5-Soft Template b) Co^{2+}-ZSM-5-Soft Template

Morphologies and the particle sizes of desilication method applied to ZSM-5 are observed in Figures 4.5 and 4.6. Typical ZSM-5 morphology is maintained throughout the alkaline treatment. NH_4^{+}-ZSM-5(I), Meso-Na^{+},Ni^{2+}-ZSM-5 and Meso-Na^{+},Co^{2+}-ZSM-5 samples show characteristic coffin shape of MFI framework with crystal size ranging 1–2 µm. The surface of the samples Micro-Co^{2+}-ZSM-5, Micro-Ni^{2+}-ZSM-5, Meso-Co^{2+}-ZSM-5, and Meso-Ni^{2+}-ZSM-5 are quite rough that can be seen mostly in zeolites with high aluminum content.

US-Y samples show typical FAU crystal morphology (octahedrons and truncated octahedrons) with crystal sizes ranging between 1 and 2 µm as demonstrated in Figure 4.7.

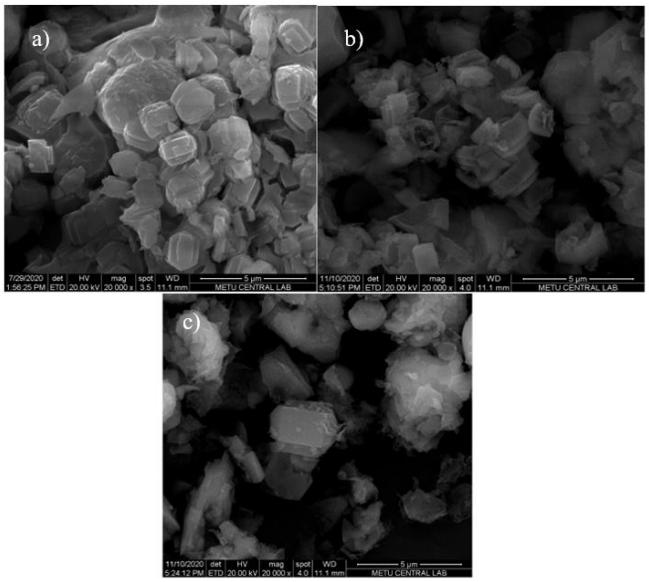

Figure 4.5 SEM micrographs a) NH_4^+-ZSM-5(I) b) Meso-Na^+,Ni^{2+}-ZSM-5 c) Meso-Na^+,Co^{2+}-ZSM-5

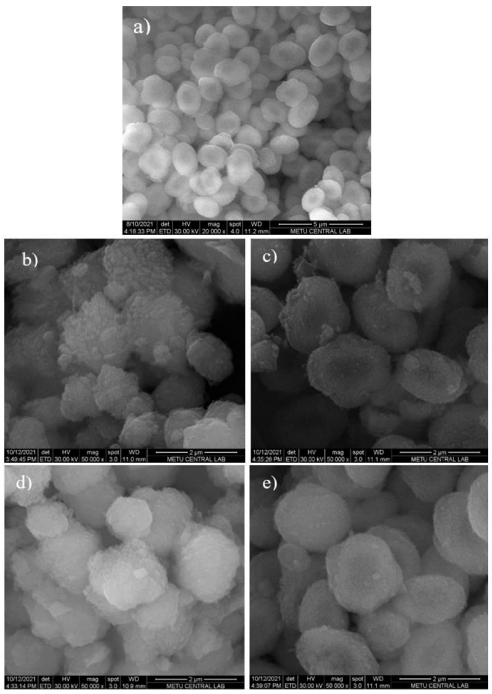

Figure 4.6 SEM micrographs a) Na^+-ZSM-5(II), b) Micro-Co^{2+}-ZSM-5, c) Micro-Ni^{2+}-ZSM-5, d) Meso-Co^{2+}-ZSM-5, e) Meso-Ni^{2+}-ZSM-5

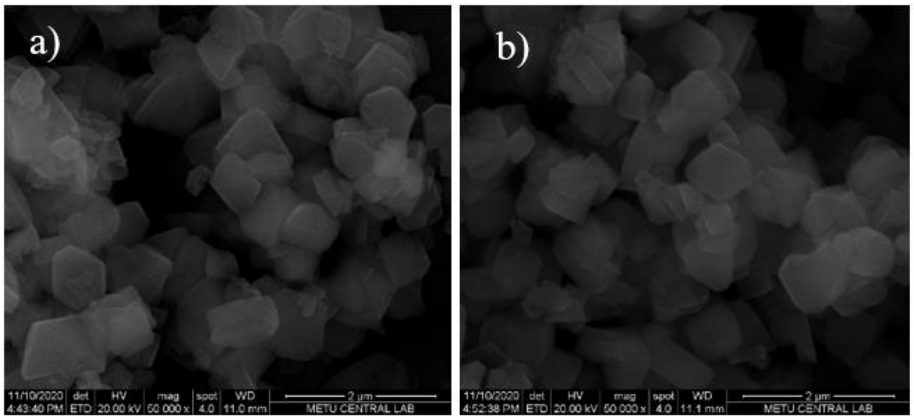

Figure 4.7 SEM micrographs a) Ni^{2+}-US-Y, b) Co^{2+}-US-Y

4.1.3 Elemental Analysis

Si/Al ratio and metal contents are given in Table 4.1. It is aimed to obtain high cation content in order to increase the possible interaction of the zeolites with the hydrogen molecules. The highest metal content in ZSM-5 belongs to Meso-Co^{2+}-ZSM-5 with a value of 0.35 mmol M^{2+}/ g zeolite. According to the ICP results, high aluminum content is observed on Co^{2+}-ZSM-5-Soft Template (Si/Al=11) resulting in 0.23 mmol M^{2+}/g.

As can be seen, the Si/Al ratio of NH_4^+-ZSM-5(I) and Na^+-ZSM-5(II) decreases following the desilication method, which is based on removing Si atoms from the framework. Meso-Ni^{2+}-ZSM-5 and Meso-Co^{2+}-ZSM-5 show a similar Si/Al ratio (~ 22) to Micro-Ni^{2+}-ZSM-5 and Micro-Co^{2+}-ZSM-5 samples with a 0.08 mmol M^{2+}/ $g_{zeolite}$ higher metal content according to ICP results. Meso-Na^+,Co^{2+}-ZSM-5 and Meso-Na^+,Ni^{2+}-ZSM-5 samples also show Na content. Ni^{2+}-US-Y and Co^{2+}-US-Y zeolites show high metal content, due to the low Si/Al ratio (Si/Al = ~5), by 0.35 and 0.42 mmol M^{2+}/g zeolite respectively.

Table 4.1 Elemental analysis of zeolites

Sample	Si/Al[a]	M^{2+}/Al[a]	mmol M^{2+}/g[a]
Na-ZSM-5-Soft Template	12[b]		
Co^{2+}-ZSM-5-Soft Template	11	0.17	0.23
NH_4^+-ZSM-5(I)	32[b]		
Meso-Na^+,Co^{2+}-ZSM-5	14	Co/Al=0.2 Na/Al=0.6	0.24
Meso-Na^+,Ni^{2+}-ZSM-5	12	Ni/Al=0.1 Na/Al=0.2	0.18
Na^+-ZSM-5(II)	33[b]		
Meso-Ni^{2+}-ZSM-5	22	0.44	0.31
Meso-Co^{2+}-ZSM-5	22	0.49	0.35
NH_4^+-ZSM-5(III)	22		
Micro-Ni^{2+}-ZSM-5	21	0.3	0.22
Micro-Co^{2+}-ZSM-5	21	0.36	0.27
NH_4^+-US-Y	6		
Ni^{2+}-US-Y	5	0.13	0.35
Co^{2+}-US-Y	4	0.13	0.42

[a]Elemental analysis performed using ICP-OES

[b]Elemantal analysis performed using EDX

4.1.4 N_2 Adsorption and BJH Pore Volume Distribution Results

N_2 physisorption isotherms of ZSM-5 and US-Y zeolites are given in Figures 4.8, 4.10, and 4.12. BJH Pore Volume Distribution of zeolites are given Figures 4.9, 4.11 and 4.13.

As demonstrated in Figure 4.8, Na-ZSM-5-Soft Template shows type IV isotherm that is commonly observed in porous materials including mesoporosity and H4 hysteresis loop as evidence of mesoporosity in the structure according to IUPAC. Co^{2+}-ZSM-5-Soft Template shows lower N_2 adsorption capacity than Na-ZSM-5-Soft Template due to existing of cations in the structure. Depending on the ionic radii

of extraframework cations they can decrease the available free space for the gas molecules. NH_4^+-ZSM-5(I) sample shows mainly Type I adsorption isotherm, which is seen on microporous materials according to IUPAC. Meso-Na, Ni^{2+}-ZSM-5, and Meso-Na, Co^{2+}-ZSM-5 show exactly Type IV isotherm and adding mesoporosity increases the N_2 adsorption capacity. Therefore, it can be inferred that mesopore addition was successfully applied to NH_4^+-ZSM-5(I) by desilication.

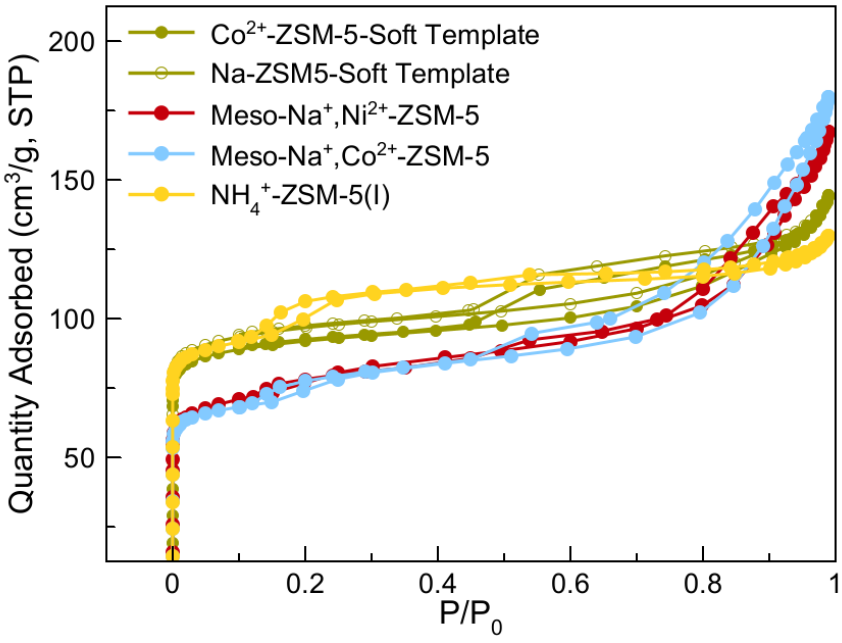

Figure 4.8 N_2 adsorption/desorption isotherms at 77 for Co^{2+}-ZSM-5-Soft Template, Na-ZSM-5-Soft Template, Meso-Na,Ni^{2+}-ZSM-5, Meso-Na,Co^{2+}-ZSM-5, NH_4^+-ZSM-5(I)

Pore sizes of the samples are calculated using Barrett–Joyner–Halenda (BJH) adsorption. Both Na-ZSM-5-Soft Template and Co^{2+}-ZSM-5-Soft Template have pores with 4 nm diameter. NH_4^+-ZSM-5(I) includes pore sizes below < 2 nm showing

a lack of mesopores (2–50 nm). Meso-Na, Ni^{2+}-ZSM-5, and Meso-Na, Co^{2+}-ZSM-5 show pores with sizes around 14 nm due to addition of extra-porosity by desilication.

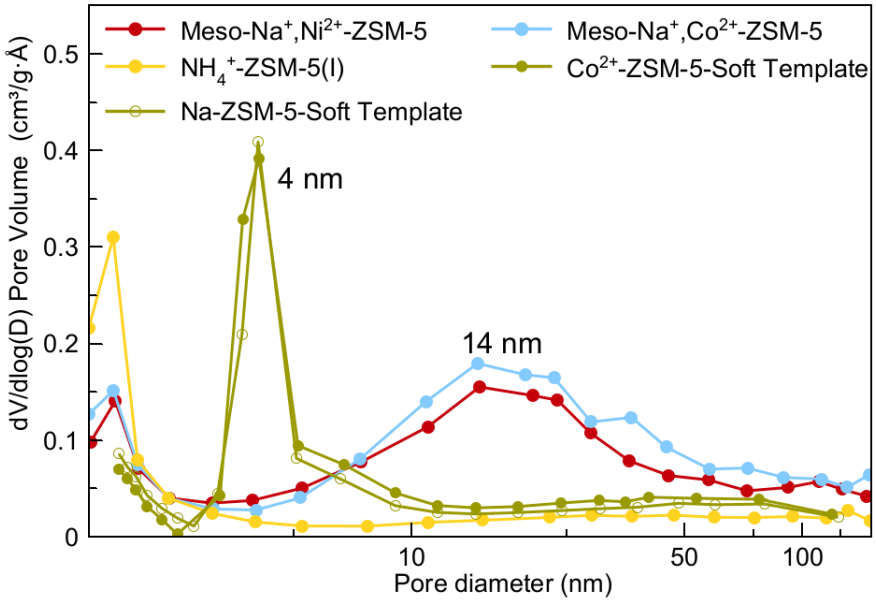

Figure 4.9 BJH adsorption branch pore size distribution of Co^{2+}-ZSM-5-Soft Template, Na-ZSM-5-Soft Template, Meso-Na,Ni^{2+}-ZSM-5, Meso-Na,Co^{2+}-ZSM-5, NH_4^+-ZSM-5(I)

As can be seen in Figure 4.10, Micro-Ni^{2+}-ZSM-5, Micro-Co^{2+}-ZSM-5, Na^+-ZSM-5(III) and NH_4^+-ZSM-5(III) show Type I isotherm. Meso-Ni^{2+}-ZSM-5 and Meso-Co^{2+}-ZSM-5 show Type IV isotherm with higher N_2 adsorption capacity due to the increased total pore volume. Also, cation loading on zeolites do not affect the pore characteristics according to the similarity on isotherms of NH_4^+-ZSM-5(III), Micro-Ni^{2+}-ZSM-5 and Micro-Co^{2+}-ZSM-5.

According to shown BJH adsorption branches in Figure 4.11, Micro-Ni^{2+}-ZSM-5, Micro-Co^{2+}-ZSM-5, Na^+-ZSM-5(II) and NH_4^+-ZSM-5(III) include micropores < 2 nm, while Meso-Ni^{2+}-ZSM-5 and Meso-Co^{2+}-ZSM-5 pore sizes are in the broad range between 4 and 92 nm with maximum pore volume at 14 nm.

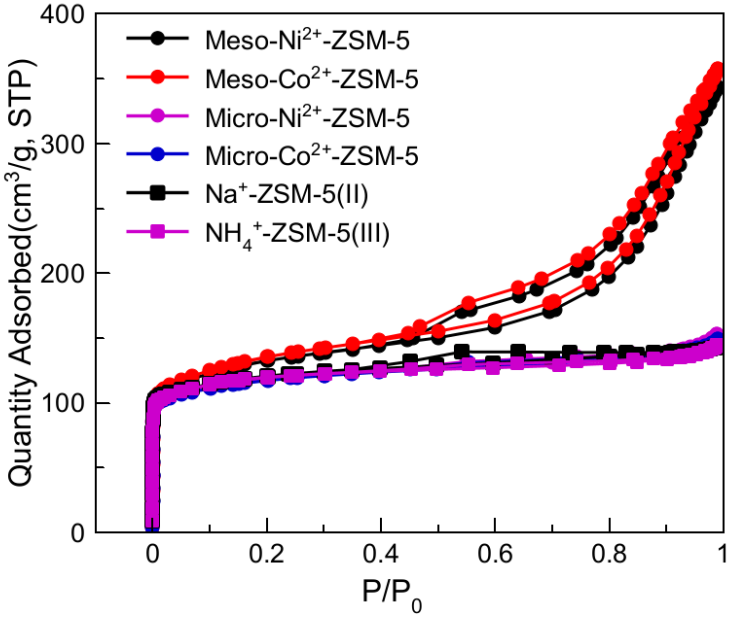

Figure 4.10 N_2 adsorption/desorption isotherms at 77 for Meso-Ni^{2+}-ZSM-5, Meso-Co^{2+}-ZSM-5, Micro-Ni^{2+}-ZSM-5, Micro-Co^{2+}-ZSM-5, Na^{+}-ZSM-5(III), NH_4^{+}-ZSM-5(III)

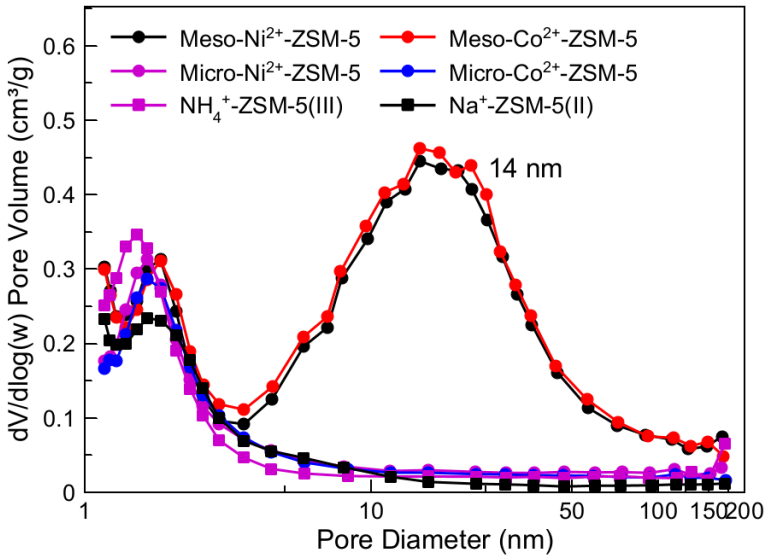

Figure 4.11 BJH adsorption branch pore size distribution of Meso-Ni^{2+}-ZSM-5, Meso-Co^{2+}-ZSM-5, Micro-Ni^{2+}-ZSM-5, Micro-Co^{2+}-ZSM-5, Na^{+}-ZSM-5(II), NH_4^{+}-ZSM-5(III)

Ni^{2+}-US-Y, Co^{2+}-US-Y and NH_4^{+}-US-Y show Type IV type of isotherm and H4 hysteresis type similar with mesopore added ZSM-5 samples. Pore sizes of US-Y

samples change between 3 and 90 nm and peak at 24 nm as shown BJH pore volume distribution in Figure 4.13.

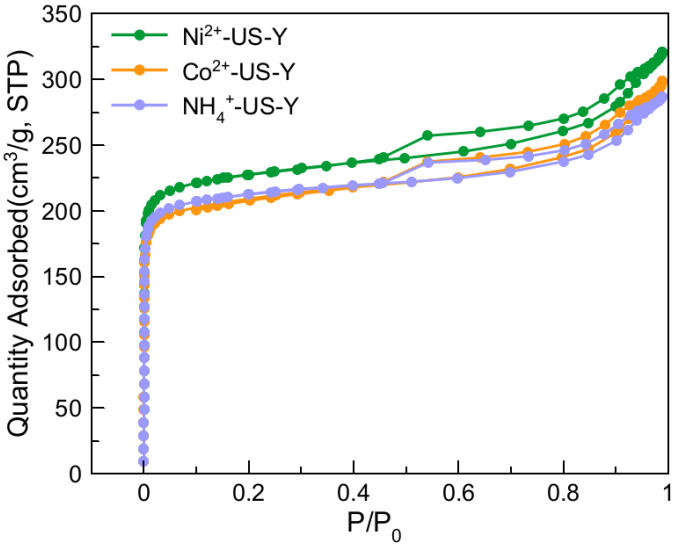

Figure 4.12 N_2 adsorption/desorption isotherms at 77 for Ni^{2+}-US-Y, Co^{2+}-US-Y, NH_4^+-US-Y

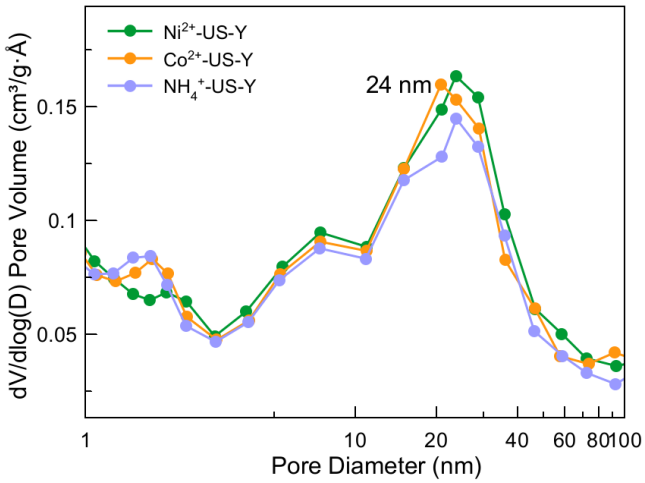

Figure 4.13 BJH adsorption branch pore size distribution of Ni^{2+}-US-Y, Co^{2+}-US-Y, NH_4^+-US-Y

Surface area and pore volumes of zeolites are calculated using the N_2 physisorption isotherms and the results are listed in Table 4.2. Mesopore volume of zeolites is

calculated by substracting micropore volume (V_{micro} (cm^3/g)) from total pore volume (V_{total} (cm^3/g)).

Synthesized microporous ZSM-5 show pore volumes (0.13–0.14 cm^3/g) that are in agreement with the characteristic MFI framework micropore volume (0.13–0.15 cm^3/g) [165]. Na-ZSM-5-Soft Template and Co^{2+}-ZSM-5-Soft Template show the total pore volume as 0.22 cm^3/g with a mesopore volume around 0.1 cm^3/g.

After alkaline treatment, the total pore volume of NH_4^+-ZSM-5(I) is successfully increased from 0.15 cm^3/g to 0.28 and 0.25 cm^3/g with the addition of ~ 0.14 cm^3/g mesopore volume as can be seen on the samples Meso-Na^+,Co^{2+}-ZSM-5 and Meso-Na^+,Ni^{2+}-ZSM-5.

Na^+-ZSM-5(II) has a total 0.22 cm^3/g pore volume and is increased to 0.52 and 0.54 cm^3/g after alkaline treatment as can be seen on Meso-Ni^{2+}-ZSM-5 and Meso-Co^{2+}-ZSM-5 respectively. The micropore volumes of Na^+-ZSM-5(II), Meso-Ni^{2+}-ZSM-5 and Meso-Co^{2+}-ZSM-5 are similar. Hence, it can be inferred that desilication has insignificant destructive effect on the texture of the samples. Moreover, Langmuir surface area is expanded from 354 m^2/g to ~ 600 m^2/g after desilication on Na^+-ZSM-5(II) due to the addition of mesopores.

Microporous zeolites NH_4^+-ZSM-5(III), Micro-Ni^{2+}-ZSM-5, and Micro-Co^{2+}-ZSM-5 show total pore volume as ~ 0.23 cm^3/g with 0.1 cm^3/g mesopore volume. There is a slight decrease in the total micropore volume due to presence of nickel or cobalt cations.

US-Y zeolites show a total pore volume of 0.49 cm^3/g with an addition of 0.20 cm^3/g mesopore volume to 0.29 cm^3/g micropore volume. In this study, US-Y zeolites show a higher Langmuir surface area (~ 1000 m^2/g) than ZSM-5 zeolites showing a maximum 614 m^2/g surface area with the Meso-Co^{2+}-ZSM-5 sample.

Table 4.2 N_2 physisorption characteristic results for zeolites

Sample	$S_{Langmuir}$ (m^2/g)	V_{total} (cm^3/g)	V_{micro} (cm^3/g)	V_{meso} (cm^3/g)
Na-ZSM-5-Soft Template	429	0.22	0.12	0.1
Co^{2+}-ZSM-5-Soft Template	407	0.22	0.15	0.07
NH_4^+-ZSM-5(I)	357	0.15	0.11	0.04
Meso-Na^+,Co^{2+}-ZSM-5	343	0.28	0.1	0.18
Meso-Na^+,Ni^{2+}-ZSM-5	354	0.25	0.09	0.16
Na^+-ZSM-5(II)	535	0.22	0.13	0.09
Meso-Ni^{2+}-ZSM-5	600	0.52	0.12	0.41
Meso-Co^{2+}-ZSM-5	614	0.54	0.11	0.43
NH_4^+-ZSM-5(III)	531	0.22	0.14	0.08
Micro-Ni^{2+}-ZSM-5	527	0.23	0.13	0.1
Micro-Co^{2+}-ZSM-5	523	0.23	0.13	0.1
NH_4^+-US-Y	946	0.46	0.27	0.19
Ni^{2+}-US-Y	1007	0.49	0.29	0.2
Co^{2+}-US-Y	968	0.46	0.28	0.18

4.2 Hydrogen Adsorption (~298 K, < 10 bar) Results

Hydrogen gravimetric uptake isotherms of zeolites are given in Figures 4.14, 4.15 and 4.16 separately. Ni^{2+}-, Co^{2+}- zeolites show higher uptake capacity (0.06–0.14 wt.%, 10 bar) than NH_4^+- zeolites (0.05–0.06 wt.%, 10 bar) [166]. The highest gravimetric capacity belongs to Meso-Ni^{2+}-ZSM-5 with 0.14 wt.% and the order of the capacities continues as Meso-Na,Ni^{2+}-ZSM-5, Micro-Ni^{2+}-ZSM-5, Ni^{2+}-US-Y, Meso-Co^{2+}-ZSM-5 (all shows ~ 0.1wt.%) > Co^{2+}-ZSM-5-Soft Template, Micro-Co^{2+}-ZSM-5, Co^{2+}-US-Y (all shows 0.08 wt.%) > Meso-Na,Co^{2+}-ZSM-5 (0.05 wt.%). Overall, Ni^{2+}-zeolites show a higher capacity than the Co^{2+} loaded form of the same NH_4^+- zeolite. The main reason for this result can be higher attraction of Ni^{2+} cation with hydrogen at 298 K.

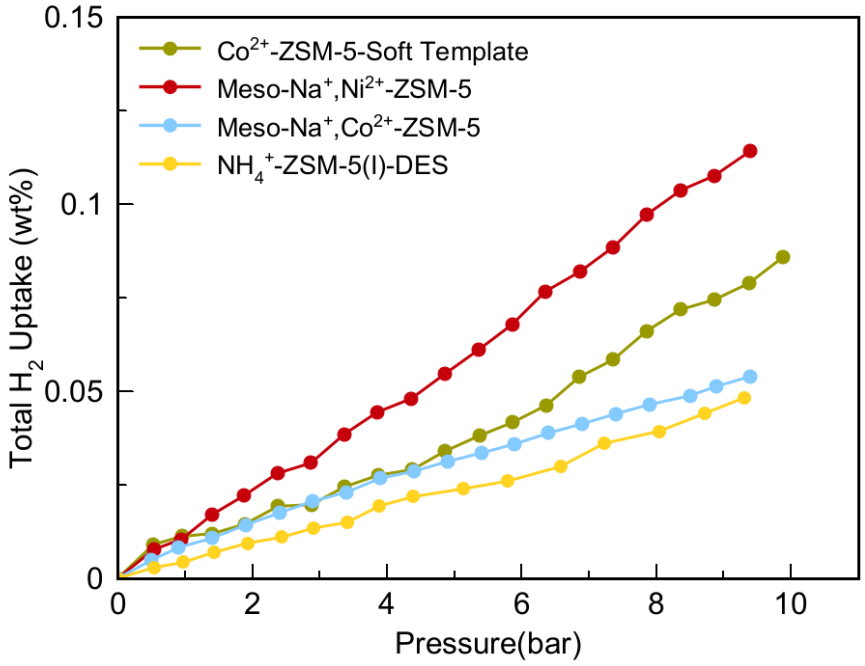

Figure 4.14 Gravimetric uptake isotherms of Co^{2+}-ZSM-5-Soft Template, Meso-Na,Ni^{2+}-ZSM-5, Meso-Na,Co^{2+}-ZSM-5, NH_4^+-ZSM-5(I)-DES up to 10 bar

The 10 bar result of Meso-Ni^{2+}-ZSM-5 (0.14 wt.%) is higher than the reported 0.1 wt.% capacity of Na-A zeolite under ambient temperature and 10 bar [90]. Besides, Meso-Ni^{2+}-ZSM-5 has a similar capacity with Ni^{2+} cation loaded metal organic framework (Ni_2(m-dobdc)) showing value of ca. 0.13% at 298 K and 10 bar [69]. On the other hand, NiNaX shows 0.16 wt.% at 303 K and 5 bar which is higher than the results of this study. One possible reason is the high metal content of NiNaX with 2.2 mmol Ni^{2+}/g [167].

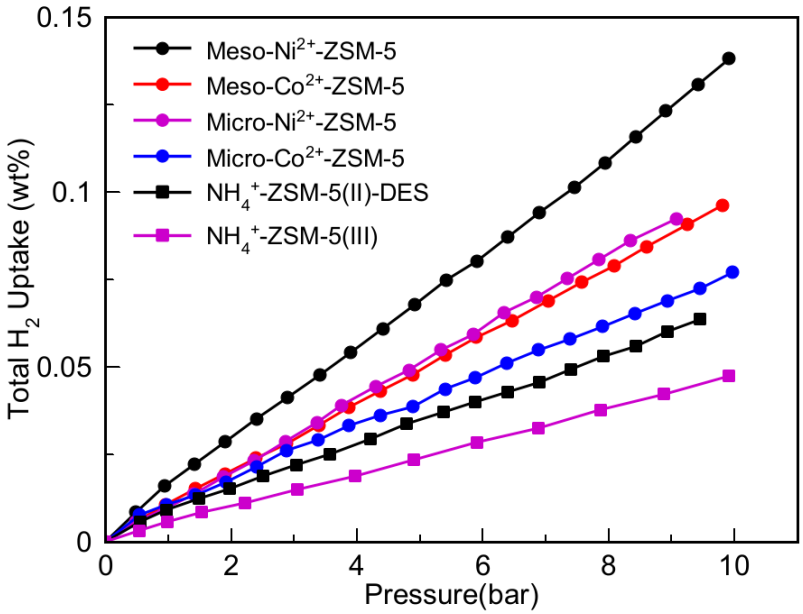

Figure 4.15 Gravimetric uptake isotherms of Meso-Ni^{2+}-ZSM-5, Meso-Co^{2+}-ZSM-5, Micro-Ni^{2+}-ZSM-5, Micro-Co^{2+}-ZSM-5, NH_4^+-ZSM-5(II), NH_4^+-ZSM-5(III)

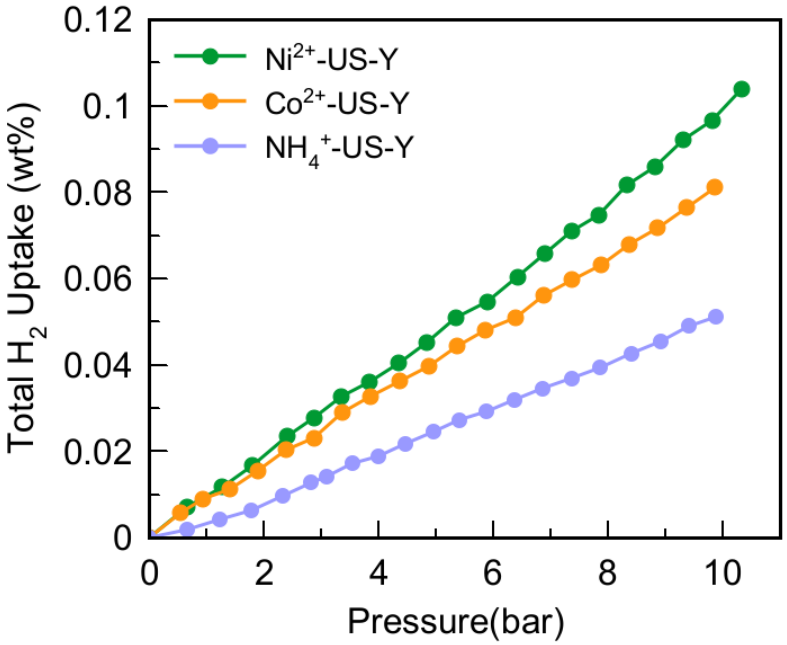

Figure 4.16 Gravimetric uptake isotherms of Ni^{2+}-US-Y, Co^{2+}-US-Y, NH_4^+-US-Y

The volumetric storage capacity of zeolites is calculated by dividing the gravimetric capacity by the total pore volume and the results are demonstrated in Figure 4.17.

The highest volumetric capacity belongs to Meso-Na,Ni^{2+}-ZSM-5 (4.5 g H_2/L) and followed by Micro-Ni^{2+}-ZSM-5 (4 g H_2/L) > Co^{2+}-ZSM-5-Soft Template (3.9 g H_2/L) > Micro-Co^{2+}-ZSM-5 (3.35 g H_2/L) > Meso-Ni^{2+}-ZSM-5 (2.7 g H_2/L)> Meso-Na,Co^{2+}-ZSM-5~Ni^{2+}-US-Y~Co^{2+}-US-Y~Meso-Co^{2+}-ZSM-5 (all shows ~2g H_2/L).

As mentioned before the highest volumetric capacity among the MOFs is reported for Ni_2(m-dobdc) showing 11 g/L at 298 K and 100 bar [69]. All of the zeolites in this study show higher volumetric capacity than the calculated 10 bar result (1.52 g/L) of Ni_2(m-dobdc). The lower total pore volume of the zeolites provides them higher volumetric capacity and makes them promising porous materials for hydrogen storage.

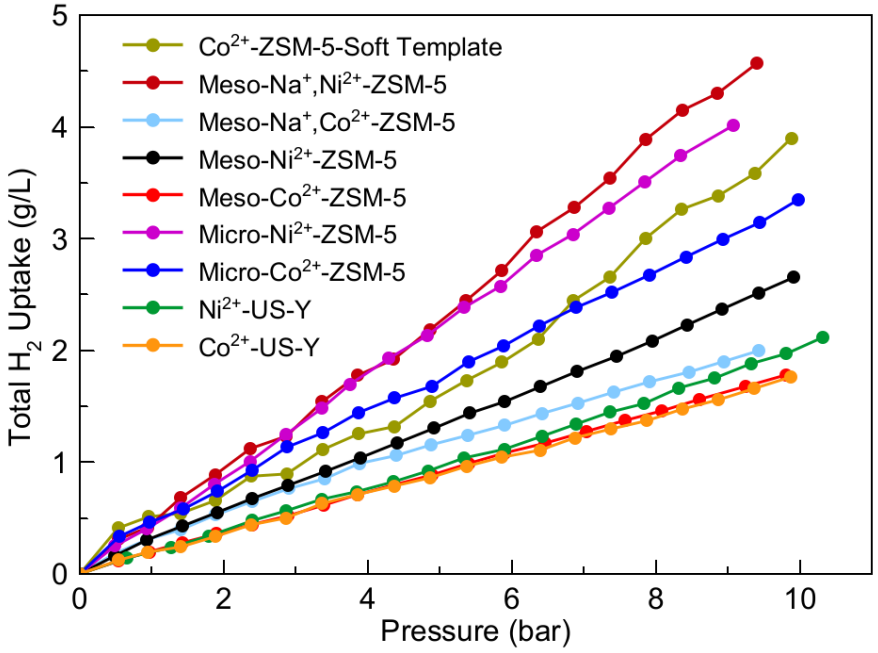

Figure 4.17 Volumetric capacity of Ni^{2+} , Co^{2+}-zeolites up to 10 bar

The prevalent parameter is the heat of adsorption at ambient temperature and low pressure storage [38]. Therefore, the main reason for observing high uptake capacity on Ni^{2+} - zeolites than Co^{2+}-zeolites is higher isosteric heat values. Hydrogen molecules are firstly adsorbed on the strongest cation sites on the framework, and it is suggested that the 2 H_2/M^{2+} is the upper limit to observe the initial heat of adsorption effect on the hydrogen physisorption. H_2/M^{2+} trends (<10 bar) of the

zeolites are given in Figure 4.18 (see Appendix A for the sample calculation for Ni^{2+}-US-Y and Table A.1 for the calculated results of H_2/Ni^{2+}). H_2/M^{2+} ratios are calculated using mmol M^{2+}/g zeolite found according to ICP-OES (Table 4.1). Prior to the hydrogen storage experiment, the samples are degassed at 673 K under vacuum. The oxidation state of the zeolites is expected to be 2+ since, the oxidation states of Ni^{2+} and Co^{2+} cations are expected to be 2+ during degassing up to 723 K under vacuum conditions [156][168][154].

Although Ni^{2+}, Co^{2+}- US-Y zeolites have high metal content (0.35 mmol and 0.42 M^{2+}/g zeolite) than ZSM-5 samples, they show lower H_2/M^{2+} because of the inaccessible sites on the FAU framework. In this study, pore volume restriction of ZSM-5 is targeted to be overcome by adding mesoporosity. However, the mesopore effect is not observed up to 10 bar. The evidence comes from the H_2/M^{2+} trend similarity on Meso-Ni^{2+}-ZSM-5 and Micro-Ni^{2+}-ZSM-5 as well as on Meso-Co^{2+}-ZSM-5 and Micro-Co^{2+}-ZSM-5. This situation claims that the heat of adsorption is still the dominant parameter up to 10 bar and hydrogen molecules have not yet begun to fill the pores.

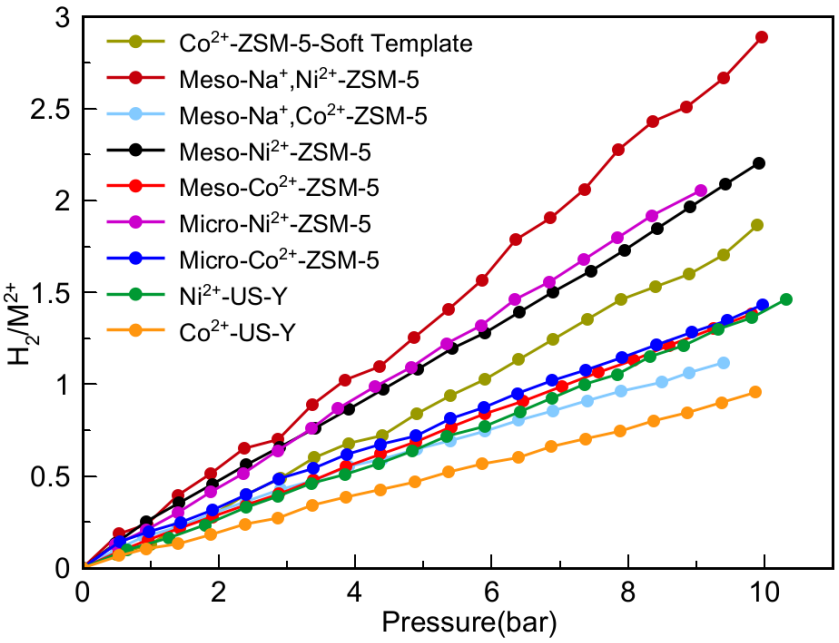

Figure 4.18 H_2/M^{2+} trends of Ni^{2+} , Co^{2+}-zeolites up to 10 bar

At the same pressure, zeolites having higher H_2/M^{2+} are predicted to have strong interaction with hydrogen, which results in a higher isosteric heat value. Isosteric heat trends ($-Q_{st}$) of the zeolites are given in Figures 4.19 and 4.20. $-Q_{st}$ and H_2/M^{2+} trends of the zeolites are in the same line indicating the dominance of the heat of adsorption up to 10 bar.

Isosteric heats of zeolites ($-Q_{st}$) are calculated by using three different adsorption isotherms obtained in the 293–338 K temperature range (isotherms can be found in Appendix Figure B1, data used to obtain isosteric heat and Van't Hoff plots of Micro-Ni^{2+}-ZSM-5 is given in Appendix Table B2 and Figure B2 respectively). NH_4^+- zeolites show similar initial isosteric heats in the range of $-Q_{st}$=8.5–10 kJ/mol (Figure 4.19). Ni^{2+}, Co^{2+}-zeolites show higher initial heat of adsorption values in the range of $-Q_{st}$=15–40 kJ/mol (Figure 4.20). Ni^{2+} and Co^{2+} sites on zeolites show a strong affinity with hydrogen resulting in the high heat of adsorption values. The highest H_2/M^{2+} values belongs to Meso-Na,Ni^{2+}-ZSM-5 which shows also the highest $-Q_{st}$ value with 40 kJ/mol and is followed by Meso-Ni^{2+}-ZSM-5~Ni^{2+}-ZSM-5>Ni^{2+}-US-Y~Meso-Co^{2+}-ZSM-5~Co^{2+}-ZSM-5> Co^{2+}-US-Y> Meso-Na,Co^{2+}-ZSM-5. Heat of adsorption values of all zeolites decrease slightly as hydrogen uptake increases. The main reason is the existence of different cation sites on the framework and these sites can also show different affinities with hydrogen. As H_2 binding energies depend on the specific cation sites, it is essential to investigate these energies specific to possible Ni^{2+}-, Co^{2+}- cation locations for ZSM-5 and US-Y. Such an investigation is given in Sections 4.4.1 (Diffuse Reflectance UV–Vis Results), 4.4.2 (Synchrotron Powder XRD (SXRD) Results) and 4.4.3 (Density Functional Theory (DFT)).

As can be seen in Figure 4.19, isosteric heat trends of Meso-Na,Ni^{2+}-ZSM-5 and Meso-Na^+,Co^{2+}-ZSM-5 decrease more sharply compared to other Ni^{2+}, Co^{2+}-zeolites. The possible reason is the presence of Na^+ cations showing $-\Delta H$ = 6–10 kJ/mol experimentally [102,105].

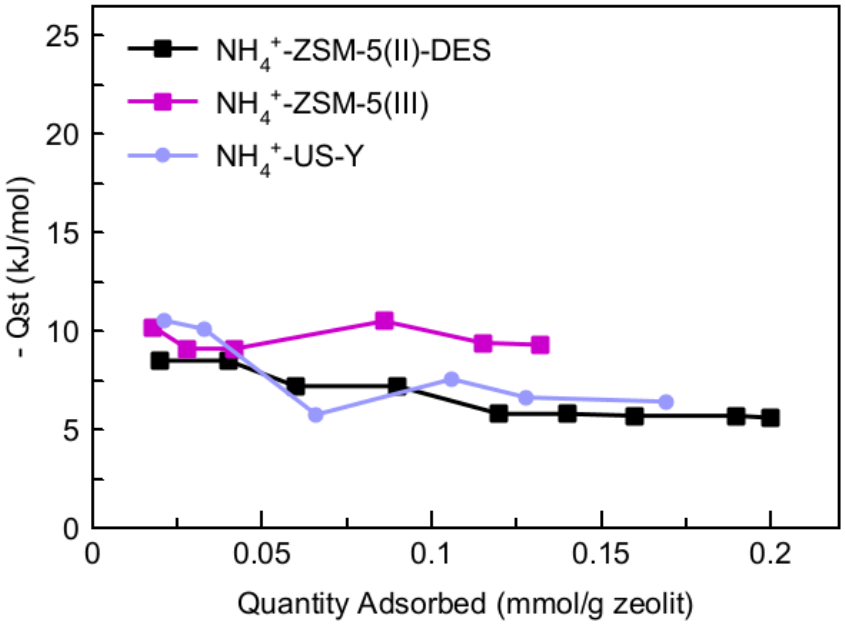

Figure 4.19 Isosteric heats (-Qst) results calculated for NH_4^+-zeolites at 293–338 K

In order to obtain reversible hydrogen physisorption, the heat of adsorption should be in the range of $-\Delta H^0_{opt} = 15 - 25$ kJ/mol [39,40]. In Bhatia and Myers's study, the optimum heat of adsorption is calculated as -15.1 kJ/mol ($\Delta S° = -8R$ for a variety of adsorbents) for 298 K and 1.5–30 bar cycling adsorption process [38]. However, the entropy of adsorption is found as -140 J/mol/K for the zeolites showing high heat of adsorption ($\Delta H^0 = -18 \frac{kJ}{mol}$)[169]. If the optimum heat of adsorption is recalculated for the working pressure range of 5–100 bar and $\Delta S^0 = -140 \frac{J}{mol\ K}$, it can be found as 34 kJ/mol. Consequently, isosteric heat results of Ni^{2+}, Co^{2+}- zeolites ($-\Delta H^0$=15–40 kJ/mol) in this study can be appropriate candidates for hydrogen storage between 100 bar and 5 bar. In addition, Ni^{2+}, Co^{2+}- zeolites in this study show higher heat of adsorption values than Ni^{2+}-MOF and Co^{2+}-MOFs showing heat of adsorption values between -13.5 and -10.7 kJ/mol [70–72,170,171]. Although high Van der Waals interaction between H_2 and extraframework cation sites is crucial, the pore size should be also less than 1 nm in order to have high affinity. At this point, zeolites ZSM-5 (5.4 x 5.6 Å) and US-Y (14.1 x 15.6 Å) have an advantage with their cage sizes especially for the high pressure levels when compared to MOFs.

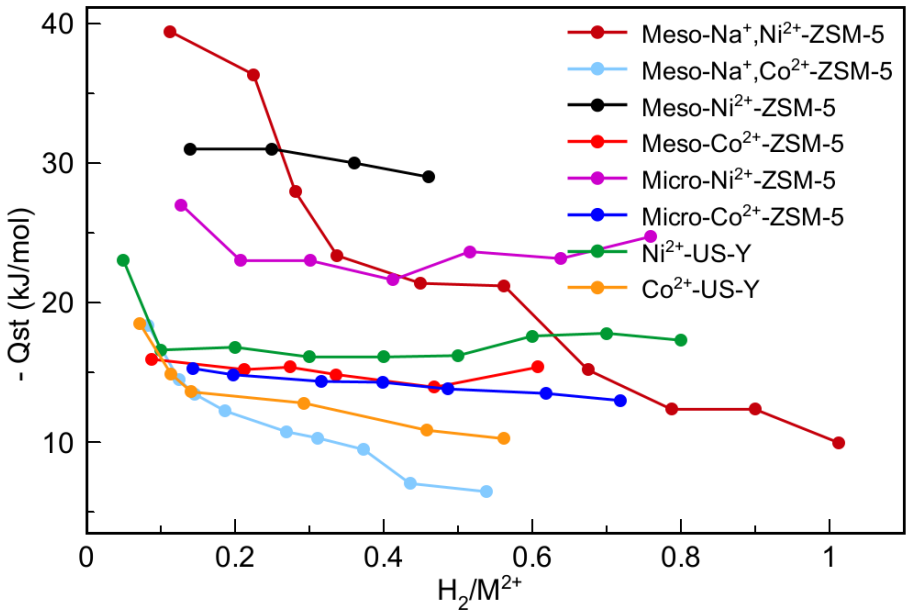

Figure 4.20 Isosteric heats (-Qst) results calculated for Co^{2+}- and Ni^{2+}- zeolites at 293–338 K

4.3 Hydrogen Adsorption (298 K, < 50 bar) Results

A couple of Ni^{2+}, Co^{2+}-zeolites are analyzed up to 50 bar at 298 K in order to observe high pressure performances. The gravimetric capacity results are given in Figure 4.21. The highest gravimetric capacity is reached on Ni^{2+}-US-Y with 0.55 wt.% capacity and followed by Meso-Na,Ni^{2+}-ZSM-5 (0.5 wt.%), Co^{2+}-US-Y (0.46 wt.%), Meso-Na,Co^{2+}-ZSM-5(0.35 wt.%) and Co^{2+}-ZSM-5-Soft Template (0.3 wt.%). In terms of the gravimetric capacity values, Co^{2+}- and Ni^{2+}-exchanged zeolites show similar uptake performances (0.3–0.6 wt.% at 298 K and 50 bar) when compared to Ni_2(m-dobdc) and Co_2(m-dobdc) [69]. One recent study belongs to Villajos et al., which is performing hydrogen uptake on Ni- or Co-MOF-74 (-Qst=~12 kJ/mole) under ambient temperature up to 50 bar. In the study, the highest total gravimetric capacity belongs to Ni-MOF-74 with 0.47 wt.% at 298 K and 50 bar [172]. The gravimetric uptake of Ni^{2+}-USY (0.55 wt.%) surpasses the Ni-MOF-74 under the same conditions due to high affinity with hydrogen resulting higher heat of adsorption value (-Qst=~17 kJ/mole).

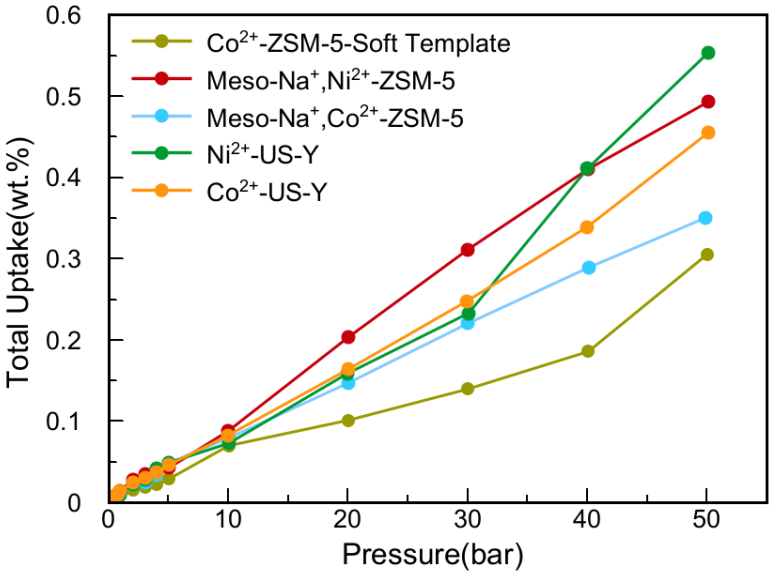

Figure 4.21 Gravimetric capacity of Co^{2+}-ZSM-5-Soft Template, Meso-Na,Ni^{2+}-ZSM-5, Meso-Na,Co^{2+}-ZSM-5, Ni^{2+}-US-Y,Co^{2+}-US-Y for 298 K and 50 bar

Figure 4.22 and 4.23 show H_2/M^{2+} and volumetric capacity results of the zeolites respectively. It is previously concluded that the heat of adsorption is still the dominant parameter up to 10 bar from the experimental results in this study. H_2/M^{2+} results of the zeolites increase to the range 5–14 H_2/M^{2+} at 50 bar as given in Figure 4.22. High H_2/M^{2+} values show that the hydrogen is adsorbed also on the zeolite's walls in addition to extraframework cation sites. Although US-Y zeolites have a higher surface area and pore volume than the ZSM-5 zeolites, they show lower volumetric capacity. The possible reason is a high hydrogen affinity of ZSM-5 due to a smaller cage size than US-Y resulting high affinity of hydrogen to zeolite walls. This situation is confirmed by the H_2/M^{2+} results of the zeolites in Figure 4.22. Meso-Na,Ni^{2+}-ZSM-5 and Meso-Na,Co^{2+}-ZSM-5, show higher H_2/M^{2+} than Ni^{2+}-US-Y and Co^{2+}-US-Y at 50 bar.

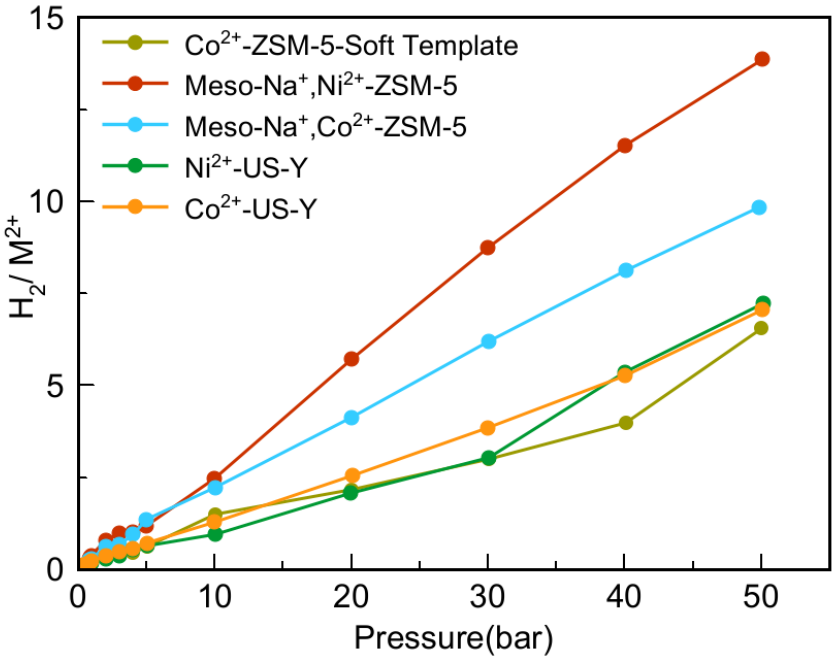

Figure 4.22 H_2/M^{2+} results for Co^{2+}-ZSM-5-Soft Template, Meso-Na,Ni^{2+}-ZSM-5, Meso-Na,Co^{2+}-ZSM-5, Ni^{2+}-US-Y,Co^{2+}-US-Y at 298 K and up to 50 bar

The highest volumetric capacity belongs to Meso-Na,Ni^{2+}-ZSM-5 (20 g H_2/L) and is followed by Co^{2+}-ZSM-5-Soft Template~Meso-Na,Co^{2+}-ZSM-5(14 g H_2/L)>Ni^{2+}-US-Y(11g H_2/L)>Co^{2+}-US-Y(10 g H_2/L). As mentioned before volumetric storage capacity is quite more crucial than gravimetric capacity because of its direct relation to the volume of the storage tank. The reached ultimate volumetric storage capacity (20 g H_2/L) in this study surpasses the results of the reported highest volumetric capacity (Ni_2(m-dobdc, 11 g H_2/L) among the MOFs at 298 K and 100 bar [69]. Similarly, Meso-Na,Co^{2+}-ZSM-5 shows higher capacity than Co_2(m-dobdc) having ca. 7.1 g/L at 298 K and 50 bar [69]. ZSM-5 zeolites have an advantage with their narrow pore openings (<1nm) and low total pore volume (0.25–0.28 cm^3/g) compared to Ni_2(m-dobdc) and Co_2(m-dobdc) having ~0.53 cm^3/g pore volume. Therefore, 20 g H_2/L volumetric capacity reached at 298 K and 50 bar show great potential to achieve the target volumetric adsorption capacity of 40 g H_2/L at 100 bar set by the Department of Energy [19]. On the other hand, it is

expected to observe high storage capacity on Ni^{2+}-US-Y and Co^{2+}-US-Y zeolites at higher pressures (~ 100 bar) because of their high surface area and total pore volume.

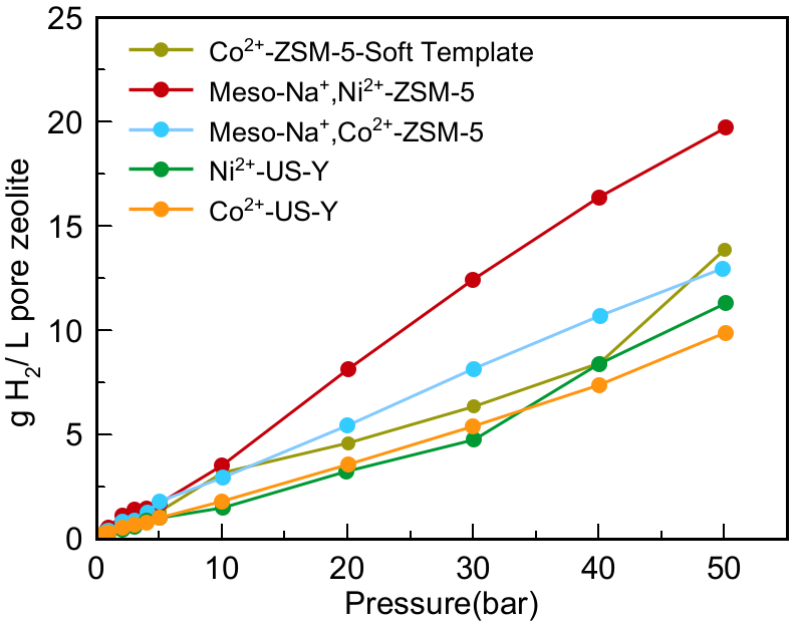

Figure 4.23 Volumetric capacity of Co^{2+}-ZSM-5-Soft Template, Meso-Na,Ni^{2+}-ZSM-5, Meso-Na,Co^{2+}-ZSM-5, Ni^{2+}-US-Y,Co^{2+}-US-Y for 298 K and up to 50 bar

One important parameter to determine appropriate porous material for hydrogen storage is reversibility at ambient condition. Ni^{2+},Co^{2+}-zeolites in this study show reversibility except Ni^{2+}-US-Y as shown in Figure 4.24.

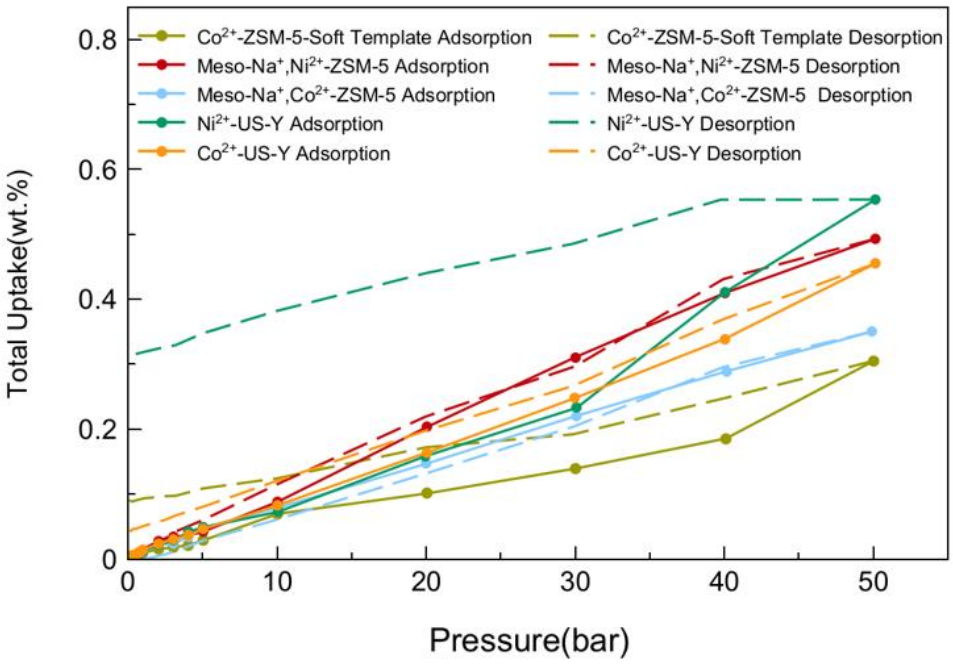

Figure 4.24 Adsorption/Desorption branch of Ni^{2+},Co^{2+}-zeolites at 298 K up to 50 bar

Figures 4.25 and 4.26 show 10 bar and 50 bar volumetric storage results of Ni^{2+}-, Co^{2+}-ZSM-5 zeolites. Although two different hydrogen storage experiments are performed under different laboratory environments, they show similar results for Meso-Na,Ni^{2+}-ZSM-5 and Meso-Na,Co^{2+}-ZSM-5. This situation can be evidence of the reproducibility of hydrogen storage on these zeolites. Micro-Ni^{2+}-ZSM-5 and Micro-Co^{2+}-ZSM-5 zeolites can also show high volumetric capacity at higher pressures under ambient conditions.

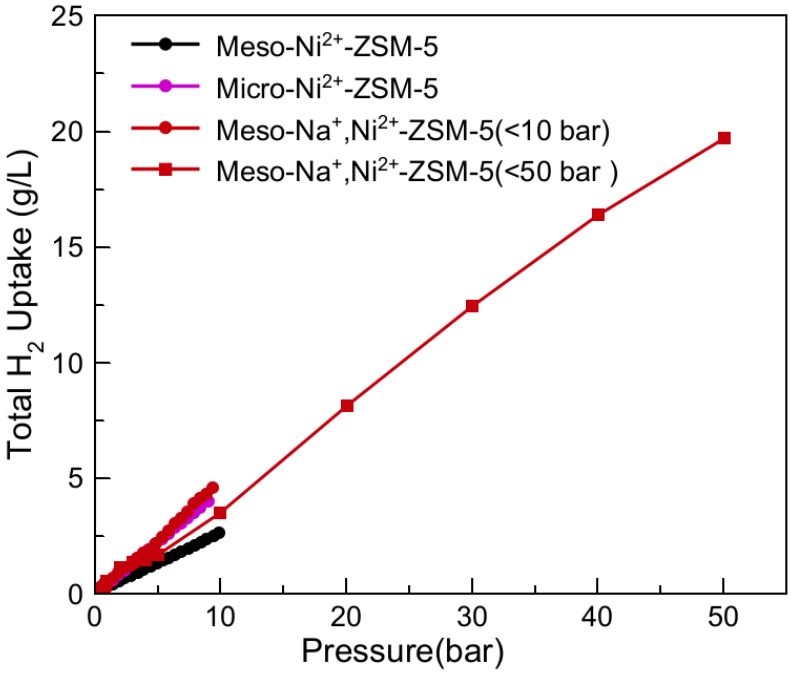

Figure 4.25 10 bar and 50 bar volumetric storage results comparison of Ni^{2+}- ZSM-5 zeolites

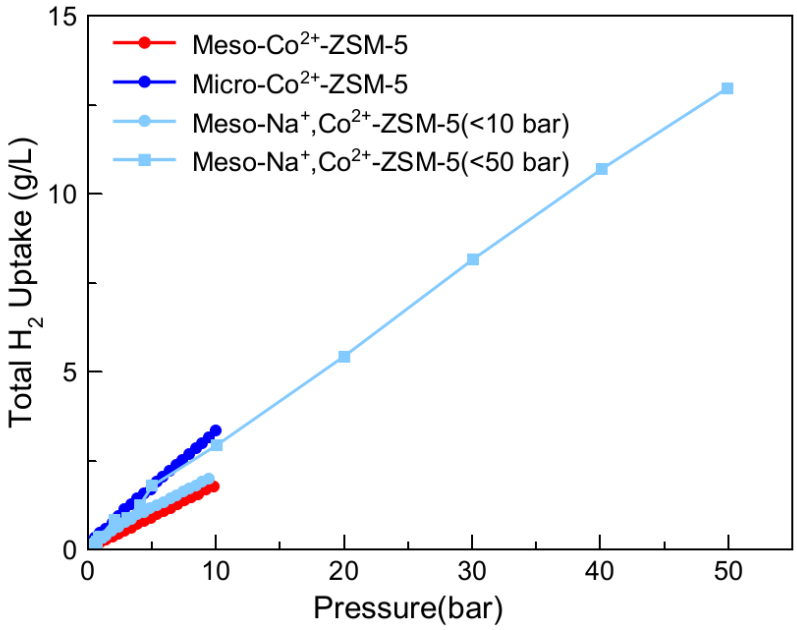

Figure 4.26 10 bar and 50 bar volumetric storage results comparison of Co^{2+}- ZSM-5 zeolites

4.4 Hydrogen Adsorption (77 K, < 1 bar) Results

Hydrogen adsorption experiments at 77 K are performed to determine the maximum storage capacities. The gravimetric and volumetric uptake values of zeolites are given in Figures 4.27 and 4.28. The order of the gravimetric capacities is Meso-Co^{2+}-ZSM-5~Micro-Ni^{2+}-ZSM-5 ~ Meso-Ni^{2+}-ZSM-5(~0.8 wt.%) > Micro-Co^{2+}-ZSM-5 (0.75 wt.%) > Ni^{2+}-US-Y (0.64 wt.%) > Co^{2+}-US-Y (0.6 wt.%). The results are lower than the previously reported 77 K and 1 bar capacity of the zeolites (Li-MOR, Na-ZSM-5, Na-FAU) showing 1.2–0.8 wt.% [95]. In addition, Ni-, Co- MOFs can reach 2 wt.% storage capacity at 77 K and 1 bar [70], but the highest uptake is reached on Meso-Co^{2+}-ZSM-5 by 0.85 wt.% in this study. The gravimetric capacity values are slightly lower than the values reported on NiNa-X (Si/Al = 1.18, Ni/Al = 0.33, 1.04 wt.% at 77 K, 1 bar)[167] and NiNa-Y (Si/Al = 3, Ni/Al = 0.42, 0.92 wt.% at 77 K, 1 bar)[115] that have higher Al, and therefore Ni contents. The main parameter for the storage at 77 K and 1 bar is high micropore volume with a narrow pore openings (<1 nm) for the porous materials [173]. Hence, narrow pore channels of ZSM-5 (5.4 x 5.6 Å) provide high storage capacity than US-Y (14.1 x 15.6 Å) zeolites at 77 K in this study.

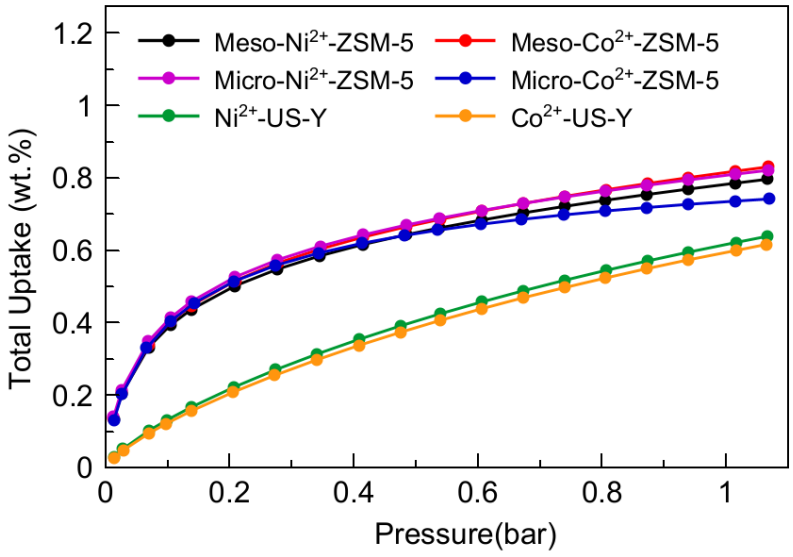

Figure 4.27 Gravimetric capacity of Ni^{2+}, Co^{2+}-zeolites at 77 K and 1 bar

In terms of volumetric storage, Micro-Ni^{2+}- or Co^{2+}-ZSM-5 zeolites show significantly higher capacities than Meso-Ni^{2+}- or Co^{2+}-ZSM-5, Ni^{2+}-US-Y and Co^{2+}- US-Y. The reason is directly related to the total pore volume of the zeolites. For hydrogen storage at 77 K, the heat of the adsorption effect is negligible and the reached 20 H_2/M^{2+} at 1 bar can be evidence for this situation as given in Figure 4.29. At this level of H_2/M^{2+}, hydrogen is adsorbed inside the pores as well as pore walls.

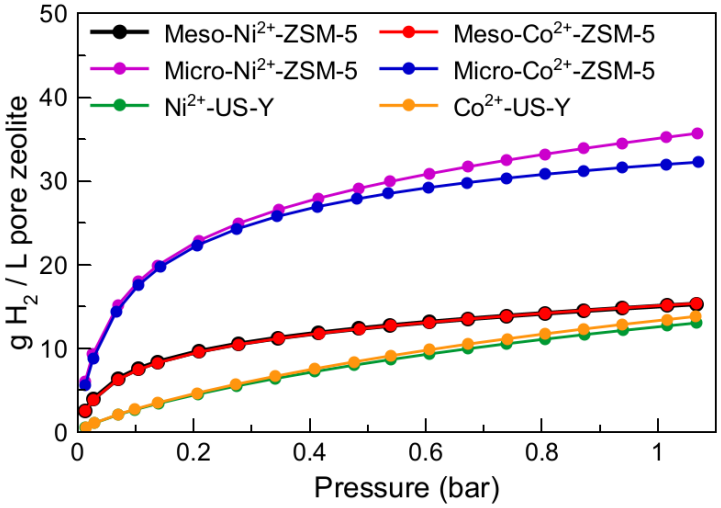

Figure 4.28 Volumetric capacity of Ni^{2+}, Co^{2+}-zeolites at 77 K and 1 bar

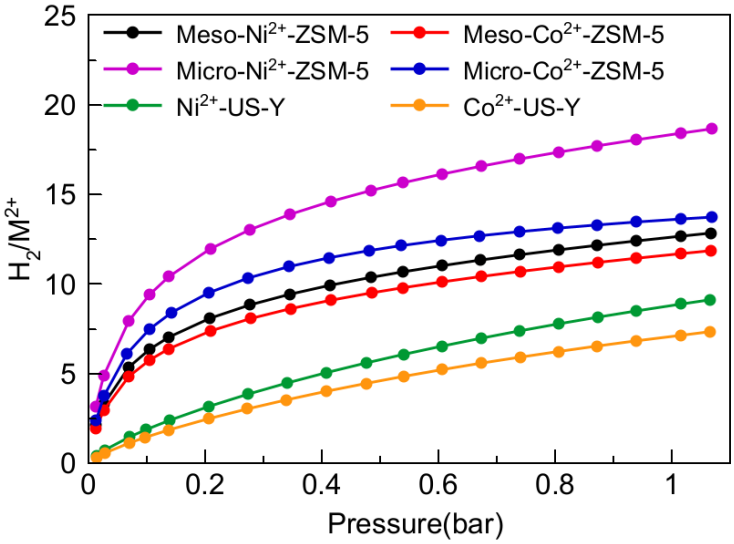

Figure 4.29 H_2/M^{2+} results of Ni^{2+}, Co^{2+}-zeolites at 77 K and 1 bar

The isotherms obtained at 77 K are fitted with a Sips adsorption model (Equation 4.1), which includes the effect of heterogeneous adsorption sites showing different heat of adsorption values.

$$Q_e = \frac{Q_{max} b P^n}{1 + b P^n} \quad \text{(Eqn.4.1)}$$

Q_{max} represents ultimate gravimetric capacity (wt.%) and b is affinity constant. According to the fitting results in Table 4.3, maximum capacity can be reached by US-Y zeolites showing ~2.3 wt.% at saturation. The high pore volume (0.49 cm^3/g) and surface area (1007 m^2/g) of US-Y provide high storage capacity compared to ZSM-5 samples. Therefore, US-Y can be promising material for hydrogen storage at cryogenic temperatures. On the other hand, Micro-Ni^{2+}-ZSM-5 and Micro-Co^{2+}-ZSM-5 show high affinity constants compared to other zeolites in this study. The reason is due to the pore characteristics of zeolites. According to BJH pore size distributions, there are micropores on Micro-Ni^{2+}-ZSM-5 and Micro-Co^{2+}-ZSM-5 whereas Meso-Ni^{2+}-ZSM-5/Meso-Co^{2+}-ZSM-5 and Ni^{2+}-US-Y and Co^{2+}-US-Y show mesopore sizes such as 14 nm and 24 nm respectively. Therefore, smaller pore openings provide a high affinity to hydrogen for Micro-Ni^{2+}-ZSM-5 or Micro-Co^{2+}-ZSM-5.

One similar study belongs to Peedikakkal et al. for Ni,Co-MOF-5. Ni-MOF-5 (0.353 cm^3/g) and Co-MOF-5 (0.223 cm^3/g) show 1.5 wt.% storage capacity at 77 K and 1 bar. After applying the Sips model to isotherms, maximum gravimetric capacity is calculated as 1.53 wt.% in the study. Ni-USY and Co-USY showing ~ 2.3 wt.% maximum gravimetric capacity surpasses the result of Ni,Co-MOF-5 [174].

Table 4.3 Calculated maximum adsorption capacity and Sips adsorption model parameters from adsorption isotherms obtained at 77 K

Sample	Q_{max}(mmol/g)	Wt.%	b (bar^-n)	n	R^2
Meso-Ni^{2+}-ZSM-5	6.191	1.2	1.679	0.584	0.99
Meso-Co^{2+}-ZSM-5	6.666	1.3	1.541	0.579	0.99
Micro-Ni^{2+}-ZSM-5	6.091	1.2	1.919	0.599	0.99
Micro-Co^{2+}-ZSM-5	5.016	1	2.8	0.645	0.99
Ni^{2+}-US-Y	11.41	2.3	0.3701	0.782	1
Co^{2+}-US-Y	11.08	2.2	0.3667	0.798	1

4.5 Diffuse Reflectance UV–Vis Results

Diffuse Reflectance UV–Vis experiments are conducted in order to obtain cation site information on ZSM-5. Moreover, Ni^{2+} and Co^{2+} coordination in US-Y is analyzed. The dehydrated and hydrated spectroscopy results of zeolites are given in Appendix Figure C.1.

There are three cation sites (α, β, and γ) that are preferable due to their framework coordination in ZSM-5. The d-d transition of bare Co^{2+} cations in the UV–Vis spectra of the dehydrated ZSM-5 is characteristic of the individual cationic sites (α, β, and γ). The cation probability on these sites depends on the exchange method, Si/Al, and whether another cation exists in the framework or not. The existence of the Al-(Si-O)$_2$-Al sequence in one ring is crucial to balancing divalent metal cations in zeolites. If two Al tetrahedra are not close enough to balance Co^{2+} cations, then the monovalent Co-OH and Co-oxo species might be balanced by single Al atoms. The observed absorption bands around 15,000 cm^{-1} represents α sites, 16 000, 17 150, 18 600, 21 200 cm^{-1} represents β sites while 20 100, 22 000 cm^{-1} shows γ -type sites

[149]. The quantitative analysis of cation distribution is conducted according to Equation 4.2.

$$[Co] = k_i A_i \quad \text{(Eqn 4.2)}$$

[Co] is the Co concentration in the zeolite, k_i is the absorption coefficient and A_i is the integrated area of the bands corresponding to the i-type Co^{2+} ion. Absorption coefficients are taken as 3.7×10^{-3}, 2.7×10^{-3} and 0.9×10^{-3} for α, β and γ-sites respectively [124,149].

The UV–Vis Spectroscopy results of the zeolites are deconvoluted and Gaussian bands are shown in Figure 4.30. According to the results, β-site is dominant in both Micro-Co^{2+}-ZSM-5(52%) and Meso-Co^{2+}-ZSM-5(47%) zeolites, whereas α and γ sites show similar presence in a range of 21–29%. These results are in line with the reported site distribution in the MFI framework such as β-site (60–85), α(10–40%), and , γ-site (2–12%)[145]. Moreover, it is stated that the Al pair coordination (Al-O-(Si-O)$_2$-Al) is mostly observed on β- site for the Si/Al in the range of 10–35 [127]. The statement is in agreement with the high β- site presence on Micro-Co^{2+}-ZSM-5 and Meso-Co^{2+}-ZSM-5, which have 22 Si/Al.

On the other hand, cations sites order is α(49%)>β(37%)>γ(14%) for Meso-Na^+,Co^{2+}-ZSM-5. The cation distribution on the sites depends on the stabilization energy of the cation, ion-exchange procedure, Si/Al, or competition with another existing cation [145]. It can be inferred that the Na^+ cation content affects the Co^{2+} distribution and results in increasing Co^{2+} content on the α site. A similar result is concluded from the study of Dedecek at al. In the case of higher cobalt content for CoNa-ZSM-5 (>Co/Al=2, ~0.52 Na/Al), β and γ -sites occupations of Co^{2+}-cation decrease sharply, whereas α-site occupation increases gradually. Moreover, α-site occupancy is reported to be almost 10% higher in CoNa-ZSM-5 (Si/Al=14) zeolite compared to the CoH-ZSM-5 (Si/Al=12.5, parent NH_4^+-ZSM-5) in the same study [149].

Co-OH species are not observed in the samples due to the easy dehydroxylation above 723 K [124]. The characteristic band for Co-OH at 7 300 cm^{-1} is not observed

on the UV–Vis spectra [149]. Therefore, it can be inferred that Co^{2+} cations are mostly observed in the form of bare cations. The absorption band at 30 000 cm^{-1}, which represents the charge transition of -oxo, superoxo or peroxo Co species is only observed on Meso-Na^{+},Co^{2+}-ZSM-5 [175].

Co^{2+}-US-Y shows absorption bands around 19 000, 17 200, and 16 000 cm^{-1} which represent pseudo-tetrahedral Co^{2+} cations at sites I' and II in calcined (673 K) zeolite Y [146,147]. In addition, the band at around 25 400 cm^{-1} might be associated with Co^{2+} located in a trigonal planar environment of the oxygen six-membered ring (Site II in Y-zeolite) [176].

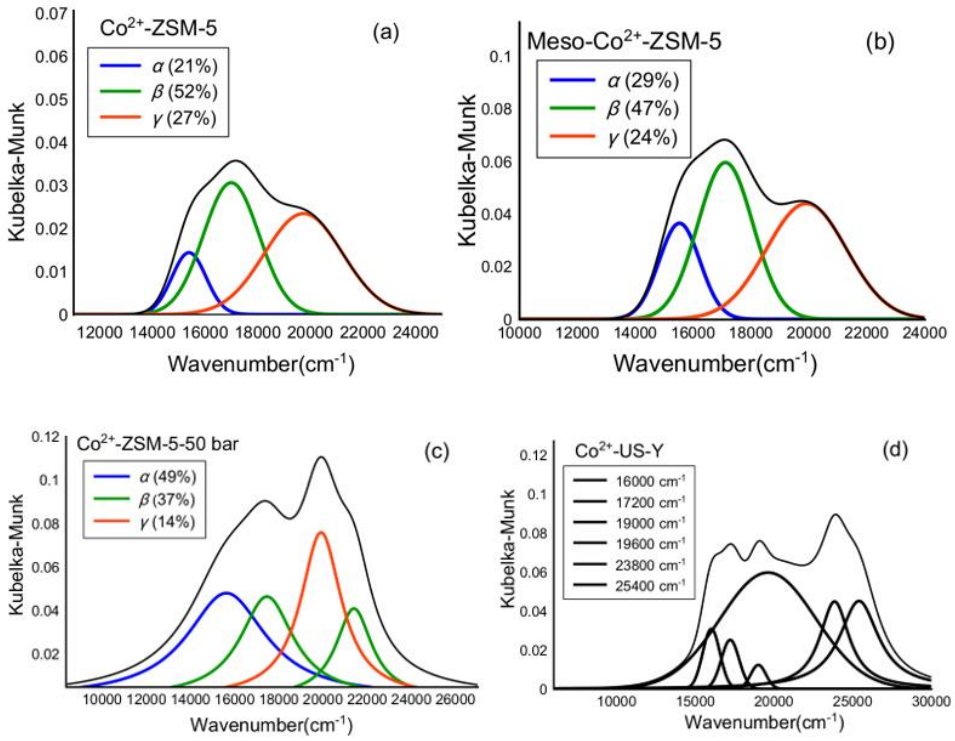

Figure 4.30 DR UV–Vis spectra of dehydrated a) Micro-Co^{2+}-ZSM-5, b) Meso-Co^{2+}-ZSM-5, c) Co^{2+}-ZSM-5-50 bar and d) Co^{2+}-US-Y deconvoluted band fittings

The similar bands are observed on Ni^{2+}-zeolites as given in Figure 4.31. The charge transfer between O^{-2} and Ni^{2+} can be observed in range between 40 000 and 45 000 cm^{-1}[153]. The $Ni(H_2O)_6^{2+}$ complex, where Ni^{2+} is in an octahedral coordination is observed with the bands between 23 000–25 000 cm^{-1} and 8 000–12 000 cm^{-1} [177].

22 000–23 000 cm^{-1} absorption bands show the square planar coordination of bare Ni^{2+}-cations in dehydrated zeolites [178,179]. The bands between 14 000–17 000 cm^{-1} shows tetrahedral (distorted) coordination environments [180]. With regard to Ni^{+2}-US-Y specifically, the 15 000 cm^{-1} band can be attributed to pseudooctahedral symmetric Ni^{2+} ions in Site I. Additionally, reported distorted tetrahedral symmetry for Ni^{+2}-US-Y might be occupied in sodalite cavities (SI′) and/or in supercages (SII) [153].

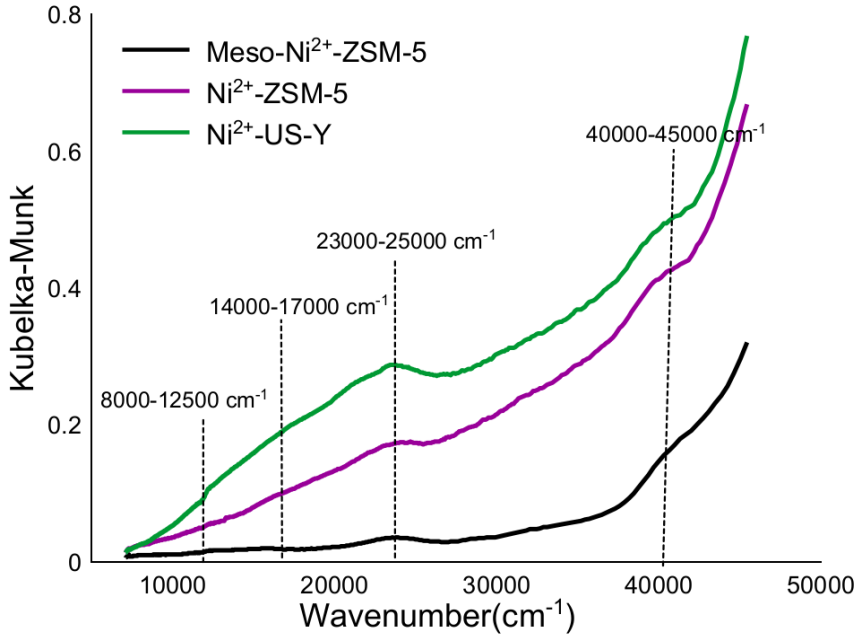

Figure 4.31 DR UV–Vis spectra of dehydrated of Ni^{2+}-zeolites

4.6 Synchrotron Powder XRD (SXRD) Results

Properties like valence state, local atomic coordination, concentration and position of the cation species within the framework structure are crucial parameters for understanding their role in hydrogen storage. Therefore, Synchrotron powder X-Ray Diffraction experiments are performed in order to determine locations of the Ni^{2+} and Co^{2+} cations on the dehydrated Meso-Ni^{2+}-ZSM-5, Micro-Ni^{2+}-ZSM-5, Meso-Co^{2+}-ZSM-5, Micro-Ni^{2+}-ZSM-5, Ni^{2+}-US-Y and Co^{2+}-US-Y. Although it is aimed to analyze the samples in dehydrated form, the partial hydration of the samples could

not be prevented during transferring the samples to the capillaries in a glovebag. The water molecule existence in the framework causes migration of the cations away from the framework oxygen atoms. Additional water molecules are refined as oxygen atoms during the Rietveld refinement analysis according to obtained Fourier map, which shows electron density. The atomic positions and parameters obtained from Rietveld refinement of Meso-Ni^{2+}-ZSM-5, Micro-Ni^{2+}-ZSM-5, Meso-Co^{2+}-ZSM-5, Micro-Ni^{2+}-ZSM-5, Ni^{2+}-US-Y and Co^{2+}-US-Y samples are given in Appendix Table D1-D6 (Synchrotron powder X-Ray Diffraction patterns of zeolites can be found in Appendix Figure D1-D6).

As mentioned before, US-Y zeolite is the member of FAU framework which includes cation sites namely I, I′, II, II′, III, and III′. However, I and I' sites are not accessible to hydrogen. SI is in the center of the hexagonal prism and is surrounded by an octahedron of oxygens while SI′ is in the sodalite cage near the center of the hexagonal window of the prism and is close to three framework oxygen atoms. Both two sides are near to hexagonal prism that is not suitable for the kinetic diameter of the hydrogen (2.89 Å)[115].

Hydrated Co^{2+}-US-Y and Ni^{2+}-US-Y zeolites show similar occupation on the framework. Both cations are detected around the locations which are close to the sites I', II' and III as shown in Figure 4.32. For US-Y zeolite two oxygen atoms (O5, O6) are refined in order to account for non-negligible water existence in the framework. Ni^{2+} cations, having 0.69 Å ionic radii, are found near to 6MR and 4MR windows with Ni^{2+}–$O_{framework}$ distances of 3.79(7) Å and 2.3(2) Å for Ni1 and Ni2 respectively as given in Table 4.4. In addition, Ni^{2+} cations show similar distance (O5: 3.4(2)Å, O6: 2.8(2)Å) to oxygen atoms of water molecules. Similarly, Co2 cations having 0.65 Å ionic radii are detected as in coordination with O atoms of H_2O with a Co2–O(H_2O) distance of 2.85(7) Å for Co^{2+}-US-Y. The distance of cation to oxygens are larger than previously reported Co–$O_{framework}$ distances (ca. 2 Å) for Co^{+2}-Y (Si/Al=1.7) [181]. The difference resulted from the water existence on the samples in this study. The labeled Ni1 and Co1 sites are close to the main sites Site I' and Site II' while Ni2 and Co2 are near to the Site III. The distribution of the

Ni^{2+} cations are found as 26% and 74% for Ni1 and Ni2 positions, while the occupation of Co^{2+} cations are calculated as 29% and 71% for Co1 and Co2, respectively. Hence, the majority of the cation sites on US-Y zeolites are accessible to H_2 molecules.

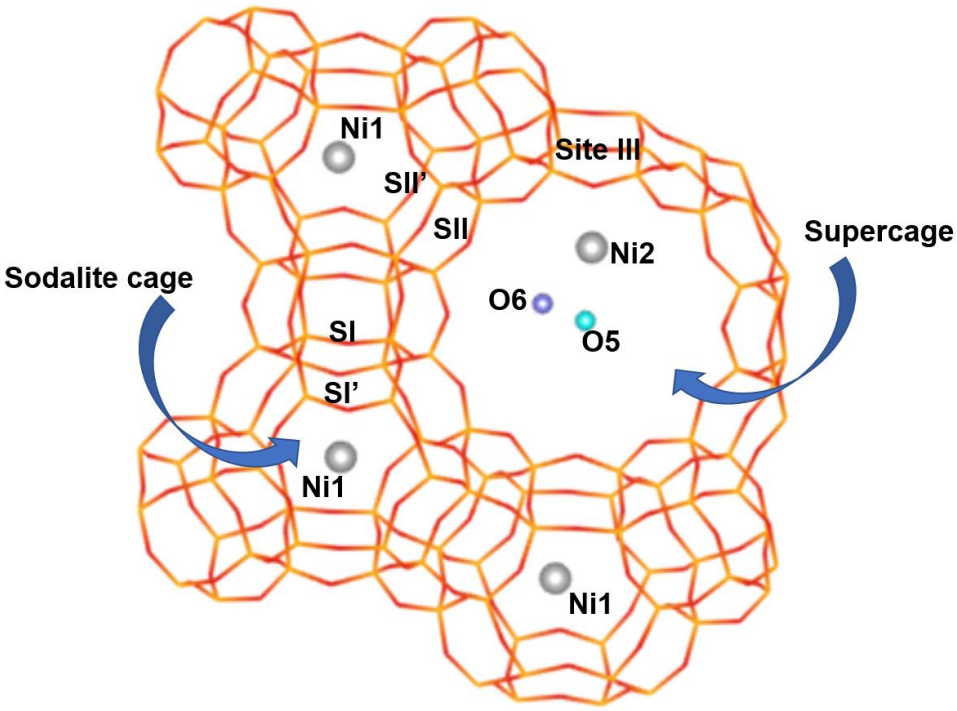

Figure 4.32 Schematic FAU framework (includes sodalite and supercages) of hydrated Ni^{2+}-US-Y, refined in space group $Fd\bar{3}m$ (Si: yellow, Ni: gray, O6: purple, O5: turquoise).

Table 4.4 Co and Ni Distribution and Bond Distances Obtained by Rietveld Analysis of PXRD Data of Co^{2+}-US-Y, Ni^{2+}-US-Y (Cubic, $Fd\bar{3}m$), (SESAME, ID09 MS, λ = 1.03365 Å) (Values in parentheses indicate one standard deviation in the prior digit.)

		M %	**Bond**	**Distance (Å)**
Co^{2+}-US-Y	Co1 (Sodalite)	29	$Co1–O3_{(fw)}$*2	3.56(5)
	Co2 (Supercage)	71	$Co2–O4_{(fw)}$	2.53(6)
			$Co2–O5_{(H2O)}$	2.76(6)
			$Co2–O6_{(H2O)}$	2.85(9)
	a/ Å	24.3290(2)		
	V/ $Å^3$	14400.3(4)		
	wRp/ %	10.68		
Ni^{2+}-US-Y	Ni1 (Sodalite)	26	$Ni1–O3_{(fw)}$*2	3.79(7)
	Ni2 (Supercage)	74	$Ni2–O4_{(fw)}$	2.3(2)
			$Ni2–O5_{(H2O)}$	3.4(2)
			$Ni2–O6_{(H2O)}$	2.8(2)
	a/ Å	24.3474(3)		
	V/ $Å^3$	14433.0(5)		
	wRp/ %	11.59		

The cation distribution representations for ZSM-5 samples are given in Figure 4.33. Three main cation sites are refined (Co1,Co2 and Co3) on Co^{2+}-ZSM-5 and Ni^{2+}-ZSM-5 (Ni1,Ni2 and Ni3) samples. Co1 is on the 10 MR viewed along [100], Co2 is in the 5MR near to β-site and Co3 is at the intersection of the straight and sinusoidal channel (Figure 4.33(a)). It can be inferred that the Co3 cations is not stable enough to be an extraframework cation because of its longer distance than typical 2–4 Å distance from the framework oxygens (closest distance for Co3–$O_{framework}$ is found as 4.06(7) Å). Hence, the presence of this electron density most

probably resulted from the water molecules in the structure. Although the similar cation occupation is observed for also Micro-Ni^{2+}-ZSM-5 and Meso-Ni^{2+}-ZSM-5, Co3 site is not taken into account as a cation site in this study. Table 4.5 shows distribution of cations and bond distances to framework oxygens.

The sites Co2 (Ni2) and Co1 (Ni1) are close to the β-site (plane of 6MR) rather than α or γ-sites. It can be said that extraframework cations are migrated from β-site to the channels due to the water existence. Moreover, the α or γ -sites can not be refined successfully for any ZSM-5 samples.

The framework oxygen and extraframework cation distances are in the same range for all zeolites (1.6–4 Å) as shown in the Table 4.5. The occupation percentage of sites are given also in the Table 4.5. As can be seen, occupation for Co1(Ni1) and Co2(Ni2) are the same for Micro-Ni^{2+}-ZSM-5 and Micro-Co^{2+}-ZSM-5. On the other hand, two sites show different existence in Meso-Ni^{2+}-ZSM-5 and Meso-Co^{2+}-ZSM-5 with a high percentage of Co1(10 MR). The possible reason might be the alkaline medium (desilication) treatment, which is based on removing Si sites from the framework. As can be seen from the Table 4.1, Si/Al decreases from 33 to 20 after desilication.

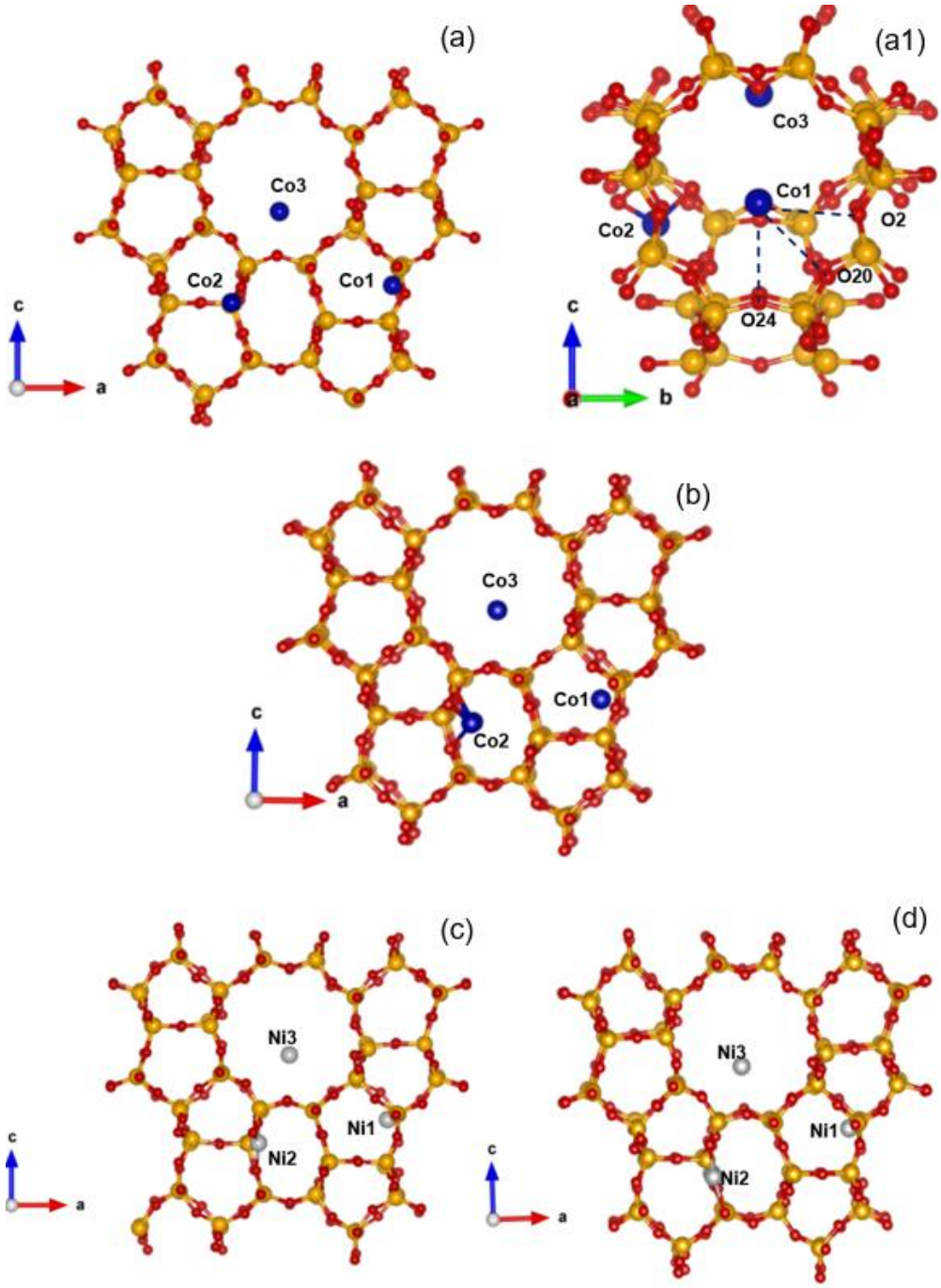

Figure 4.33 Schematic of MFI framework cation locations in a) Micro-Co^{2+}-ZSM-5, a1) Co1 and framework oxygen coordination for Micro-Co^{2+}-ZSM-5 b) Meso-Co^{2+}-ZSM-5 c) Meso-Ni^{2+}-ZSM-5 d) Micro-Ni^{+2}-ZSM-5 refined in space group Pnma (Si: yellow, Co: dark blue, Ni: gray, O: red).

Table 4.5 Co and Ni Distribution and Bond Distances Obtained by Rietveld Analysis of PXRD Data of Micro-Co^{2+}-ZSM-5, Micro-Ni^{2+}-ZSM-5, Meso-Co^{2+}-ZSM-5, Meso-Ni^{2+}-ZSM-5 (Orthorhombic, Pnma) (SESAME, ID09 MS, λ = 1.03365 Å) (Values in parentheses indicate one standard deviation in the prior digit.)

		M %	**Bond**	**Distance (Å)**
Micro-Co^{2+}-ZSM-5	Co1 (10MR)	50	$Co1–O24_{(fw)}$	3.6(1)
			$Co1–O20_{(fw)}$*2	3.60(8)
	Co2 (5MR)	50	$Co2–O16_{(fw)}$	1.61(8)
			$Co2–O15_{(fw)}$	1.90(8)
	a/ Å	20.0182(4)		
	b/ Å	19.8931(5)		
	c/ Å	13.3790(3)		
	V/ $Å^3$	5327.9(2)		
	wRp/ %	9.86		
Micro-Ni^{2+}-ZSM-5	Ni1 (10MR)	52	$Ni1–O2_{(fw)}$*2	3.57(5)
			$Ni1–O20_{(fw)}$*2	3.8(1)
	Ni2 (5MR)	48	$Ni2–O16_{(fw)}$	1.8(1)
			$Ni2–O14_{(fw)}$	2.1(1)
	a/ Å	20.0417(5)		
	b/ Å	19.8769(6)		
	c/ Å	13.3810(4)		
	V/ $Å^3$	5330.6(2)		
	wRp/ %	9.58		

Table 4.5 (Cont'd)

Meso-Co^{2+} -ZSM-5	Co1 (10MR)	66	$Co1–O24_{(fw)}$	3.6(1)
			$Co1–O2_{(fw)}$*2	3.64(4)
	Co2 (β-site)	34	$Co2–O16_{(fw)}$	2.0(3)
			$Co2–O15_{(fw)}$	2.1(3)
	a/ Å	20.1091(4)		
	b/ Å	19.9669(5)		
	c/ Å	13.4229(4)		
	V/ $Å^3$	5389.5(2)		
	wRp/ %	10.47		
Meso-Ni^{2+}-ZSM-5	Ni1 (10MR)	82	$Ni1–O2_{(fw)}$*2	3.67(5)
			$Ni1–O24_{(fw)}$	4.0(1)
	Ni2 (5MR)	18	$Ni2–O15_{(fw)}$	1.4(4)
			$Ni2–O16_{(fw)}$	1.5(5)
	a/ Å	20.0331(5)		
	b/ Å	19.8821(6)		
	c/ Å	13.3769(5)		
	V/ $Å^3$	5328.0(2)		
	wRp/ %	10.10		

4.7 Density Functional Theory (DFT)

Density functional theory studies are performed in order to analyze H_2-zeolite interactions for alkali metal [182] [183], alkaline earth metal [184] [185,186] as well as transition metal [187] [188] [189] [190] cations.

Periodic DFT study is performed for ZSM-5 (MFI framework, Figure 2.7), which includes three main cation sites namely β, α and γ-sites as mentioned before. One of the main aim of the DFT periodic study is to optimize 3 different pair Al (Al-O-(Si-O)$_2$-Al) or (Al-O-(Si-O)-Al) coordination for β, α and γ-sites on the orthorhombic ZSM-5 having lattice parameters a = 20.4598 Å, b = 20.1984 Å and c = 13.5548 Å (Figure 4.34). Afterward, H_2 adsorption is performed on the optimized structure, and the heat of adsorption values are calculated.

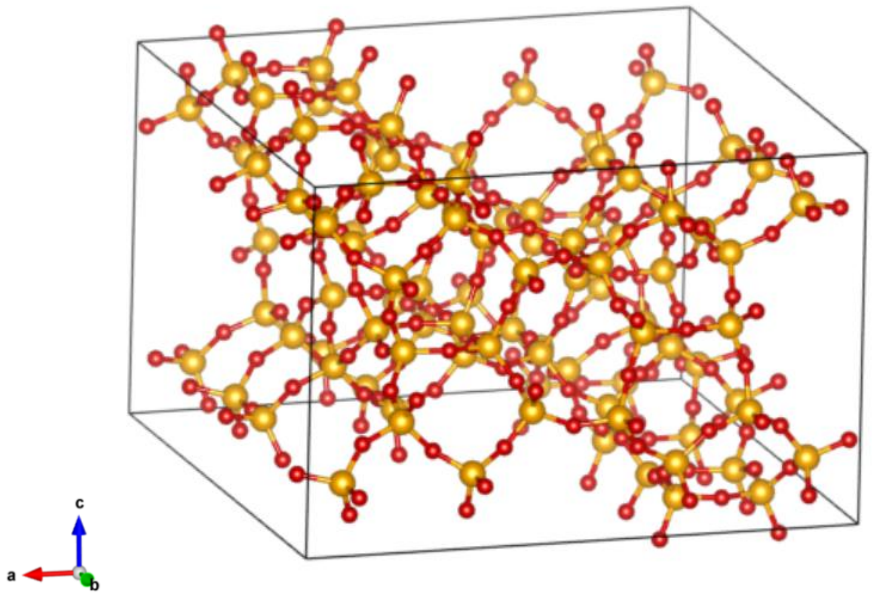

Figure 4.34 Unit cell of optimized ZSM-5 (a = 20.4598 Å, b = 20.1984 Å and c = 13.5548 Å)

Optimized geometries for Ni^{2+} and Co^{2+} cations on cation sites are given in Figure 4.35. According to the results, both cations are more stable in β and γ sites than α site. In addition, the β and γ -sites with 2Al atoms coordinated in opposite sites (Al-O-Si-O-Si-O-Al) in the 6MR are the most favorable site for Co^{2+}- and Ni^{2+} cations,

which show square planar or distorted square planar coordinations with framework oxygen atoms. The observed absorption band (23 000 cm^{-1}, Figure 4.31) on Ni^{2+}-ZSM-5, which represents square planar coordination from the DR UV–Vis study is in agreement with this coordination. This situation explains the statement that has been mentioned in the previous study of Dedecek et al. It is suggested that the Al pair coordination in 6MR (Al-O-(Si-O)$_2$-Al) represents the majority of Al atoms in Si-rich zeolites (Si/Al>12) with an occupation of 84% in ZSM-5 [145]. The Al-O-Si-O-Al sequence shows distorted tetrahedral coordination with Ni^{2+} or Co^{2+} cations resulting high energy values, which makes them less favorable for cations. This situation is also parallel with the statement which the Al-O-Si-O-Al sequence is generally not observed for the high Si-zeolites (Si/Al > 12)[128,191].

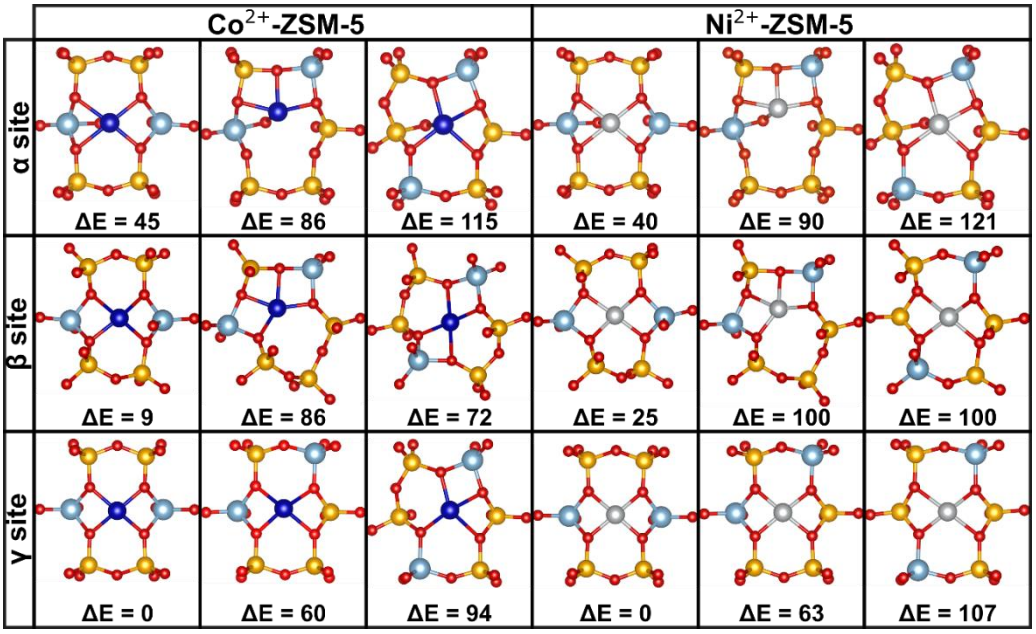

Figure 4.35 Optimized geometries and relative energies (kJ/mol) of Co^{2+}-ZSM-5 and Ni^{2+}-ZSM-5 using DFT

The heat of adsorption results of the optimized structures is given in Figure 4.36. Lower heat of adsorption values is obtained for more stable cation sites as presented in Figure 4.36. The highest heat of adsorption is observed for Co^{2+}-ZSM-5 with ΔH = -35 kJ/mol in α-site. The most stable cation sites (γ, β, Figure 4.36, Configuration

1) for Ni and Co show lower heats of H_2 adsorption by -12 kJ/mol and -13 kJ/mole respectively.

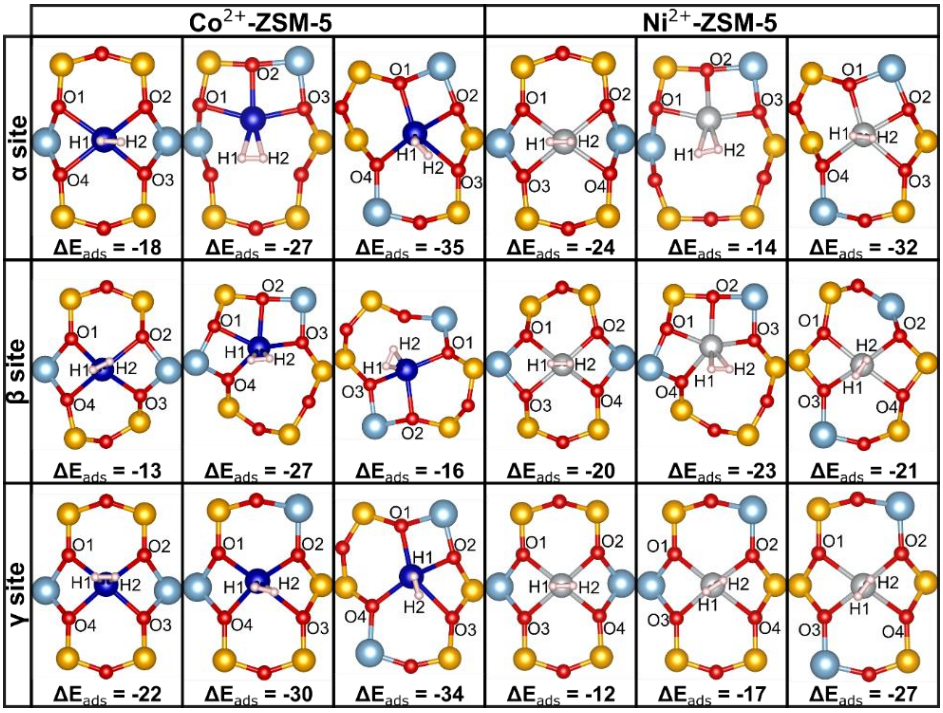

Figure 4.36 Optimized geometries, distances (Å) and energies (kJ/mol) of the H_2 adsorption on Co^{2+} and Ni^{2+} cations located at α, β and γ -sites in Co^{2+}-ZSM-5 and Ni^{2+}-ZSM-5 using periodic DFT models. (Si: yellow, Al: light blue, Co: dark blue, Ni: gray, O: red, H:pink)

The H_2 binds side on to the metal cation primarily via donation of its two σ electrons to a vacant d orbital [192]. Extaframework cations on zeolites have an activation for π bonds and also σ bonds of the H_2. There could be three main factors affect the hydrogen activation with cations: σ donation from H_2 molecule to the cation, π back donation from the cation to H_2 molecule and H_2 molecule interaction with framework oxygen. Moreover, low coordination number of cations on the framework can enhance the interaction between framework oxygen and H_2[109].

$Co–O_{framework}$ and $Ni–O_{framework}$ distances are ~2 Å as expected for dehydrated cations. As given in Table 4.6, the M^{2+}–H lengths are around 1.8 Å which show stronger interaction when compared to van der Waals interaction with an expected contact distance around 3 Å [36].

H-H bond length shows a slight elongation from the free H-H bond length (0.74 Å) with a bond length around ~0.79 Å on the cation sites. In this study, the observed elongation H-H bond express the filling of the hydrogen antibonding orbital (σ^*) through backdonation from the metal d orbitals. In addition, M–H distances that are around 1.8 Å shows the electron donation from H_2 bonding (σ) orbitals to s-and d-orbitals of the metal cations strengthening the H_2–metal bond.

Table 4.6 Interatomic distances (Å) for H_2 adsorption on metal cation (Ni^{2+} and Co^{2+}) containing sites calculated using DFT

	Co^{2+} in α-1	**Co^{2+} in α-2**	**Co^{2+} in α-3**	**Ni^{2+} in α-1**	**Ni^{2+} in α-2**	**Ni^{2+} in α-3**
M – O1	2.1549	2.0773	2.0721	2.1471	2.0918	2.0943
M – O2	2.0782	2.0635	2.0328	2.0780	1.9939	2.0789
M – O3	2.0629	1.9943	2.3533	2.0466	2.0093	2.1976
M – O4	2.1612	NA	2.0194	2.1480	NA	2.1098
M – H1	1.9672	1.7578	1.8489	1.8506	1.7916	1.8315
M – H2	1.9822	1.7578	1.8409	1.8581	1.7719	1.8351
H1 – H2	0.7744	0.8000	0.7861	0.7790	0.7951	0.7821
	Co^{2+} in β-1	**Co^{2+} in β-2**	**Co^{2+} in β-3**	**Ni^{2+} in β-1**	**Ni^{2+} in β-2**	**Ni^{2+} in β-3**
M – O1	1.9956	2.1226	NA	1.9946	2.0884	2.1192
M – O2	2.1822	2.1691	1.9522	2.0546	2.0553	1.9913
M – O3	2.0118	2.0433	1.9417	2.0434	2.0884	2.0733
M – O4	2.0258	1.9731	2.1338	2.0450	1.9963	2.0287
M – H1	1.8696	1.8366	1.8701	1.7824	1.7687	1.7904
M – H2	1.8813	1.8589	1.8696	1.8112	1.7974	1.7854
H1 – H2	0.7835	0.7886	0.7888	0.7926	0.7940	0.7905
	Co^{2+} in γ-1	**Co^{2+} in γ-2**	**Co^{2+} in γ-3**	**Ni^{2+} in γ-1**	**Ni^{2+} in γ-2**	**Ni^{2+} in γ-3**
M – O1	2.0472	1.9745	2.0837	2.0247	1.9978	2.1487
M – O2	2.0472	1.9970	1.9998	2.0246	2.0124	1.9967
M – O3	2.0337	2.3481	2.3629	2.0179	2.1545	2.1279
M – O4	2.0337	2.0165	1.9973	2.0179	2.0108	1.9952
M – H1	1.7972	1.8248	1.8411	1.7717	1.7545	1.7559
M – H2	1.7972	1.8228	1.8489	1.7717	1.7617	1.7545
H1 – H2	0.7940	0.7901	0.7863	0.7925	0.7952	0.7973

Cluster model DFT study is performed for the sites α and γ for the same coordinations given in Figure 4.37 (optimized structure can be found in Appendix Figure E1 and Figure E2 for Co^{2+} and Ni^{2+} cations respectively). The calculated heat of adsorption values for DFT periodic model, DFT cluster model and isosteric heats ($-Q_{st}$) are given in Table 4.7. According to the results, the cluster model overestimates $-E_{ads}$ values for Ni^{2+}-ZSM-5 and underestimates for Co^{2+}-ZSM-5, compared to the periodic model results. Overall, experimentally calculated $-Q_{st}$ values are in the range of both periodic and cluster models. Specific to cluster model, Ni^{2+} and Co^{2+} cations at the γ-sites are in the same line with the experimental values. The occupation of γ sites on the samples obtained from DR UV–Vis results (Figure 4.30) support the observed similarity.

As mentioned before, square planar coordination is the most favorable coordination for the cations and mainly observed on the sites β and γ. Moreover, β-site existence is concluded from the Synchrotron powder X-Ray Diffraction experiments for ZSM-5 samples. DR UV–Vis absorption results show also dominant existence of β sites with a considerable γ occupation for Co^{2+}-ZSM-5 samples (Figure 4.30). Therefore, it can be expected that the hydrogen adsorption mostly taken place on β and γ sites on Co^{2+}-ZSM-5 zeolites.

On the other hand, the absorption bands at 21 000–23 000 cm^{-1} in the DR UV–Vis spectra (Figure 4.7) is assigned as square-planar coordination of bare Ni^{2+} cation for Ni^{2+}-ZSM-5. As a parallel result the most favorable optimized geometries for the cations are found for β and γ -sites showing square planar coordination. Therefore, it is expected that the hydrogen adsorption probability on β and γ -sites is high also in the Ni^{2+}-ZSM-5 samples.

Additionally, noticeable higher heat of adsorption values (-27– -40 kJ/mol) are observed for Ni^{2+}-ZSM-5 when compared to Co^{2+}-ZSM-5 (Figure 4.19). Hence, the higher heat of adsorption values computed for α-site for Ni^{2+}-ZSM-5 could indicate additional occupation of α-sites for this sample.

Although there is not a specific computational study for the H_2 interaction with the Co^{2+} and Ni^{2+} -exchanged FAU framework, the calculated -15 – -25 kJ/mol heat of adsorption values for Co^{2+} and Ni^{2+} located in the 6MR window of CHA by DFT study of Ozbek et al. [193], can be approximated for the Site I' and Site II in FAU framework. The calculated initial isosteric heats of Ni^{2+}-US-Y (-23 kJ/mol) and Co^{2+}-US-Y(-19 kJ/mol) are in the same line with the reported DFT study.

Table 4.7 Experimental and theoretical (DFT) heat of H_2 adsorption values for Co^{2+}-ZSM-5 and Ni^{2+}-ZSM-5

	DFT Cluster Model Gaussian (-E_{ads} kJ/mol)		**DFT Periodic Model (-E_{ads} kJ/mol)**		**Experimental (-Q_{st} kJ/mol)**	
	Co^{2+}-ZSM-5	Ni^{2+}-ZSM-5	Co^{2+}-ZSM-5	Ni^{2+}-ZSM-5	Co^{2+}-ZSM-5	Ni^{2+}-ZSM-5
***α* 1**	7	81	18	24	13–16	24–40
***α* 2**	8	10	27	14		
***α* 3**	9	44	35	32		
***β* 1**	-	-	13	20		
***β* 2**	-	-	27	23		
***β* 3**	-	-	16	21		
***γ* 1**	4	25	22	12		
***γ* 2**	16		30	17		
***γ* 3**	13	30	34	27		

CHAPTER 5

CONCLUSION

To conclude, microporous and mesopore added Ni^{2+}- and Co^{2+}- zeolites were analyzed for hydrogen storage. The development of zeolitic materials to reach the targets (5 wt.%, 40 g H_2/L) assigned by the Department of Energy (DOE) were aimed in this study. The zeolites chosen for the study were ZSM-5 and US-Y.

In the first part of the study, the microporous ZSM-5 zeolites were prepared hydrothermally. In order to overcome pore volume restriction for zeolites, mesopore addition to ZSM-5 samples was prepared by the soft templating and desilication method. As an example, the total pore volume of one of the microporous ZSM-5 (0.22 cm^3/g) was increased to 0.54 cm^3/g by the addition of 0.43 cm^3/g mesopore volume using the desilication method. The US-Y zeolites showed a total pore volume of around 0.46 cm^3/g. Targeted high Ni^{2+} and Co^{2+} content of the zeolites was successfully obtained by 0.18–0.42 mmol M^{2+}/g zeolite ratios.

In the second part, hydrogen storage experiments at ambient temperature and <10 bar were performed. The isosteric heat of adsorption values ($-Q_{st}$) were calculated by using three different isotherms performed at the 293–338 K temperature range up to 10 bar. The heat of adsorption values of Ni^{2+}, Co^{2+}-zeolites were found close to the assigned optimum heat of adsorption range for 100 bar adsorption and 5 bar desorption. The similar H_2/M^{2+} trends observed on Micro-Ni^{2+}-ZSM-5 and Meso-Ni^{2+}-ZSM-5 showed that the pore volume effect had not started until 10 bar. In addition, the Ni^{2+}, Co^{2+}-zeolites showed the same order on both H_2/M^{2+} and isosteric heats that claimed hydrogen was mainly adsorbed on extraframework cation sites. Consequently, Ni^{2+}-zeolites showed higher heat of adsorption values ($-Q_{st}$=23–40

kJ/mol) than Co^{2+}-zeolites ($-Q_{st}$=15–19 kJ/mol), hence Ni^{2+}-zeolites showed higher gravimetric capacity.

High pressure experiments were performed at 298 K and < 50 bar in the third part of the study. The high H_2/M^{2+} ratios (6–14 H_2/M^{2+}) at 50 bar showed that the hydrogen was adsorbed on pore surfaces as well as cation centers. Ni^{2+}-,Co^{2+}-ZSM-5 samples showed higher volumetric capacity than Ni^{2+}-,Co^{2+}-US-Y because of the advantage of the smaller cage size of ZSM-5 (5.4 x 5.6 Å) when compared to US-Y (14.1 x 15.6 Å). Smaller cages were known to increase the Van der Waals interactions. Although large cage size and possible inaccessible sites decreased the H_2 storage capacity of US-Y at 50 bar, they were predicted to be promising materials for higher pressure storage (100 bar) due to high pore volumes (0.49 cm^3/g) and high surface area (~1000 m^2/g). 20 g H_2/L volumetric capacity, which was obtained on Meso-Na^+,Ni^{2+}-ZSM-5 at 298 K and 50 bar, was a promising result for achieving the 40 g H_2/L set by DOE for 100 bar pressure storage. As an important parameter to evaluate materials for hydrogen storage, the Ni^{2+}-, Co^{2+}-zeolites showed reversibility except for Ni^{2+}-US-Y. High volumetric capacity along with reversible storage on ZSM-5 makes them highly promising materials for hydrogen storage for ambient temperature storage.

In order to observe the ultimate storage capacity of the zeolites, 77 K experiments were performed up to 1 bar. According to the Sips isotherm model results, US-Y showed promising results because of its high surface area and pore volume. Therefore, US-Y may also be appropriate material for lower temperature storage in addition to higher H_2 adsorption pressure storage (~100 bar). Also, according to the same experiment, mesopore addition on ZSM-5 showed improvement under specified conditions. However, these improvements couldnot be observed at 298 K. This is due to the fact that at pressures lower than 50 bar, micropores showed higher surface interaction with hydrogen, which was the dominant phenomenon. The effect of mesopores starts to become significant after the micropores are fully filled which can be observed at higher pressures (~100 bar) or at low temperature adsorption.

According to the DR UV–Vis study, β-site occupation was dominant in both Micro-Co^{2+}-ZSM-5 (52%) and Meso-Co^{2+}-ZSM-5 (47%), whereas Na^{+} content in Meso-Na^{+},Co^{2+}-ZSM-5 resulted in higher occupation for α sites (49%). Ni^{2+}-zeolites showed mostly square planar coordination on the framework. The cation locations in the Ni^{2+}-, Co^{2+}-zeolites were also analyzed by synchrotron powder X-ray Diffraction. The refined cation sites were close to the β sites on ZSM-5 similar to the obtained high occupation of β sites from DR UV–Vis. Three different cation sites (I', II', and III) were found for Ni^{2+}-, Co^{2+}-US-Y with a high occupation (~ 70 %) around Site III, which was an accessible site for H_2 molecules.

From periodic Density Functional Theory study, it was concluded that the β and γ -sites in the 6MR with 2Al atoms coordinated in the opposite sites (Al-O-Si-O-Si-O-Al) were the most favorable sites for Co^{2+}- and Ni^{2+} cations, which showed square planar coordination. As a result of DR UV–Vis, Synchrotron powder X-Ray Diffraction, and density functional theory (DFT) studies, it was concluded that hydrogen adsorption mostly taken place on β and γ sites on Co^{2+}-ZSM-5 and Ni^{2+}-ZSM-5 zeolites. Moreover, hydrogen adsorption on α site can be estimated for Ni^{2+}-ZSM-5 samples because of showing moderately high heat of adsorption values (-Q_{st}=24–40 kJ/mol) that were close to theoretically calculated α site heat of adsorption values. Periodic and cluster DFT models predicted the heat of adsorption values in agreement with the experimentally calculated isosteric heat of adsorption (-Q_{st}) values.

REFERENCES

[1] Agyekum EB, Nutakor C, Agwa AM, Kamel S. A Critical Review of Renewable Hydrogen Production Methods : Factors Affecting Their Scale-Up and Its Role in Future Energy Generation. Membranes (Basel) 2022;12:173.

[2] Singla MK, Nijhawan P, Oberoi AS. Hydrogen fuel and fuel cell technology for cleaner future: a review. Environ Sci Pollut Res 2021;28:15607–26.

[3] Crippa, M., Guizzardi, D., Solazzo, E., Muntean, M., Schaaf, E., Monforti-Ferrario, F., Banja, M., Olivier, J., Grassi, G., Rossi, S. and Vignati E. GHG emissions of all world countries. Luxembourg: 2021.

[4] Abe JO, Popoola API, Ajenifuja E, Popoola OM. Hydrogen energy, economy and storage: Review and recommendation. Int J Hydrogen Energy 2019;44:15072–86.

[5] Wang M, Wang G, Sun Z, Zhang Y, Xu D. Review of renewable energy-based hydrogen production processes for sustainable energy innovation. Glob Energy Interconnect 2019;2:436–43.

[6] Capurso T, Stefanizzi M, Torresi M, Camporeale SM. Perspective of the role of hydrogen in the 21st century energy transition. Energy Convers Manag 2022;251:114898.

[7] IEA. Net Zero by 2050: A Roadmap for the Global Energy Sector. Int Energy Agency 2021:224.

[8] Cullen DA, Neyerlin KC, Ahluwalia RK, Mukundan R, More KL, Borup RL, et al. New roads and challenges for fuel cells in heavy-duty transportation. Nat Energy 2021;6:462–474.

[9] International IEA, Agency E. Global Hydrogen Review 2021. Paris: 2021.

[10] Mcwilliams B, Zachmann G. Navigating through hydrogen. Bruegel: 2021.

[11] Rungsima Yeetsorn and Yaowaret Maiket. Hydrogen Fuel Cell Implementation for the Transportation Sector. Adv. Appl. Hydrog. Eng. Syst.

Automot. Ind., London: 2020.

[12] Manoharan Y, Hosseini SE, Butler B, Alzhahrani H, Senior BTF, Ashuri T, et al. Hydrogen fuel cell vehicles; Current status and future prospect. Appl Sci 2019;9.

[13] Wang Y, Chen K, Mishler J, Adroher XC, Cho C, Adroher C. A review of polymer electrolyte membrane fuel cells: Technology, applications, and needs on fundamental research 2011.

[14] Manoharan Y, Hosseini SE, Butler B, Alzahrani H. Hydrogen Fuel Cell Vehicles; Current Status and Future Prospect 2019.

[15] Gröger O, Soc JE, Gr O, Gasteiger HA, Suchsland J. Review—Electromobility: Batteries or Fuel Cells? 2015.

[16] Ioannis V, Hariklia N, Degn A, Pape T, Anne S. Power to fuels and chemicals innovation challenge. In Accelerating the clean energy revolution - perspectives on innovation challenges: DTU International Energy Report 2018. Denmark: 2018.

[17] Sreedhar I, Kamani KM, Kamani BM, Reddy BM, Venugopal A. A Bird's Eye view on process and engineering aspects of hydrogen storage. Renew Sustain Energy Rev 2018;91:838–60.

[18] Schlapbach L, Züttel A. Hydrogen-storage materials for mobile applications. Nature 2001;414:353–8.

[19] U.S. Department of Energy. Target Explanation Document : Onboard Hydrogen Storage for Light-Duty Fuel Cell Vehicles 2017.

[20] Gómez-Gualdrón DA, Wang TC, García-Holley P, Sawelewa RM, Argueta E, Snurr RQ, et al. Understanding volumetric and gravimetric hydrogen adsorption trade-off in metal-organic frameworks. ACS Appl Mater Interfaces 2017;9:33419–28.

[21] Ahmed A, Liu Y, Purewal J, Tran LD, Wong-Foy AG, Veenstra M, et al. Balancing gravimetric and volumetric hydrogen density in MOFs. Energy

Environ Sci 2017;10:2459–71.

[22] Hassan IA, Ramadan HS, Saleh MA, Hissel D. Hydrogen storage technologies for stationary and mobile applications : Review , analysis and perspectives. Renew Sustain Energy Rev 2021;149:111311.

[23] 2022 MIRAI Full Specs n.d. https://www.toyota.com/mirai/features/hydrogen_tank/3002/3003.

[24] Aziz M. Liquid hydrogen: A review on liquefaction, storage, transportation, and safety. Energies 2021;14:5917.

[25] Andersson J, Grönkvist S. Large-scale storage of hydrogen. Int J Hydrogen Energy 2019;44:11901–19.

[26] Yang J, Sudik A, Wolverton C, Siegel DJ. High capacity hydrogen storage materials: Attributes for automotive applications and techniques for materials discovery. Chem Soc Rev 2010;39:656–75.

[27] Yartys VA, Lototskyy M V., Akiba E, Albert R, Antonov VE, Ares JR, et al. Magnesium based materials for hydrogen based energy storage: Past, present and future. Int J Hydrogen Energy 2019;44:7809–59.

[28] Crivello JC, Dam B, Denys R V., Dornheim M, Grant DM, Huot J, et al. Review of magnesium hydride-based materials: development and optimisation. Appl Phys A Mater Sci Process 2016;122:1–20.

[29] Orimo SI, Nakamori Y, Eliseo JR, Züttel A, Jensen CM. Complex hydrides for hydrogen storage. Chem Rev 2007;107:4111–32.

[30] Ozolins V, Majzoub EH, Wolverton C. First-principles prediction of thermodynamically reversible hydrogen storage reactions in the Li-Mg-Ca-B-H system. J Am Chem Soc 2009;131:230–7.

[31] Bogdanović B, Brand RA, Marjanović A, Schwickardi M, Tölle J. Metal-doped sodium aluminium hydrides as potential new hydrogen storage materials. J Alloys Compd 2000;302:36–58.

[32] Modi P, Aguey-Zinsou KF. Room Temperature Metal Hydrides for Stationary

and Heat Storage Applications: A Review. Front Energy Res 2021;9:1–25.

[33] Fernández JF, Sánchez CR. Rate determining step in the absorption and desorption of hydrogen by magnesium. J Alloys Compd 2002;340:189–98.

[34] Zhang X, Liu Y, Ren Z, Zhang X, Hu J, Huang Z, et al. Realizing 6.7 wt% reversible storage of hydrogen at ambient temperature with non-confined ultrafine magnesium hydrides. Energy Environ Sci 2021;14:2302–13.

[35] Allendorf MD, Hulvey Z, Gennett T, Ahmed A, Autrey T, Camp J, et al. An assessment of strategies for the development of solid-state adsorbents for vehicular hydrogen storage. Energy Environ Sci 2018;11:2784–812.

[36] Lochan RC, Head-Gordon M. Computational studies of molecular hydrogen binding affinities: The role of dispersion forces, electrostatics, and orbital interactions. Phys Chem Chem Phys 2006;8:1357–70.

[37] Georgiadis AG, Charisiou ND, Goula MA. Removal of hydrogen sulfide from various industrial gases: A review of the most promising adsorbing materials. Catalysts 2020;10.

[38] Bhatia SK, Myers AL. Optimum conditions for adsorptive storage. Langmuir 2006;22:1688–700.

[39] Garrone E, Bonelli B, Otero Areán C. Enthalpy-entropy correlation for hydrogen adsorption on zeolites. Chem Phys Lett 2008;456:68–70.

[40] Bae YS, Snurr RQ. Optimal isosteric heat of adsorption for hydrogen storage and delivery using metal-organic frameworks. Microporous Mesoporous Mater 2010;132:300–3.

[41] Jhung SH, Kim HK, Yoon JW, Chang JS. Low-temperature adsorption of hydrogen on nanoporous aluminophosphates: Effect of pore size. J Phys Chem B 2006;110:9371–4.

[42] Assoualaye G, Djongyang N. Influence of pore size and isosteric heat of adsorption of some metal–organic frameworks on the volumetric and gravimetric adsorption capacities of hydrogen at room temperature. Polym

Bull 2021;78:4987–5001.

[43] Bahadur J, Contescu CI, Ramirez-Cuesta AJ, Mamontov E, Gallego NC, Cheng Y, et al. Properties of immobile hydrogen confined in microporous carbon. Carbon N Y 2017;117:383–92.

[44] Sethia G, Sayari A. Activated carbon with optimum pore size distribution for hydrogen storage. Carbon N Y 2016;99:289–94.

[45] Yushin G, Dash R, Jagiello J, Fischer JE, Gogotsi Y. Carbide-derived carbons: Effect of pore size on hydrogen uptake and heat of adsorption. Adv Funct Mater 2006;16:2288–93.

[46] Goldsmith J, Wong-Foy AG, Cafarella MJ, Siegel DJ. Theoretical limits of hydrogen storage in metal-organic frameworks: Opportunities and trade-offs. Chem Mater 2013;25:3373–82.

[47] Reviews C. Introduction to Metal − Organic Frameworks 2012:673–4.

[48] Jiao L, Yen J, Seow R, Skinner WS, Wang ZU, Jiang H. Metal – organic frameworks : Structures and functional applications. Mater Today 2019;27:43–68.

[49] Aghajanloo M, Rashidi AM. Synthesis of Zinc-Organic Frameworks Nano Adsorbent and their Application for Methane Adsorption. J Chem Eng Process Technol 2014;05.

[50] Broom DP, Webb CJ, Fanourgakis GS, Froudakis GE, Trikalitis PN, Hirscher M. Concepts for improving hydrogen storage in nanoporous materials. Int J Hydrogen Energy 2019;44:7768–79.

[51] Gangu KK, Maddila S, Mukkamala SB, Jonnalagadda SB. Characteristics of MOF, MWCNT and graphene containing materials for hydrogen storage: A review. J Energy Chem 2019;30:132–44.

[52] Latroche M, Surblé S, Serre C, Mellot-Draznieks C, Llewellyn PL, Lee JH, et al. Hydrogen storage in the giant-pore metal-organic frameworks MIL-100 and MIL-101. Angew Chemie - Int Ed 2006;45:8227–31.

[53] Dinča M, Dailly A, Liu Y, Brown CM, Neumann DA, Long JR. Hydrogen storage in a microporous metal-organic framework with exposed Mn2+ coordination sites. J Am Chem Soc 2006;128:16876–83.

[54] Mallick A, Saha S, Pachfule P, Roy S, Banerjee R. Selective CO2 and H2 adsorption in a chiral magnesium-based metal organic framework (Mg-MOF) with open metal sites. J Mater Chem 2010;20:9073–80.

[55] Cheon YE, Park J, Suh MP. Selective gas adsorption in a magnesium-based metal-organic framework. Chem Commun 2009:5436–8.

[56] Gedrich K, Senkovska I, Klein N, Stoeck U, Henschel A, Lohe MR, et al. A highly porous metal-organic framework with open nickel sites. Angew Chemie - Int Ed 2010;49:8489–92.

[57] Li Y, Xie L, Liu Y, Yang R, Li X. Favorable hydrogen storage properties of M(HBTC)(4,4′-bipy) ·3DMF (M = Ni and Co). Inorg Chem 2008;47:10372–7.

[58] Wang X Sen, Shengqian M, Rauch K, Simmons JM, Yuan D, Wang X, et al. Metal-organic frameworks based on double-bond-coupled Di-isophthalate linkers with high hydrogen and methane uptakes. Chem Mater 2008;20:3145–52.

[59] Berg AWC Van Den, Area CO. Materials for hydrogen storage : current research trends and perspectives 2008:668–81.

[60] Collins DJ, Zhou H. Hydrogen storage in metal-organic frameworks 2014.

[61] Furukawa H, Ko N, Go YB, Aratani N, Choi SB, Choi E, et al. Ultrahigh porosity in metal-organic frameworks. Science (80-) 2010;329:424–8.

[62] Wong-Foy AG, Matzger AJ, Yaghi OM. Exceptional H2 saturation uptake in microporous metal-organic frameworks. J Am Chem Soc 2006;128:3494–5.

[63] Farha OK, Yazaydin AÖ, Eryazici I, Malliakas CD, Hauser BG, Kanatzidis MG, et al. De novo synthesis of a metal-organic framework material featuring ultrahigh surface area and gas storage capacities. Nat Chem 2010;2:944–8.

[64] Panella B, Hirscher M, Pütter H, Müller U. Hydrogen adsorption in metal-organic frameworks: Cu-MOFs and Zn-MOFs compared. Adv Funct Mater 2006;16:520–4.

[65] Sumida K, Hill MR, Horike S, Dailly A, Long JR. Synthesis and hydrogen storage properties of Be12(OH) 12(1,3,5-benzenetribenzoate)4. J Am Chem Soc 2009;131:15120–1.

[66] Dietzel PDC, Georgiev PA, Eckert J, Blom R, Strässle T, Unruh T. Interaction of hydrogen with accessible metal sites in the metal-organic frameworks M2(dhtp) (CPO-27-M; M = Ni, Co, Mg). Chem Commun 2010;46:4962–4.

[67] Ma S, Zhou HC. A metal-organic framework with entatic metal centers exhibiting high gas adsorption affinity. J Am Chem Soc 2006;128:11734–5.

[68] Kapelewski MT, Geier SJ, Hudson MR, Stück D, Mason JA, Nelson JN, et al. M2(m-dobdc) (M = Mg, Mn, Fe, Co, Ni) metal-organic frameworks exhibiting increased charge density and enhanced H2 binding at the open metal sites. J Am Chem Soc 2014;136:12119–29.

[69] Kapelewski MT, Runčevski T, Tarver JD, Jiang HZH, Hurst KE, Parilla PA, et al. Record High Hydrogen Storage Capacity in the Metal-Organic Framework Ni2(m-dobdc) at Near-Ambient Temperatures. Chem Mater 2018;30:8179–89.

[70] Pham T, Forrest KA, Banerjee R, Orcajo G, Eckert J, Space B. Understanding the H2 sorption trends in the M-MOF-74 series (M = Mg, Ni, Co, Zn). J Phys Chem C 2015;119:1078–90.

[71] Areán CO, Chavan S, Cabello CP, Garrone E, Palomino GT. Thermodynamics of Hydrogen Adsorption on Metal-Organic Frameworks. ChemPhysChem 2010;11:3237–42.

[72] Vitillo JG, Regli L, Chavan S, Ricchiardi G, Spoto G, Dietzel PDC, et al. Role of Exposed Metal Sites in Hydrogen Storage in MOFs 2008:8386–96.

[73] Zhou W, Wu H, Yildirim T. Enhanced H 2 Adsorption in Isostructural Metal

- Organic Frameworks with Open Metal Sites : Strong Dependence of the Binding Strength on Metal Ions 2008;2:15268–9.

[74] Dincă M, Long JR. High-enthalpy hydrogen adsorption in cation-exchanged variants of the microporous metal-organic framework Mn3[(Mn4CI) 3(BTT)8(CH3OH)10]2. J Am Chem Soc 2007;129:11172–6.

[75] Zhang X, Lin RB, Wang J, Wang B, Liang B, Yildirim T, et al. Optimization of the Pore Structures of MOFs for Record High Hydrogen Volumetric Working Capacity. Adv Mater 2020;32:1–6.

[76] Blanita G, Coldea I, Misan I, Lupu D. Hydrogen cryo-adsorption by hexagonal prism monoliths of MIL-101. Int J Hydrogen Energy 2014;39:17040–6.

[77] Niaz S, Manzoor T, Pandith AH. Hydrogen storage: Materials, methods and perspectives. Renew Sustain Energy Rev 2015;50:457–69.

[78] Wang H, Gao Q, Hu J. High hydrogen storage capacity of porous carbons prepared by using activated carbon. J Am Chem Soc 2009;131:7016–22.

[79] Masika E, Mokaya R. Preparation of ultrahigh surface area porous carbons templated using zeolite 13X for enhanced hydrogen storage. Prog Nat Sci Mater Int 2013;23:308–16.

[80] Chen P, Wu X, Lin J, Tan KL. High H2 uptake by alkali-doped carbon nanotubes under ambient pressure and moderate temperatures. Science (80-) 1999;285:91–3.

[81] Xia K, Hu J, Jiang J. Enhanced room-temperature hydrogen storage in super-activated carbons: The role of porosity development by activation. Appl Surf Sci 2014;315:261–7.

[82] Liu C, Chen Y, Wu CZ, Xu ST, Cheng HM. Hydrogen storage in carbon nanotubes revisited. Carbon N Y 2010;48:452–5.

[83] Moshoeshoe M, Silas Nadiye-Tabbiruka M, Obuseng V. A Review of the Chemistry, Structure, Properties and Applications of Zeolites. Am J Mater Sci

2017;2017:196–221.

[84] TOP S, VAPUR H. TürkTermikSantrallerindeİki Farkli Uçucu Kül KullanarakAlkali Yakma MetoduylaZeolitSentezi. Bilim Madencilik Derg 2020:7–14.

[85] Langmi HW, Book D, Walton A, Johnson SR, Al-Mamouri MM, Speight JD, et al. Hydrogen storage in ion-exchanged zeolites. J Alloys Compd 2005;404–406:637–42.

[86] Li Y, Yang RT. Gas adsorption and storage in metal-organic framework MOF-177. Langmuir 2007;23:12937–44.

[87] Georgiev PA, Drenchev N, Hadjiivanov KI, Ollivier J, Unruh T, Albinati A, et al. H2 Adsorption on Cu(I)-SSZ-13. Microporous Mesoporous Mater 2005;122:540–8.

[88] Weitkamp J, Fritz M, Ernst S. ZEOLITES AS MEDIA FOR HYDROGEN STORAGE*. Int J Hydrogen Energy 1995;20:967–70.

[89] Jiang J, Yun Y, Zou X, Luis Jorda J, Corma A. ITQ-54: a multi-dimensional extra-large pore zeolite with 20*14*12-ring channels. Chem Sci 2015;6:480.

[90] Kayiran SB, Darkrim FL. Synthesis and ionic exchanges of zeolites for gas adsorption 2002:100–4.

[91] Langmi HW, Walton A, Al-Mamouri MM, Johnson SR, Book D, Speight JD, et al. Hydrogen adsorption in zeolites A, X, Y and RHO. J. Alloys Compd., vol. 356–357, 2003, p. 710–5.

[92] Takagi H, Hatori H, Soneda Y, Yoshizawa N, Yamada Y. Adsorptive hydrogen storage in carbon and porous materials 2004;108:143–7.

[93] M M, Zholobenko VL, Al-ghefaili KM, Thompson NE, Dewing J, Dwyer J. Brnsted Acid Sites in Zeolites. J Chem Sociaty Faraday Trans 1994;90:1047–54.

[94] Zecchina A, Bordiga S, Vitillo JG, Ricchiardi G, Lamberti C, Spoto G, et al. Liquid Hydrogen in Protonic Chabazite 2005:6361–6.

[95] Kubo M, Kamimura Y, Itabashi K, Okubo T. Cryogenic hydrogen adsorption onto H-, Li-, Na-exchanged zeolites with various Si/Al ratios. Adsorpt Sci Technol 2014;32:413–23.

[96] Sung HJ, Ji WY, Kim HK, Chang JS. Low temperature adsorption of hydrogen on nanoporous materials. Bull Korean Chem Soc 2005;26:1075–8.

[97] Du X, Wu E. Physisorption of Hydrogen in A, X and ZSM-5 Types of Zeolites at Moderately High Pressures. Chinese J Chem Phys 2006;19:457–62.

[98] Otero Areán C, Nachtigallová D, Nachtigall P, Garrone E, Rodríguez Delgado M. Thermodynamics of reversible gas adsorption on alkali-metal exchanged zeolites - The interplay of infrared spectroscopy and theoretical calculations. Phys Chem Chem Phys 2007;9:1421–37.

[99] Tun H, Chen CC. Isosteric heat of adsorption from thermodynamic Langmuir isotherm. Adsorption 2021;27:979–89.

[100] Builes S, Sandler SI, Xiong R. Isosteric heats of gas and liquid adsorption. Langmuir 2013;29:10416–22.

[101] Nachtigall P, Garrone E, Turnes Palomino G, Rodríguez Delgado M, Nachtigallová D, Otero Areán C. FTIR spectroscopic and computational studies on hydrogen adsorption on the zeolite Li-FER. Phys Chem Chem Phys 2006;8:2286–92.

[102] Otero Areán C, Rodriguez Delgado M, Turnes Palomino G, Rubio MT, Tsyganenko NM, Tsyganenko AA, et al. Thermodynamic studies on hydrogen adsorption on the zeolites Na-ZSM-5 and K-ZSM-5. Microporous Mesoporous Mater 2005;80:247–52.

[103] Palomino GT, Carayol MRL, Areán CO. Hydrogen adsorption on magnesium-exchanged zeolites. J Mater Chem 2006;16:2884–5.

[104] Turnes Palomino G, Llop Carayol MR, Otero Areán C. Thermodynamics of hydrogen adsorption on the zeolite Ca-Y. Catal Today 2008;138:249–52.

[105] Jhung SH, Yoon JW, Lee JS, Chang JS. Low-temperature adsorption/storage

of hydrogen on FAU, MFI, and MOR zeolites with various Si/Al ratios: Effect of electrostatic fields and pore structures. Chem - A Eur J 2007;13:6502–7.

[106] Georgiev PA, Albinati A, Eckert J. Room temperature isosteric heat of dihydrogen adsorption on Cu(I) cations in zeolite ZSM-5. Chem Phys Lett 2007;449:182–5.

[107] Ipek B, Pollock RA, Brown CM, Uner D, Lobo RF. H2 Adsorption on Cu(I)-SSZ-13. J Phys Chem C 2018;122:540–8.

[108] Ipek B, Altiparmak I. Remarkable isosteric heat of hydrogen adsorption on Cu(I)-exchanged SSZ-39. Int J Hydrogen Energy 2020;45:34972–82.

[109] Kozyra P, Piskorz W. A comparative computational study on hydrogen adsorption on the Ag+, Cu+, Mg2+, Cd2+, and Zn2+ cationic sites in zeolites. Phys Chem Chem Phys 2016;18:12592–603.

[110] Kazansky VB. Localization of bivalent transition metal ions in high-silica zeolites with the very broad range of Si/Al ratios in the framework probed by low-temperature H2 adsorption. J Catal 2003;216:192–202.

[111] Kazansky VB, Serykh AI, Bell AT. Siting of Co2+ ions in cobalt-modied high-silica zeolites probed by low-temperature molecular hydrogen adsorption. Abstr Pap Am Chem Soc 2002;223:C12–C12.

[112] Bordiga S, Garrone E, Lamberti C, Zecchina A, Areán CO, Kazansky VB, et al. Comparative IR-spectroscopic study of low-temperature H2 and CO adsorption on Na zeolites. J Chem Soc Faraday Trans 1994;90:3365–72.

[113] Kazansky VB, Borovkov VY, Zhidomirov GM. Nuclear magnetic resonance studies of complexes formed by adsorbed molecules and tetrahedral Co2+ and Ni2+ ions. J Catal 1975;39:205–12.

[114] Georgiev PA, Albinati A. Nonclassical hydrides of Ni + in ZSM-5 zeolite structures: A hybrid DFT study. Chem Phys Lett 2012;545:66–70.

[115] Raj MC, Prasanth KP, Dangi GP, Bajaj HC. Hydrogen sorption in transition metal exchanged zeolite Y: Volumetric measurements and simulation study.

J Porous Mater 2012;19:657–66.

[116] Kim CW, Jung KJ, Heo NH, Seff K. Crystal Structures of Vacuum-Dehydrated Ni 2 + -Exchanged Zeolite Y (FAU , Si / Al) 1 . 69) Containing Three-Coordinate Ni 2 + , Ni 8 O 4 · x H 2 O 8 + , x e 4 , Clusters with Near Cubic Ni 4 O 4 Cores , and H + 2009:5164–81.

[117] Olson DH. Crystal structure of the zeolite nickel faujasite. J Phys Chem 1968;72:4366–73.

[118] Gallezot P, Imelik B. Location of Nickel Ions in Y Zeolites. 1. Influence of Thermal Treatment. J Phys Chem 1972;295:652–6.

[119] Seo SM, Kim HS, Chung DY, Suh JM, Lim WT. The Effect of Co2+-ion exchange time into zeolite y (FAU, Si/Al = 1.56): Their Single-Crystal Structures. Bull Korean Chem Soc 2014;35:243–9.

[120] MAHER PK, HUNTER FD, SCHERZER J. Crystal Structures of Ultrastable Faujasites 1974:266–78.

[121] Chapellière Y, Daniel C, Tuel A, Farrusseng D, Schuurman Y. Kinetics of n-hexane cracking over mesoporous hy zeolites based on catalyst descriptors. Catalysts 2021;11.

[122] Vitillo JG, Ricchiardi G, Spoto G, Zecchina A. Theoretical maximal storage of hydrogen in zeolitic frameworks. Phys Chem Chem Phys 2005;7:3948–54.

[123] Database of Zeolite Structures n.d. http://www.iza-structure.org/databases/.

[124] Dědeček J, Kaucký D, Wichterlová B, Gonsiorová O. Co2+ ions as probes of Al distribution in the framework of zeolites. ZSM-5 study. Phys Chem Chem Phys 2002;4:5406–13.

[125] Dědeček J, Wichterlová B. Co2+ ion siting in pentasil-containing zeolites. I. Co2+ ion sites and their occupation in mordenite. A Vis-NIR diffuse reflectance spectroscopy study. J Phys Chem B 1999;103:1462–76.

[126] Drozdová L, Prins R, Dědeček J, Sobalík Z, Wichterlová B. Bonding of Co ions in ZSM-5, ferrierite, and mordenite: An X-ray absorption, UV-Vis, and

IR study. J Phys Chem B 2002;106:2240–8.

[127] Dědeček J, Kaucký D, Wichterlová B. Al distribution in ZSM-5 zeolites: An experimental study. Chem Commun 2001:970–1.

[128] Dedecek J, Balgová V, Pashkova V, Klein P, Wichterlová B. Synthesis of ZSM-5 zeolites with defined distribution of Al atoms in the framework and multinuclear MAS NMR analysis of the control of Al distribution. Chem Mater 2012;24:3231–9.

[129] Rassy E. Development of methods to identify thermophysical properties of complex media 2019:252.

[130] McCusker LB, Liebau F, Englehardt G. Nomenclature of structural and compositional characteristics of ordered microporous and mesoporous materials with inorganic hosts (IUPAC recommendations 2001): Physical chemistry Division commision on colloid and surface chemistry including catalysis. Microporous Mesoporous Mater 2003;58:3–13.

[131] Gamliel DP, Cho HJ, Fan W, Valla JA. On the effectiveness of tailored mesoporous MFI zeolites for biomass catalytic fast pyrolysis. Appl Catal A Gen 2016;522:109–19.

[132] Jia X, Khan W, Wu Z, Choi J, Yip ACK. Modern synthesis strategies for hierarchical zeolites: Bottom-up versus top-down strategies. Adv Powder Technol 2019;30:467–84.

[133] Wu L, Degirmenci V, Magusin PCMM, Lousberg NJHGM, Hensen EJM. Mesoporous SSZ-13 zeolite prepared by a dual-template method with improved performance in the methanol-to-olefins reaction. J Catal 2013;298:27–40.

[134] Xue T, Liu H, Zhang Y, Wu H, Wu P, He M. Synthesis of ZSM-5 with hierarchical porosity: In-situ conversion of the mesoporous silica-alumina species to hierarchical zeolite. Microporous Mesoporous Mater 2017;242:190–9.

[135] Sasongko SB, Anggoro DD, Buchori L, Febrianto R, Siagian EAB. The effect of dealumination process on zeolite y acidity and morphology. AIP Conf Proc 2020;2197.

[136] Groen JC, Jansen JC, Moulijn JA, Pérez-Ramírez J. Optimal aluminum-assisted mesoporosity development in MFI zeolites by desilication. J Phys Chem B 2004;108:13062–5.

[137] Van Donk S, Janssen AH, Bitter JH, De Jong KP. Generation, characterization, and impact of mesopores in zeolite catalysts. Catal Rev - Sci Eng 2003;45:297–319.

[138] Kapteijn F, Marbán G, Rodriguez-Mirasol J, Moulijn JA. Kinetic analysis of the decomposition of nitrous oxide over ZSM-5 catalysts. J Catal 1997;167:256–65.

[139] Iliopoulou EF, Stefanidis SD, Kalogiannis KG, Delimitis A, Lappas AA, Triantafyllidis KS. Catalytic upgrading of biomass pyrolysis vapors using transition metal-modified ZSM-5 zeolite. Appl Catal B Environ 2012;127:281–90.

[140] Vafaeian Y, Haghighi M, Aghamohammadi S. Ultrasound assisted dispersion of different amount of Ni over ZSM-5 used as nanostructured catalyst for hydrogen production via CO2 reforming of methane. Energy Convers Manag 2013;76:1093–103.

[141] Conte M, Lopez-Sanchez JA, He Q, Morgan DJ, Ryabenkova Y, Bartley JK, et al. Modified zeolite ZSM-5 for the methanol to aromatics reaction. Catal Sci Technol 2012;2:105–12.

[142] Usman M, Wan Daud WMA, Abbas HF. Dry reforming of methane: Influence of process parameters - A review. Renew Sustain Energy Rev 2015;45:710–44.

[143] Negm NA, El Sheikh R, El-Farargy AF, Hefni HHH, Bekhit M. Treatment of industrial wastewater containing copper and cobalt ions using modified

chitosan. J Ind Eng Chem 2015;21:526–34.

[144] Bellmann A, Rautenberg C, Bentrup U, Brückner A. Determining the location of Co2+ in zeolites by UV-Vis diffuse reflection spectroscopy: A critical view. Catalysts 2020;10:1–11.

[145] Dědeček J, Sobalík Z, Wichterlová B. Siting and Distribution of Framework Aluminium Atoms in Silicon-Rich Zeolites and Impact on Catalysis. Catal Rev - Sci Eng 2012;54:135–223.

[146] Verberckmoes AA, Weckhuysen BM, Schoonheydt RA. Chemometric analysis of diffuse reflectance spectra of CoA zeolites: Spectroscopic fingerprinting of Co2+-sites. Stud Surf Sci Catal 1997;105:623–30.

[147] Woo JDH and SI. UV/VIS Diffuse Reflectance Spectroscopic (DRS) Study of Cobalt-Containing Y Zeolites Dehydrated at Elevated Temperatures. Korean J Chem 1989;8:2430–2.

[148] Hutta PJ, Lunsford JH. Spectroscopic evidence for the location of Co2+ ions in zeolite Y upon dehydration. J Chem Phys 1977;66:4716–7.

[149] Dědeček J, Kaucký D, Wichterlová B. Co2+ ion siting in pentasil-containing zeolites, part 3. Co2+ ion sites and their occupation in ZSM-5: A VIS diffuse reflectance spectroscopy study. Microporous Mesoporous Mater 2000;35–36:483–94.

[150] Góra-Marek K, Glanowska A, Datka J. Quantitative IR studies of the concentration of different nickel sites in NiZSM-5 zeolites. Microporous Mesoporous Mater 2012;158:162–9.

[151] Ganjkhanlou Y, Groppo E, Bordiga S, Volkova MA, Berlier G. Incorporation of Ni into HZSM-5 zeolites: Effects of zeolite morphology and incorporation procedure. Microporous Mesoporous Mater 2016;229:76–82.

[152] Góra-Marek K, Gil B, Śliwa M, Datka J. An IR spectroscopy study of Co sites in zeolites CoZSM-5. Appl Catal A Gen 2007;330:33–42.

[153] Lepetit C, Che M. Discussion on the coordination of Ni2+ ions to lattice

oxygens in calcined Faujasite-type zeolites followed by diffuse reflectance spectroscopy. J Phys Chem 1996;100:3137–43.

[154] Serykh AI, Amiridis MD. Formation and thermal stability of Ni + cationic sites in Ni-ZSM-5. J Phys Chem C 2007;111:17020–4.

[155] Serykh AI, Sokolova NA, Borovkov VY, Kazansky VB. Study of the state of nickel in ion-exchanged NiNaY zeolite by IR spectroscopy using molecular hydrogen adsorbed at low temperatures. Kinet Catal 2000;41:688–95.

[156] Sun T, Trudeau ML, Ying JY. The nature of cobalt species in Co-ZSM-5 NO emission control catalysts. J Phys Chem 1996;100:13662–6.

[157] Meng L, Mezari B, Goesten MG, Wannapakdee W, Pestman R, Gao L, et al. Direct synthesis of hierarchical ZSM-5 zeolite using cetyltrimethylammonium as structure directing agent for methanol-to-hydrocarbons conversion. Catal Sci Technol 2017;7:4520–33.

[158] Kustova MY, Rasmussen SB, Kustov AL, Christensen CH. Direct NO decomposition over conventional and mesoporous Cu-ZSM-5 and Cu-ZSM-11 catalysts: Improved performance with hierarchical zeolites. Appl Catal B Environ 2006;67:60–7.

[159] Groen JC, Peffer LAA, Moulijn JA, Pérez-Ramírez J. Mesoporosity development in ZSM-5 zeolite upon optimized desilication conditions in alkaline medium. Colloids Surfaces A Physicochem Eng Asp 2004;241:53–8.

[160] Schmidt F, Lohe MR, Büchner B, Giordanino F, Bonino F, Kaskel S. Improved catalytic performance of hierarchical ZSM-5 synthesized by desilication with surfactants. Microporous Mesoporous Mater 2013;165:148–57.

[161] Harkins WD, Jura G. Surfaces of Solids. XIII. A Vapor Adsorption Method for the Determination of the Area of a Solid without the Assumption of a Molecular Area, and the Areas Occupied by Nitrogen and Other Molecules on the Surface of a Solid. J Am Chem Soc 1944;66:1366–73.

[162] Abdellatief M, Najdawi M Al, Momani Y, Aljamal B, Abbadi A, Harfouche M, et al. Operational status of the X-ray powder diffraction beamline at the SESAME synchrotron. J Synchrotron Radiat 2022;29:532–9.

[163] Toby BH, Von Dreele RB. GSAS-II: The genesis of a modern open-source all purpose crystallography software package. J Appl Crystallogr 2013;46:544–9. https://doi.org/10.1107/S0021889813003531.

[164] Giannozzi P, Baroni S, Bonini N, Calandra M, Car R, Cavazzoni C, et al. QUANTUM ESPRESSO: A modular and open-source software project for quantum simulations of materials. J Phys Condens Matter 2009;21.

[165] Voogd P, Scholten JJF, van Bekkum H. Use of the t-plot-De Boer method in pore volume determinations of ZSM-5 type zeolites. Colloids and Surfaces 1991;55:163–71.

[166] Sarohan N, Ozbek MO, Kaya Y, Abdellatief M, Ipek B. Hydrogen adsorption on Co 2+ - and Ni 2+ - exchanged -US-Y and -ZSM-5 . A combined sorption , DR UV-Vis , synchrotron XRD and DFT study. Int J Hydrogen Energy 2022.

[167] Prasanth KP, Pillai RS, Bajaj HC, Jasra R V., Chung HD, Kim TH, et al. Adsorption of hydrogen in nickel and rhodium exchanged zeolite X. Int J Hydrogen Energy 2008;33:735–45.

[168] Suzuki M, Tsutsumi K, Takahashi H. Characterization and catalytic activity of nickel-zeolite catalysts. II. Effects of hydroxyl groups on reduction of nickel ions in mordenites. Zeolites 1982;2:87–93.

[169] Otero Areán C, Turnes Palomino G, Llop Carayol MR. Variable temperature FT-IR studies on hydrogen adsorption on the zeolite (Mg,Na)-Y. Appl Surf Sci 2007;253:5701–4.

[170] Gygi D, Bloch ED, Mason JA, Hudson MR, Gonzalez MI, Siegelman RL, et al. Hydrogen Storage in the Expanded Pore Metal-Organic Frameworks M2(dobpdc) (M = Mg, Mn, Fe, Co, Ni, Zn). Chem Mater 2016;28:1128–38.

[171] Zhou W, Wu H, Yildirim T. Enhanced H2 adsorption in isostructural metal-

organic frameworks with open metal sites: Strong dependence of the binding strength on metal ions. J Am Chem Soc 2008;130:15268–9.

[172] Villajos JA, Orcajo G, Martos C, Botas JÁ, Villacañas J, Calleja G. Co/Ni mixed-metal sited MOF-74 material as hydrogen adsorbent. Int J Hydrogen Energy 2015;40:5346–52.

[173] Yang SJ, Im JH, Nishihara H, Jung H, Lee K, Kyotani T, et al. General relationship between hydrogen adsorption capacities at 77 and 298 K and pore characteristics of the porous adsorbents. J Phys Chem C 2012;116:10529–40.

[174] Peedikakkal AMP, Aljund IH. Upgrading the hydrogen storage of mof-5 by post-synthetic exchange with divalent metal ions. Appl Sci 2021;11.

[175] Sazama P, Tabor E, Klein P, Wichterlova B, Sklenak S, Mokrzycki L, et al. Al-rich beta zeolites. Distribution of Al atoms in the framework and related protonic and metal-ion species. J Catal 2016;333:102–14.

[176] Klier K, Kellerman R, Hutta PJ. Spectra of synthetic zeolites containing transition metal ions. V.* Π complexes of olefins and acetylene with Co(II)A molecular sieve. J Chem Phys 1974;61:4224–34.

[177] Tanaka M, Kuroda Y, Iwamoto M. Effect of pore size and nickel content of Ni-MCM-41 on catalytic activity for ethene dimerization and local structures of nickel ions. J Phys Chem C 2012;116:22649–51.

[178] Luo GG, Wang YH, Wang JH, Wu JH, Wu RB. A square-planar nickel dithiolate complex as an efficient molecular catalyst for the electro- and photoreduction of protons. Chem Commun 2017;53:7007–10.

[179] Rashad MM, Hassan AM, Nassar AM, Ibrahim NM, Mourtada A. A new nano-structured Ni(II) Schiff base complex: synthesis, characterization, optical band gaps, and biological activity. Appl Phys A Mater Sci Process 2014;117:877–90.

[180] Galoisy L, Calas G. Structural environment of nickel in silicate glass/melt systems: Part 1. Spectroscopic determination of coordination states. Geochim

Cosmochim Acta 1993;57:3613–26.

[181] Seo SM, Ko SO, Lim WT. Structural comparison of partially dehydrated partially Co2+-exchanged zeolites X (FAU, Si/Al = 1.40) and Y (FAU, Si/Al = 1.70). J Porous Mater 2016;23:95–105.

[182] Kang L, Deng W, Han K, Zhang T, Liu Z. A DFT study of adsorption hydrogen on the Li-FAU zeolite. Int J Hydrogen Energy 2008;33:105–10.

[183] Ozturk Z. Hydrogen storage on lithium modified silica based CHAbazite type zeolite, A computational study. Int J Hydrogen Energy 2018;43:22365–76.

[184] Areán CO, Palomino GT, Carayol MRL, Pulido A, Rubeš M, Bludský O, et al. Hydrogen adsorption on the zeolite Ca-A: DFT and FT-IR investigation. Chem Phys Lett 2009;477:139–43.

[185] Yuksel N, Kose A, Fellah MF. A Density Functional Theory study of molecular hydrogen adsorption on Mg site in OFF type zeolite cluster. Int J Hydrogen Energy 2020;45:34983–92.

[186] Torres FJ, Civalleri B, Terentyev A, Ugliengo P, Pisani C. Theoretical study of molecular hydrogen adsorption in Mg-exchanged chabazite. J Phys Chem C 2007;111:1871–3.

[187] Zaragoza IP, Pacheco-Sánchez JH, Echevarria-Chan I, Bravo-Ortega A. DFT study of interaction between a hydrogen molecule and AgY-zeolite. Rev Mex Física 2014;60:460–5.

[188] Shubin AA, Zhidomirov GM, Kazansky VB, Van Santen RA. DFT cluster modeling of molecular and dissociative hydrogen adsorption on Zn2+ ions with distant placing of aluminum in the framework of high-silica zeolites. Catal Letters 2003;90:137–42.

[189] Kozyra P, Piskorz W. A comparative computational study on hydrogen adsorption on the Ag+, Cu+, Mg2+, Cd2+, and Zn2+ cationic sites in zeolites. Phys Chem Chem Phys 2016;18:12592–603.

[190] Georgiev PA, Drenchev N, Hadjiivanov KI, Ollivier J, Unruh T, Albinati A.

Dynamics of bound states of dihydrogen at Cu(I) and Cu(II) species coordinated near one and two zeolite framework aluminium atoms: A combined sorption, INS, IR and DFT study. Int J Hydrogen Energy 2021;46:26897–914.

[191] Sklenak S, Dědeček J, Li C, Wichterlová B, Gábová V, Sierka M, et al. Aluminium siting in the ZSM-5 framework by combination of high resolution 27Al NMR and DFT/MM calculations. Phys Chem Chem Phys 2009;11:1237–47.

[192] Kubas GJ. Fundamentals of H 2 Binding and Reactivity on Transition Metals Underlying Hydrogenase Function and H 2 Production and Storage 2007:4152–205.

[193] Ozbek MO, Ipek B. A Theoretical Investigation of Cu+, Ni2+ and Co2+-exchanged Zeolites for Hydrogen Storage. ChemPhysChem 2022.

APPENDICES

A. H_2/M^{2+} Calculation

Ni^{2+}-US-Y Sample Calculation

Si/Al	5
Ni/Al	0.13
SiO_2 Molecular Weight	60.1
AlO_2 Molecular Weight	59
Ni Molecular Weight	58.7

$$\frac{g_{zeolite}}{mol\ Al} = \frac{\text{Si}}{\text{Al}} * SiO_2 \text{ Molecular Weight} + AlO_2 \text{ Molecular Weight} + \frac{\text{Ni}}{\text{Al}} * \text{Ni Molecular Weight} = 367\ \frac{g}{mol\ Al}$$

$$\frac{mol\ Al}{g_{zeolite}} = 0.0027$$

$$\frac{mol\ Ni^{2+}}{g\ zeolite} = \frac{mol\ Al}{g_{zeolite}} * \frac{mol\ Ni^{2+}}{mol\ Al} = 0.00035$$

$$\frac{mol\ H_2}{mol\ Ni^{2+}} = \frac{mol\ H_2}{g\ zeolite} * \frac{g\ zeolite}{mol\ Ni^{2+}}$$

Table A1. H_2/Ni^{2+} Results of Ni^{2+}-US-Y up to 10 bar

Pressure(bar)	**Adsorbed amount (mol H_2/g zeolite)**	$\frac{mol\ H_2}{mol\ Ni^{2+}}$
0.00	0.00000	0.00
0.66	0.00004	0.10
1.27	0.00006	0.16
1.80	0.00008	0.23
2.40	0.00012	0.33
2.87	0.00014	0.39
3.36	0.00016	0.46
3.85	0.00018	0.51
4.35	0.00020	0.57
4.84	0.00023	0.64
5.34	0.00025	0.72
5.90	0.00027	0.77
6.42	0.00030	0.85
6.89	0.00033	0.93
7.36	0.00035	1.00
7.84	0.00037	1.05
8.33	0.00041	1.15
8.82	0.00043	1.21
9.32	0.00046	1.30
9.82	0.00048	1.36
10.33	0.00052	1.46

B. Hydrogen Uptake Isotherms

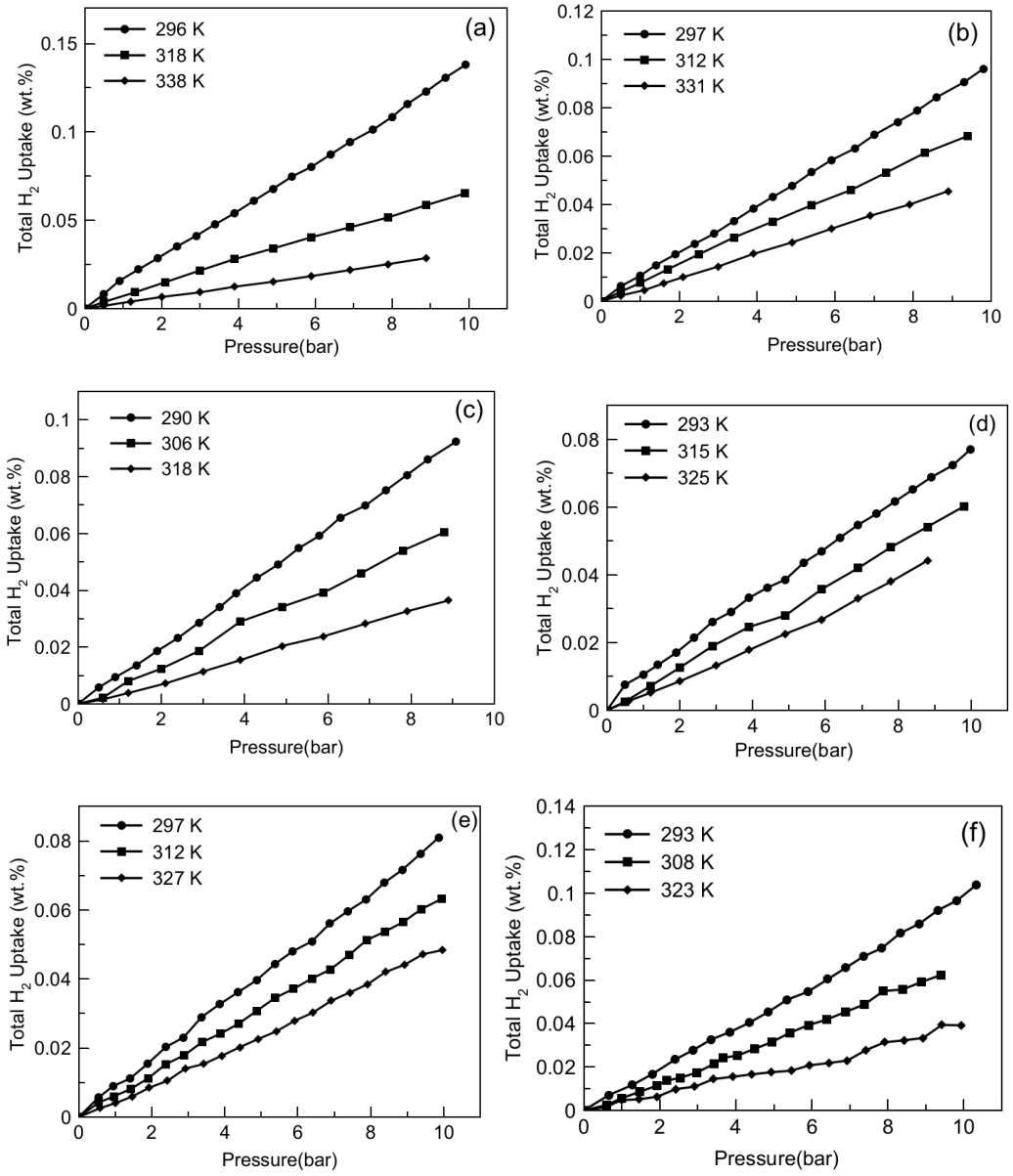

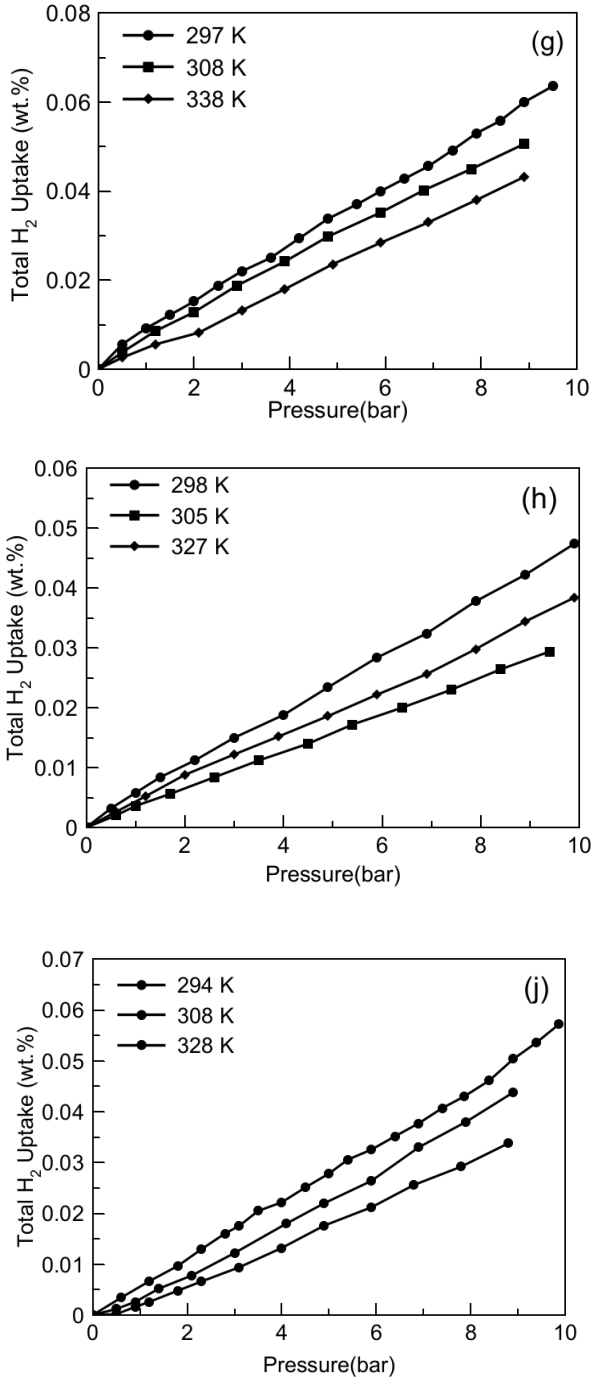

Figure B.1 Hydrogen adsorption isotherms at different temperatures for samples a) Meso-Ni^{2+}-ZSM-5 b) Meso-Co^{2+}-ZSM-5 c) Micro-Ni^{2+}-ZSM-5 d) Micro-Co^{2+}-ZSM-5, e) Co^{2+}-US-Y, f) Ni^{2+}-US-Y g) NH_4^+-ZSM-5(III)-DES h) NH_4^+-ZSM-5(III) j) NH_4^+-US-Y

Micro-Ni^{2+}-ZSM-5 Isotherm Fittings and Isosteric Heat Results

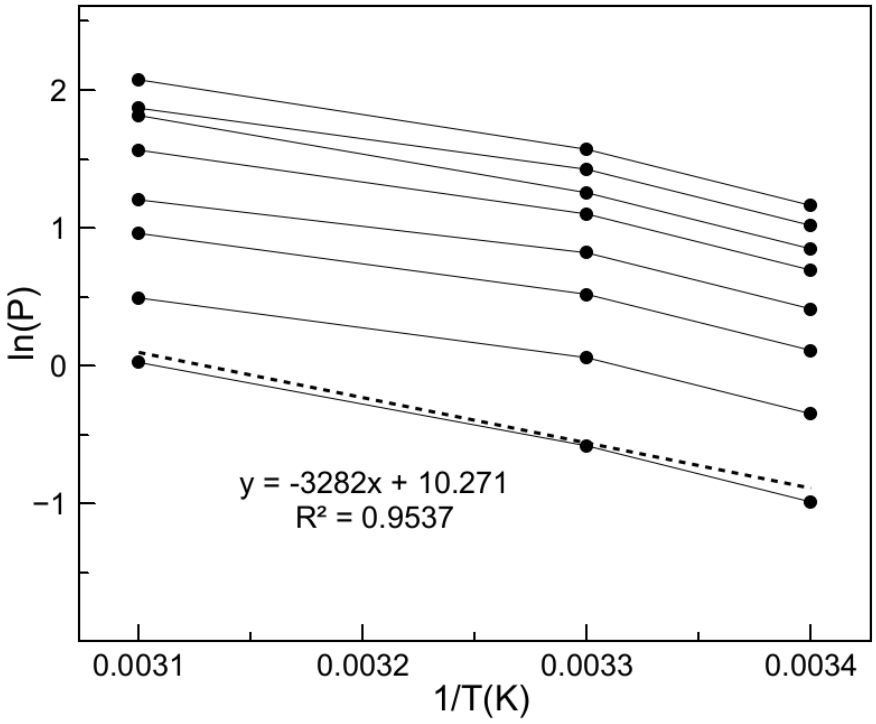

Figure B2. Adsorption isosteric method- Van't Hoff plots of Micro-Ni^{2+}-ZSM-5

Table B1. Data used to obtain isosteric heat of adsorption of Micro-Ni^{2+}-ZSM-5 between the temperatures 290 K and 318 K.

Adsorbed Amount(μmol)	lnP_{290K}	lnP_{306K}	lnP_{318K}	-Qst(kJ/mol)	R^2
19	-1	-0.6	0.02	27.29	0.9537
36	-0.3	0.06	0.49	22.88	0.9851
57	0.11	0.52	0.96	23.09	0.9837
77	0.41	0.82	1.20	21.62	0.9923
102	0.69	1.10	1.56	23.65	0.98
119	0.85	1.25	1.81	26.14	0.9622
141	1.02	1.42	1.87	23.15	0.9833
163	1.16	1.57	2.07	24.72	0.9726

C. DR UV–Vis spectra Results

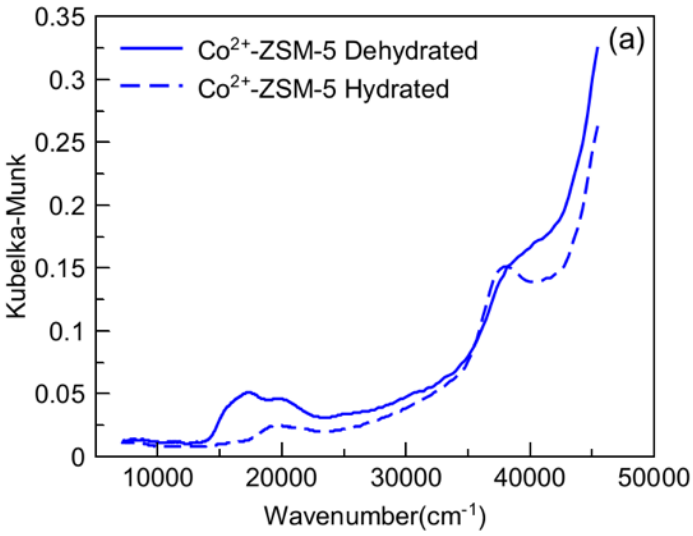

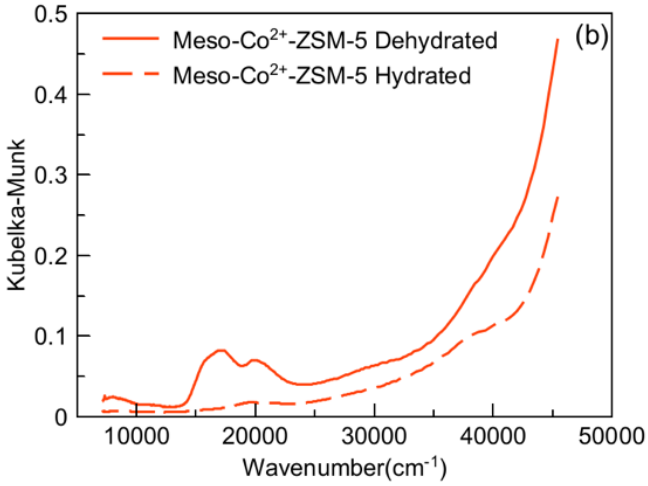

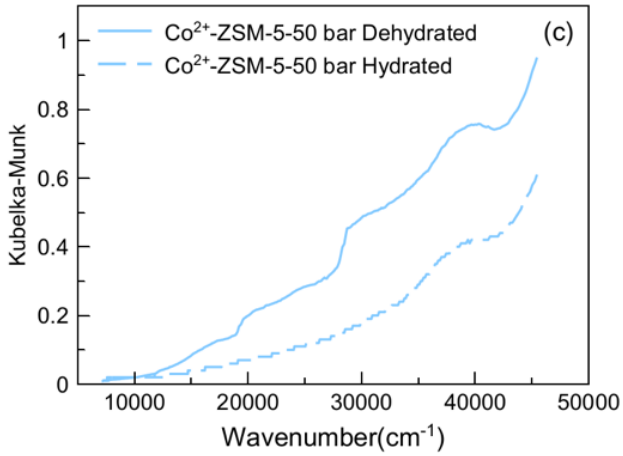
Co2+-ZSM-5-50 bar Dehydrated
Co2+-ZSM-5-50 bar Hydrated
(c)
Kubelka-Munk
Wavenumber(cm-1)

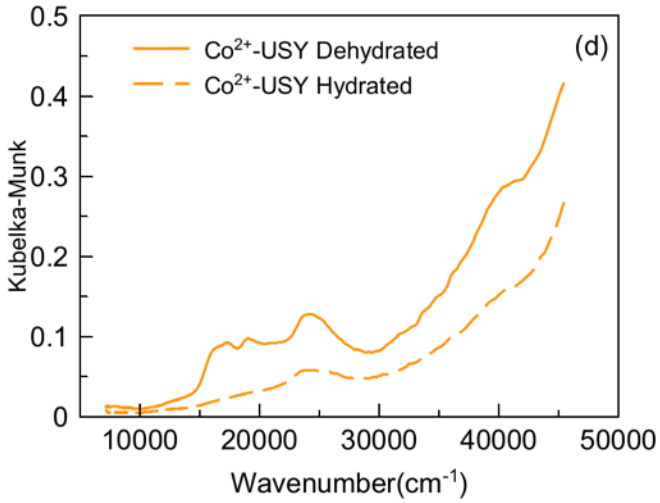
Co2+-USY Dehydrated
Co2+-USY Hydrated
(d)
Kubelka-Munk
Wavenumber(cm-1)

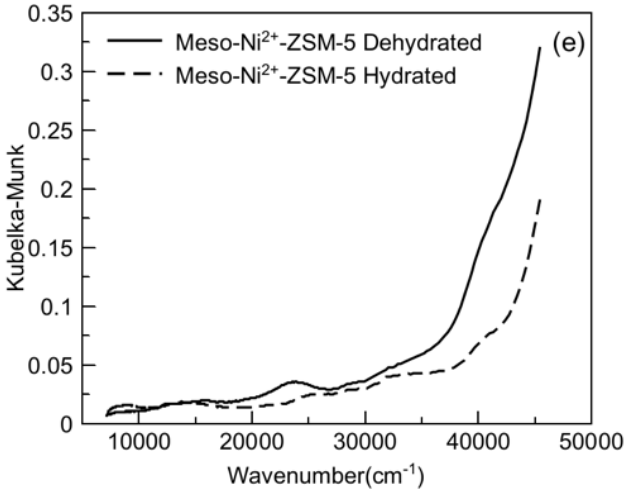
Meso-Ni2+-ZSM-5 Dehydrated
Meso-Ni2+-ZSM-5 Hydrated
(e)
Kubelka-Munk
Wavenumber(cm-1)

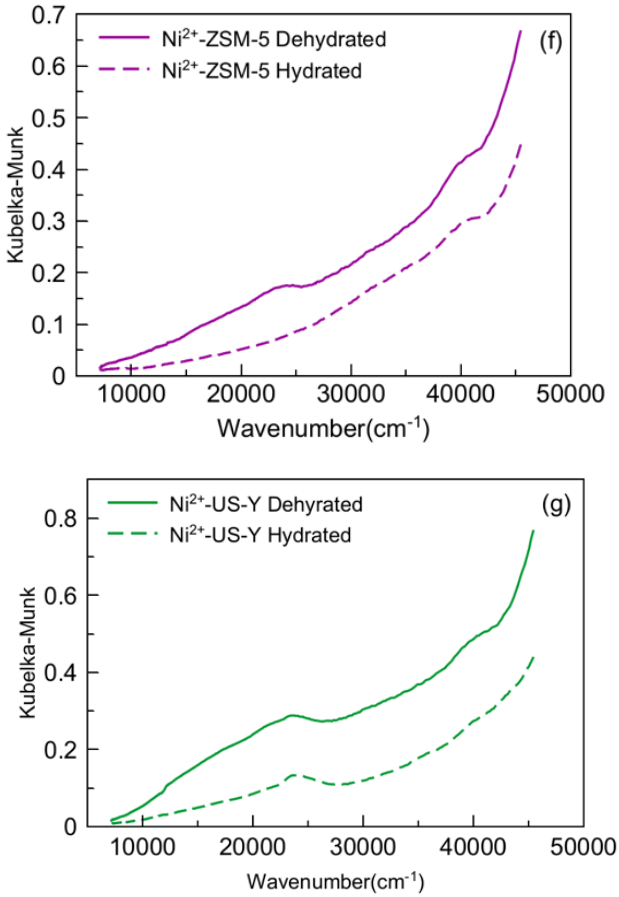

Figure C.1 DR UV–Vis spectra of a) Micro-Co^{2+}-ZSM-5 b) Meso-Co^{2+}-ZSM-5 c) Meso-Na^{+},Co^{2+}-ZSM d) Co^{2+}-US-Y e) Meso-Ni^{2+}-ZSM-5 f) Micro-Ni^{2+}-ZSM-5 g) Ni^{2+}-US-Y

D. Synchrotron XRD Refinements

Table D1. Atomic Parameters from Rietveld refinement of Co-US-Y ($Co_5Al_{38.4}Si_{153.6}O_{384}$) data [SESAME, ID09 MS] (Cubic, $Fd\bar{3}m$, Goodness of fit parameters wR_p = 10.68% at 25°C, λ = 1.03365 Å, a = 24.3290(2) Å, V = 14400.3(4) $Å^3$. (Values in parentheses indicate one standard deviation in the prior digit.)

	x	y	z	Occupancy	U_{iso} ($Å^2$)	Multiplicity
Si	-0.0545(1)	0.1250(1)	0.0357(1)	0.834	0.0206	192
Al	-0.0545(1)	0.1250(1)	0.0357(1)	0.166	0.0206	192
O1	0.0000	-0.1068(2)	0.1068(2)	1	0.0148	96
O2	-0.0032(2)	-0.0032(2)	0.1402(3)	1	0.0313	96
O3	0.0751(2)	0.0751(2)	-0.0355(3)	1	0.0463	96
O4	0.0717(2)	0.0717(2)	0.3200(3)	1	0.0539	96
Co1	0.105(2)	0.105(2)	0.105(2)	0.058(3)	0.1984	32
Co2	0.139(3)	0.267(2)	0.483(2)	0.047(4)	0.2578	96
O5/H_2O	0.2500	0.2500	0.5000	0.60(4)	0.4681	16
O6/H_2O	0.099(2)	0.099(2)	0.498(1)	0.43(1)	0.8125	96

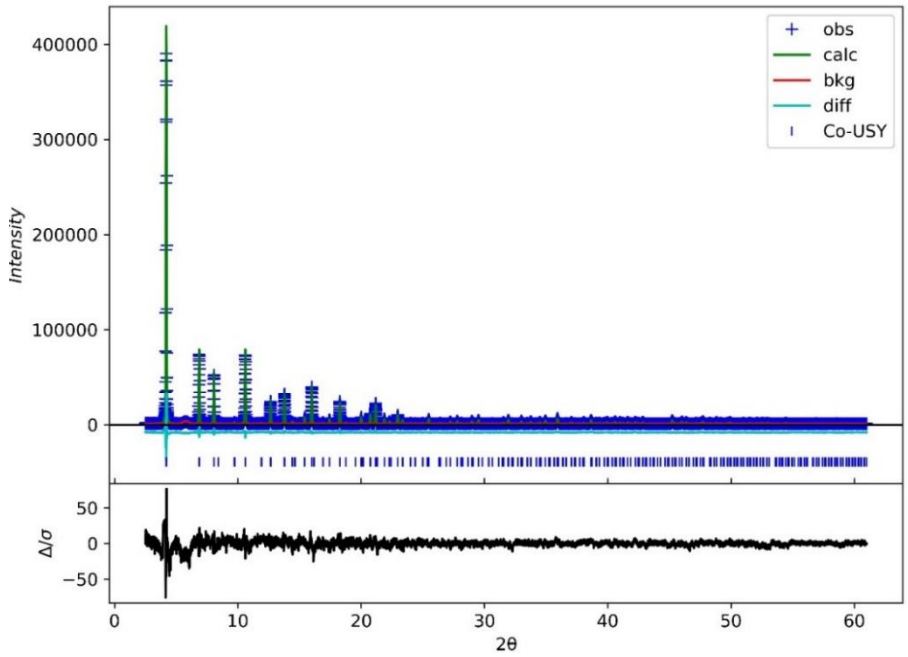

Figure D1. Synchrotron powder X-ray diffraction data (λ = 1.03365 Å) collected for Co-US-Y at 25 °C. Plus signs, green line, red line and blue line represent the experimental and calculated diffraction patterns, background and the difference between the experimental and calculated patterns. wR_p = 10.68%

Table D2. Atomic Parameters from Rietveld refinement of Ni-US-Y ($Ni_{4.2}Al_{32}Si_{160}O_{384}$) data [SESAME, ID09 MS] (Cubic, $Fd\bar{3}m$, Goodness of fit parameters wR_p = 11.59% at 25 °C, λ = 1.03365 Å, a = 24.3474(3) Å, V = 14433.0(5) $Å^3$. (Values in parentheses indicate one standard deviation in the prior digit.)

	x	y	z	Occupancy	U_{iso} ($Å^2$)	Multiplicity
Si	-0.0545(1)	0.1252(1)	0.0359(1)	0.834	0.0143	192
Al	-0.0545(1)	0.1252(1)	0.0359(1)	0.166	0.0143	192
O1	0.0000	-0.1065(2)	0.1065(2)	1	0.0087	96
O2	-0.0028(2)	-0.0028(2)	0.1399(2)	1	0.0122	96
O3	0.0759(2)	0.0759(2)	-0.0361(3)	1	0.0342	96
O4	0.0713(2)	0.0713(2)	0.3205(3)	1	0.0568	96
Ni1	0.111(3)	0.111(3)	0.111(3)	0.026(2)	0.0817	32
Ni2	0.011(7)	0.363(9)	0.011(7)	0.025(6)	0.2405	96
O5/H_2O	0.2500	0.2500	0.5000	0.59(3)	0.3358	16
O6/H_2O	0.094(1)	0.094(1)	0.495(1)	0.56(2)	0.4414	96

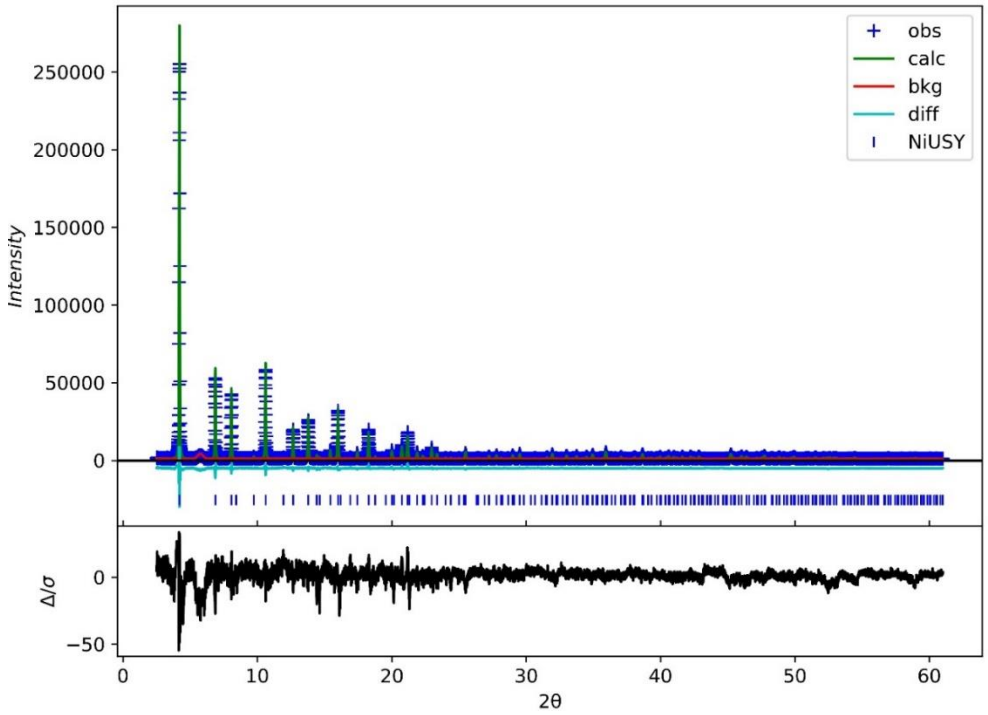

Figure D2. Synchrotron powder X-ray diffraction data (λ = 1.03365 Å) collected for Ni-US-Y at 25 °C. Plus signs, green line, red line and blue line represent the experimental and calculated diffraction patterns, background and the difference between the experimental and calculated patterns. wR_p = 11.59%

Table D3. Atomic Parameters from Rietveld refinement of Co-ZSM-5 ($Co_{1.57}Al_{4.36}Si_{91.64}O_{192}$) data [SESAME, ID09 MS] (Orthorhombic, *Pnma*, Goodness of fit parameters wR_p = 9.86% at 25 °C, λ = 1.03365 Å, a = 20.0182(4) Å, b = 19.8931(5) Å, c = 13.3790(3) Å, V = 5327.9(2) $Å^3$. (Values in parentheses indicate one standard deviation in the prior digit.)

	x	y	z	Occupancy	U_{iso} ($Å^2$)	Multiplicity
Si1	0.4196(9)	0.0555(8)	-0.321(1)	1	0.0229	8
Si2	0.305(1)	0.0295(7)	-0.170(1)	1	0.0532	8
Si3	0.2816(9)	0.0587(8)	0.033(1)	1	0.0637	8
Si4	0.1217(8)	0.0637(8)	0.029(1)	1	0.0156	8
Si5	0.074(1)	0.0381(8)	-0.185(1)	1	0.0730	8
Si6	0.195(1)	0.0626(9)	-0.334(1)	1	0.0559	8
Si7	0.423(1)	-0.1736(8)	-0.325(1)	1	0.0320	8
Si8	0.3125(9)	-0.1319(7)	-0.180(1)	1	0.0269	8
Si9	0.276(1)	-0.182(1)	0.036(2)	1	0.2089	8
Si10	0.116(1)	-0.1711(5)	0.035(1)	1	0.0488	8
Si11	0.0653(9)	-0.1219(8)	-0.179(1)	1	0.0451	8
Si12	0.1870(8)	-0.1704(6)	-0.308(1)	1	0.0278	8
O1	0.377(1)	0.044(2)	-0.219(2)	1	0.0491	8
O2	0.320(1)	0.073(1)	-0.071(1)	1	0.0010	8
O3	0.2013(8)	0.049(2)	0.034(2)	1	0.1093	8
O4	0.096(1)	0.077(1)	-0.084(1)	1	0.0136	8
O5	0.127(2)	0.059(3)	-0.270(3)	1	0.2963	8
O6	0.248(1)	0.057(2)	-0.243(2)	1	0.0119	8
O7	0.381(1)	-0.162(2)	-0.223(2)	1	0.1474	8
O8	0.310(2)	-0.153(2)	-0.064(2)	1	0.1402	8
O9	0.197(1)	-0.165(1)	0.038(2)	1	0.0474	8
O10	0.090(2)	-0.160(1)	-0.079(2)	1	0.0809	8
O11	0.118(1)	-0.142(2)	-0.265(2)	1	0.1030	8
O12	0.250(1)	-0.166(1)	-0.236(2)	1	0.0083	8
O13	0.299(2)	-0.0516(7)	-0.175(2)	1	0.0628	8
O14	0.081(1)	-0.0422(8)	-0.169(2)	1	0.0334	8
O15	0.412(2)	0.130(1)	-0.371(2)	1	0.0704	8
O16	0.405(2)	-0.001(1)	-0.404(2)	1	0.0453	8

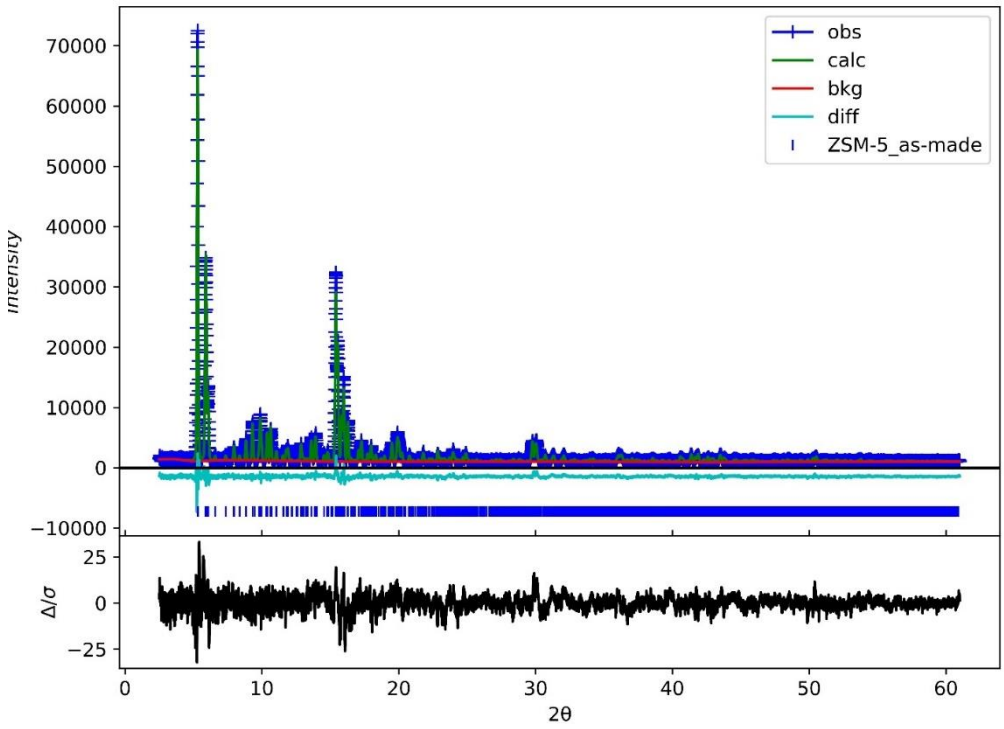

Figure D3. Synchrotron powder X-ray diffraction data (λ = 1.03365 Å) collected for Co-ZSM-5 at 25 °C. Plus signs, green line, red line and blue line represent the experimental and calculated diffraction patterns, background and the difference between the experimental and calculated patterns. wR_p = 9.86%

Table D4. Atomic Parameters from Rietveld refinement of Ni-ZSM-5 ($Ni_{1.31}Al_{4.36}Si_{91.64}O_{192}$) data [SESAME, ID09 MS] (Orthorhombic, *Pnma*, Goodness of fit parameters wR_p = 9.58% at 25 °C, λ = 1.03365 Å, a = 20.0417(5) Å, b = 19.8769(6) Å, c = 13.3810(4) Å, V = 5330.6(2) $Å^3$. (Values in parentheses indicate one standard deviation in the prior digit.)

	x	y	z	Occupancy	U_{iso} ($Å^2$)	Multiplicity
Si1	0.417(1)	0.054(1)	-0.314(2)	1	0.023	8
Si2	0.305(1)	0.023(8)	-0.164(2)	1	0.030	8
Si3	0.282(2)	0.064(1)	0.035(2)	1	0.094	8
Si4	0.122(2)	0.063(1)	0.034(2)	1	0.065	8
Si5	0.074(1)	0.0403(9)	-0.177(2)	1	0.045	8
Si6	0.195(1)	0.059(1)	-0.328(2)	1	0.057	8
Si7	0.425(1)	-0.175(1)	-0.318(2)	1	0.050	8
Si8	0.312(1)	-0.1385(8)	-0.165(1)	1	0.010	8
Si9	0.277(1)	-0.183(2)	0.053(2)	1	0.297	8
Si10	0.115(1)	-0.1692(9)	0.034(2)	1	0.028	8
Si11	0.065(1)	-0.1230(8)	-0.179(1)	1	0.009	8
Si12	0.191(1)	-0.171(1)	-0.307(2)	1	0.056	8
O1	0.376(2)	0.045(2)	-0.211(2)	1	0.049	8
O2	0.309(2)	0.078(1)	-0.077(2)	1	0.040	8
O3	0.202(2)	0.049(2)	0.037(3)	1	0.081	8
O4	0.096(2)	0.081(2)	-0.078(2)	1	0.057	8
O5	0.125(2)	0.049(3)	-0.270(3)	1	0.060	8
O6	0.250(2)	0.054(3)	-0.240(3)	1	0.104	8
O7	0.379(1)	-0.166(2)	-0.220(3)	1	0.012	8
O8	0.313(2)	-0.155(2)	-0.047(1)	1	0.040	8
O9	0.197(1)	-0.173(2)	0.043(2)	1	0.040	8
O10	0.088(2)	-0.165(2)	-0.081(2)	1	0.015	8
O11	0.123(1)	-0.154(2)	-0.249(3)	1	0.040	8
O12	0.257(2)	-0.141(2)	-0.253(3)	1	0.040	8
O13	0.297(2)	-0.0582(8)	-0.161(2)	1	0.031	8
O14	0.071(2)	-0.0415(8)	-0.179(3)	1	0.004	8
O15	0.410(2)	0.125(2)	-0.371(2)	1	0.040	8
O16	0.392(2)	0.004(2)	-0.402(2)	1	0.005	8

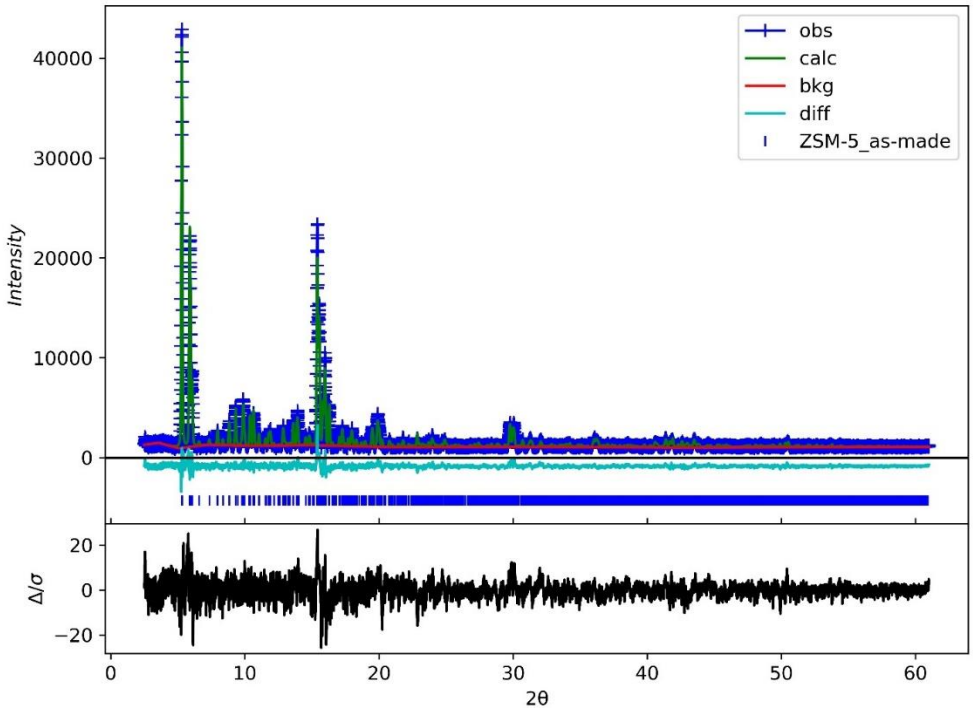

Figure D4. Synchrotron powder X-ray diffraction data (λ = 1.03365 Å) collected for Ni-ZSM-5 at 25 °C. Plus signs, green line, red line and blue line represent the experimental and calculated diffraction patterns, background and the difference between the experimental and calculated patterns. wR_p = 9.58%

Table D5. Atomic Parameters from Rietveld refinement of Meso-Co-ZSM-5 ($Co_{2.04}Al_{4.17}Si_{91.83}O_{192}$) data [SESAME, ID09 MS] (Orthorhombic, *Pnma*, Goodness of fit parameters wR_p = 10.47% at 25 °C, λ = 1.03365 Å, a = 20.1091(4) Å, b = 19.9669(5) Å, c = 13.4229(4) Å, V = 5389.5(2) $Å^3$. (Values in parentheses indicate one standard deviation in the prior digit.)

	x	y	z	Occupancy	U_{iso} ($Å^2$)	Multiplicity
Si1	0.418(1)	0.064(1)	-0.319(2)	1	0.0416	8
Si2	0.311(2)	0.0228(9)	-0.173(2)	1	0.0445	8
Si3	0.279(2)	0.054(1)	0.030(2)	1	0.1712	8
Si4	0.118(2)	0.053(2)	0.036(2)	1	0.1693	8
Si5	0.069(1)	0.034(1)	-0.182(2)	1	0.0405	8
Si6	0.196(2)	0.054(1)	-0.322(2)	1	0.0521	8
Si7	0.426(2)	-0.1704(6)	-0.328(2)	1	0.0337	8
Si8	0.314(1)	-0.1390(9)	-0.175(2)	1	0.0036	8
Si9	0.276(1)	-0.176(1)	0.040(2)	1	0.1833	8
Si10	0.119(1)	-0.1707(5)	0.036(2)	1	0.0275	8
Si11	0.072(2)	-0.129(1)	-0.176(2)	1	0.0371	8
Si12	0.193(1)	-0.1714(8)	-0.317(2)	1	0.0521	8
O1	0.381(2)	0.052(2)	-0.214(2)	1	0.0490	8
O2	0.307(2)	0.073(1)	-0.080(2)	1	0.0402	8
O3	0.199(2)	0.048(3)	0.037(3)	1	0.1645	8
O4	0.095(2)	0.064(2)	-0.078(2)	1	0.0437	8
O5	0.128(1)	0.055(2)	-0.258(3)	1	0.0437	8
O6	0.248(2)	0.055(2)	-0.229(3)	1	0.0944	8
O7	0.384(1)	-0.161(2)	-0.226(2)	1	0.0037	8
O8	0.315(2)	-0.147(2)	-0.056(2)	1	0.0016	8
O9	0.198(1)	-0.159(3)	0.025(5)	1	0.6159	8
O10	0.098(2)	-0.171(2)	-0.081(2)	1	0.1298	8
O11	0.127(1)	-0.155(2)	-0.255(2)	1	0.0480	8
O12	0.258(2)	-0.142(2)	-0.260(3)	1	0.0600	8
O13	0.302(3)	-0.0583(9)	-0.172(3)	1	0.1921	8
O14	0.070(2)	-0.048(1)	-0.182(3)	1	0.0211	8
O15	0.412(2)	0.140(1)	-0.363(2)	1	0.0011	8
O16	0.399(2)	0.019(2)	-0.415(3)	1	0.0303	8

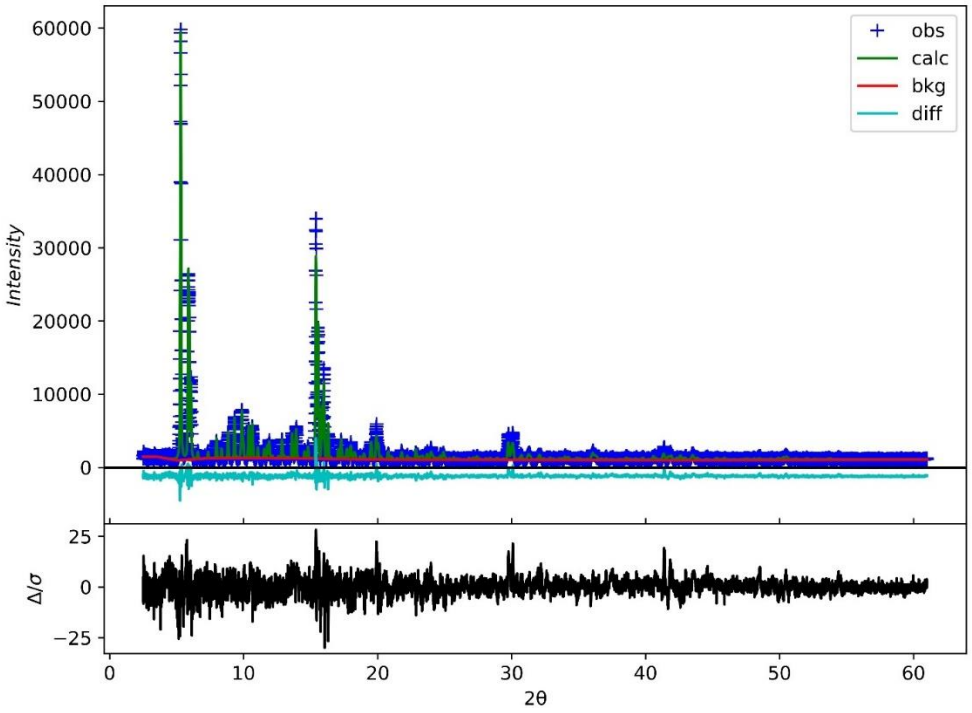

Figure D5. Synchrotron powder X-ray diffraction data (λ = 1.03365 Å) collected for Meso-Co-ZSM-5 at 25 °C. Plus signs, green line, red line and blue line represent the experimental and calculated diffraction patterns, background and the difference between the experimental and calculated patterns. wR_p = 10.47%

Table D6. Atomic Parameters from Rietveld refinement of Meso-Ni-ZSM-5 ($Ni_{1.83}Al_{4.17}Si_{91.83}O_{192}$) data [SESAME, ID09 MS] (Orthorhombic, *Pnma*, Goodness of fit parameters wR_p = 10.10% at 25 °C, λ = 1.03365 Å, a = 20.0331(5) Å, b = 19.8821(6) Å, c = 13.3769(5) Å, V = 5328.0(2) $Å^3$. (Values in parentheses indicate one standard deviation in the prior digit.)

	x	y	z	Occupancy	U_{iso} ($Å^2$)	Multiplicity
Si1	0.419(2)	0.055(2)	-0.312(2)	1	0.0328	8
Si2	0.308(2)	0.026(1)	-0.166(2)	1	0.0358	8
Si3	0.278(2)	0.055(2)	0.040(2)	1	0.1177	8
Si4	0.118(2)	0.056(2)	0.041(3)	1	0.0869	8
Si5	0.070(2)	0.038(1)	-0.177(3)	1	0.0353	8
Si6	0.192(2)	0.057(2)	-0.319(2)	1	0.0750	8
Si7	0.423(2)	-0.171(1)	-0.322(2)	1	0.0431	8
Si8	0.311(2)	-0.137(1)	-0.162(2)	1	0.0105	8
Si9	0.274(2)	-0.174(2)	0.058(3)	1	0.2642	8
Si10	0.114(2)	-0.173(1)	0.038(2)	1	0.0200	8
Si11	0.071(2)	-0.125(1)	-0.179(2)	1	0.0166	8
Si12	0.195(2)	-0.172(1)	-0.307(2)	1	0.0523	8
O1	0.380(2)	0.052(3)	-0.207(3)	1	0.0400	8
O2	0.309(3)	0.074(2)	-0.069(3)	1	0.0400	8
O3	0.198(2)	0.046(3)	0.040(4)	1	0.1503	8
O4	0.098(2)	0.071(2)	-0.075(3)	1	0.0456	8
O5	0.129(2)	0.068(3)	-0.245(4)	1	0.0815	8
O6	0.246(2)	0.057(3)	-0.228(4)	1	0.1153	8
O7	0.376(2)	-0.161(2)	-0.225(3)	1	0.0262	8
O8	0.312(3)	-0.152(2)	-0.043(2)	1	0.0296	8
O9	0.195(2)	-0.175(2)	0.034(3)	1	0.0884	8
O10	0.091(3)	-0.164(2)	-0.077(2)	1	0.0428	8
O11	0.124(2)	-0.149(2)	-0.262(3)	1	0.0008	8
O12	0.261(2)	-0.141(3)	-0.256(3)	1	0.0360	8
O13	0.305(3)	-0.055(1)	-0.160(3)	1	0.0421	8
O14	0.077(2)	-0.043(1)	-0.179(3)	1	0.0038	8
O15	0.413(3)	0.125(2)	-0.374(3)	1	0.0420	8
O16	0.399(4)	0.018(3)	-0.415(3)	1	0.0125	8

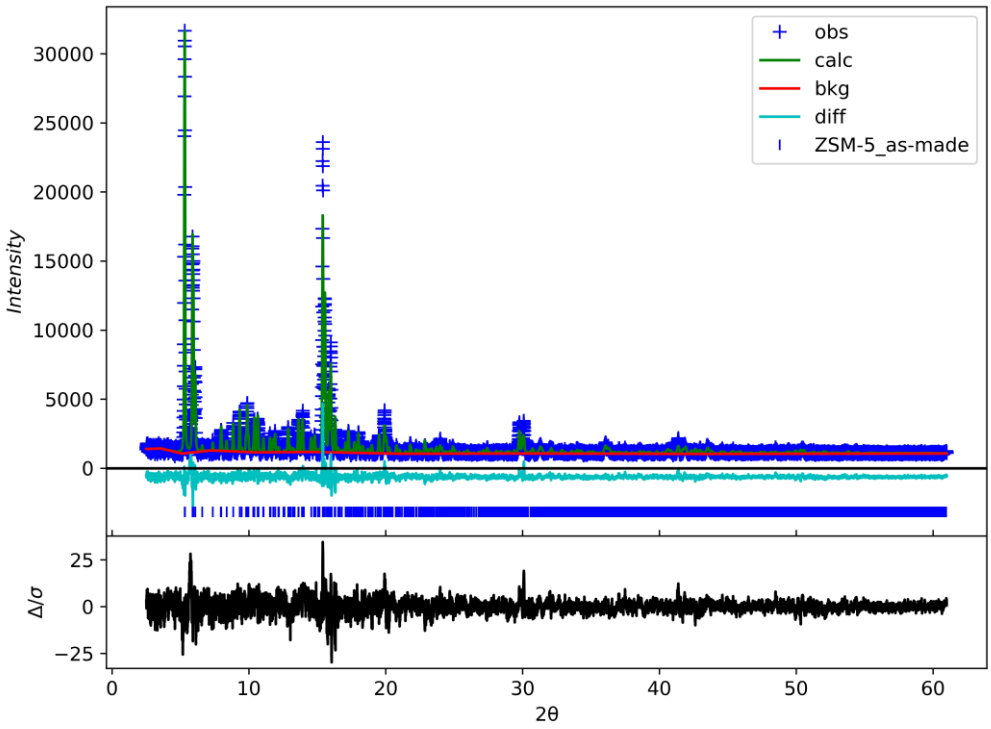

Figure D6. Synchrotron powder X-ray diffraction data (λ = 1.03365 Å) collected for Meso-Ni-ZSM-5 at 25 °C. Plus signs, green line, red line and blue line represent the experimental and calculated diffraction patterns, background and the difference between the experimental and calculated patterns. wR_p = 10.10%

E. DFT Cluster Model Optimized Geometries

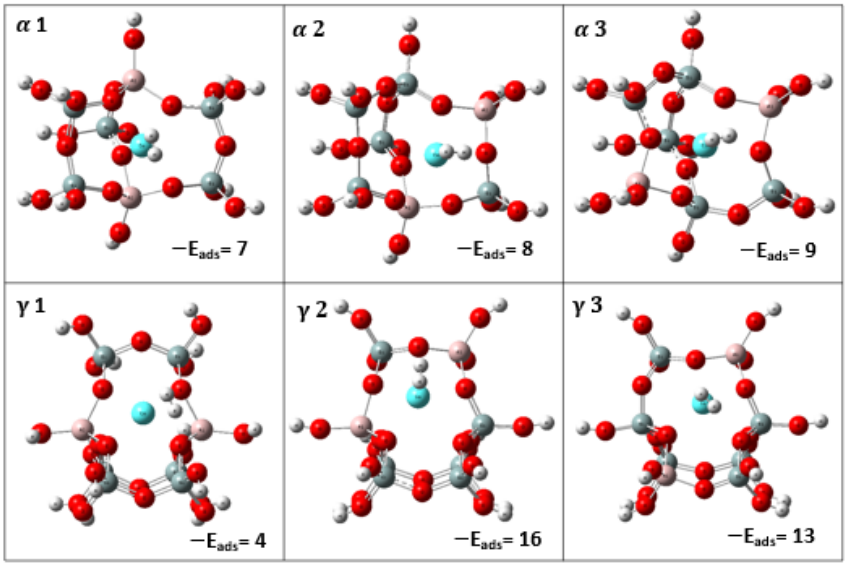

Figure E1. Optimized geometries and energies (kJ/mol) of the H_2 adsorption on Co^{2+} cations located at α and γ -sites in Co^{2+}-ZSM-5 using cluster model. Color code: Si: grey, Co: blue, Al: pink, O: red, H: white

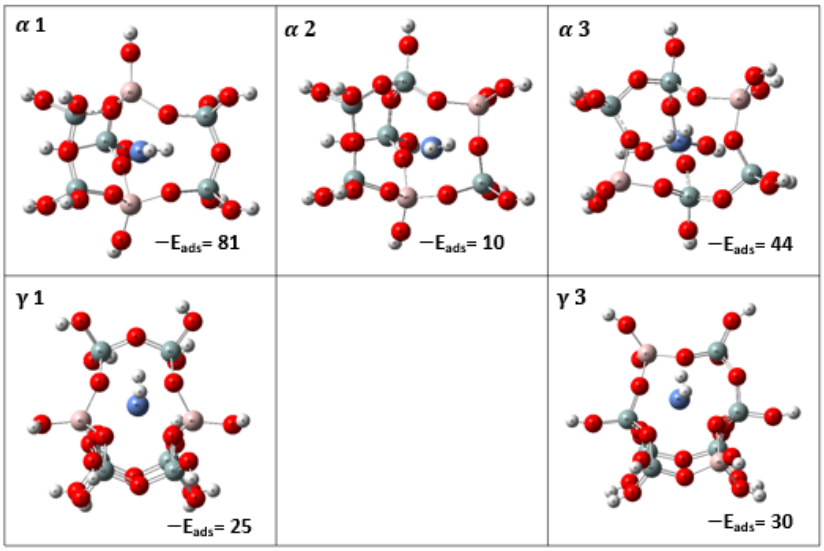

Figure E2. Optimized geometries and energies (kJ/mol) of the H_2 adsorption on Ni^{2+} cations located at α and γ -sites in Ni^{2+}-ZSM-5 using cluster model. Color code: Si: grey, Ni: blue, Al: pink, O: red, H: white